# Identification and Registration of Vascular Networks via Geometrical Graph-based Models

A dissertation submitted by

Sepideh Almasi

in partial fulfillment of the requirements for the degree of

Doctor of Philosophy

in

Electrical Engineering

Tufts University

August 2015

Adviser: Prof. Eric L. Miller

## Abstract

In this dissertation, we investigate the identification and application of geometrical graph-based models (GGMs) of tubular structures with a focus on the vascular networks. Our initial contribution is in the development of a method that directly extracts microvasculature from highly artifacted raw 3-D fluorescence microscopy images. This method comprises two novel initialization and constrained recovery and enhancement stages. The approach is fully automated using features derived from bi-scale statistical measures and produces results robust to non-uniform illumination, low SNR, and local structural variations. We next introduce a GGM-based method that identifies a piece-wise linear skeletal approximation of a microvascular network that merely requires a rough segmentation of the structures. The nodes of the graph represent the critical points (CPs), defined as locations of large structural deformation and detected with template and convex hull filterings that are independent of any a priori geometric and probabilistic information such as direction, degree, or intensity distribution. The anatomical connectivity of the CPs is derived by solving a binary integer program whose utility function reflects both intensity profile and structural information of the vasculature along the edges. In a "divide and conquer" manner, we have designed a graph interpolation technique that extends applicability of the GGM identification method to larger data sizes. Finally, the GGMs are employed to non-rigidly register cranial artery networks which is formulated as a homologous landmarks guided point correspondence problem. We have developed a novel collection of features, which we call a "signature," that captures geometrical attributes of nodes (location of junctions) and edges (length and curvature of vessels) in a topologically encoded form. Using this signature, we formulate registration as a Linear Assignment Problem (LAP) rather than the more commonly employed (and NP-hard) quadratic assignment problem. Using signatures allows us to relax the combinatorial problem to a convex form that results in a profound computational complexity reduction. By solving the LAP via a graduated assignment technique, nodes are first matched, and then the edge correspondences are determined using a heuristic approach. The performance of this method is tested using clinical angiography images and synthetic data sets. Quantitative results suggest that this method is highly reliable under the influence of different perturbing factors that turns it into a potential technique for inter-subject and multi-modal registration.

*To my parents.*

# Acknowledgements

First and foremost, I express my gratitude to my advisor, Prof. Eric Miller. It has been a privilege to know and work with Eric for his vast scientific knowledge, spot-on guides, and support of my goals. He provided a unique setting through which, I had the opportunity to considerably polish and grow my research and professional skills. It was an empowering and inspiring experience for which I give my sincere thanks to him.

I would also like to thank Prof. Xiaoyin Xu, Prof. Brian Tracey, and Prof. Misha Kilmer, the rest of my thesis committee members, for providing invaluable comments.

The clinical data that motivated us and were used in this work have been provided by our collaborators in the neurobiology and neurosurgery departments of Harvard, Prof. Gu, Dr. Lacoste, Dr. Bin-Zvi, and Tufts, Dr. Malek and Dr. Lauric, Medical Schools to whom, I am thankful.

I had a nice time at Tufts thanks to my former officemates Brian and Jincheng. They have always been an unhesitating source of thought sharing on a wide variety of topics from technical issues to social matters that made the long hours of work far more enjoyable. I am also thankful to Shideh and Sam who never held back their help and friendship. Hana, Somayeh, Galia, and Sara, thank you for creating the most joyful moments of my stay in Boston and giving your heartful company.

I cannot be more blessed having my dearest friend Shima and cousin Shilan. In spite of being thousands of miles away and from different corners of the globe, they have continuously brought warmth to my soul with their immaculate kindness and encouragements.

I specially thank my parents, Zhila and Ali-Ashraf, and my dear brother, Rouzbeh, who have shown me the unconditional love through it all. My thirst for learning started to grow by reading the stream of my father's books and in companionship of his free spirit and never stopped advancing influenced by my mother's diligence and wisdom. I owe finishing my graduate education to the mentality that they gave me.

I am grateful to my husband, Jouya. His never-failing support and care even when he was challenged with the graduate school himself, have always kept me strong through the hardest times. Being an aspiring and outstanding scholar, he has been a great source of motivation and technical insight.

This work was partially supported by the NSF Award 0958345.

# Contents

# List of Tables

# List of Figures

# Chapter 1

# Introduction

Tubular networks are one of the fundamental structures in biological and medical studies. They are found for example in the skeletal structures, nerve fibers, systems for propagating gases (intrathoracic airway trees) and fluids (vascular and microvascular networks) or used for describing hierarchies (phylogenic trees). When imaging, it is of crucial importance to devise efficient methods for analyzing such structures in terms of recognition and matching. The work in this thesis focuses on the extraction and analysis of interconnected and tree structures from various forms of biological and medical imagery with specific application to vascular networks.

Quantitative analysis of connectivity patterns in complex biological tubular networks especially the cortical vasculature has recently received growing attention for a variety of biological questions, ranging from vascular development (e.g. angiogenesis and vascular patterning), vascular physiology (e.g. regulation of brain perfusion and blood flow), vascular physiology to vascular diseases, surgical planning, and therapy [1–4]. For instance, a correlation between microvascular and neuronal densities in the murine cortex [5] was discovered recently: it was shown that in the range of 1 to 10 mm of the gray matter, neuronal and vascular densities are correlated to each other in that the functional behavior of the neurons in granular lamina detected from the brain images was consistent with and measurable from the distribution of blood vessel densities. In addition, analysis and classification of blood vessel networks in terms of the length of vessels in a given volume and the number of bifurcations have been shown to provide pathological insight into the biological properties of a sample [1]. Finally, the connectivity model of vascular networks has been used to aid in the registration of Magnetic Resonance Angiography images acquired from the same vasculature at separate points in time or from different patients [6–8].

Motivated by the above discussion, finding a well-defined mathematical and computational representation of the tubular networks that simplifies further algorithms and analysis appears to be crucial. An object's representation is defined by a collection of its discriminating geometric features that are invariant under affine and restricted elastic transformations [9]. Common shape representations are point sets, curves, surfaces, level sets, deformable templates, and medial representations.

Skeleton or medial axis that integrates topological and geometrical features of the object is an important shape descriptor for object recognition. Shape similarity based on skeleton matching usually performs better than contour or other shape descriptors in the presence of partial occlusion and articulation of parts [10,11]. One approach to approximate the medial axis of specific thin and elongated shape model of vascular networks is through the geometric graph-based models (GGMs). In the graph-based model of our concern, nodes represent branching points (junctions) or points of curvature extrema (waypoints) and edges stand for the vessel parts connecting those points. A GGM yields a compact description of both topological and quantitative specifications of volumetric vascular systems via piece-wise linear approximation to their centerlines. These models can be applied to all the problems mentioned above. For example, junction degree can trivially be determined from the graph and vessel length approximated by the physical length of the edges on the shortest path between two junctions in the graph. Also, adding the cross-sectional area information to the edges, it will be possible to analyze the blood flow.

Graphs are particularly convenient to process and compare across diverse image appearances in different modalities, scales, and times. This universality property allows us to combine the specific information from each modality to turn them into a strong and effective asset in feature-based registration, statistical analysis for abnormality detection, and image-guided surgery. They provide a relatively low dimensional representation that our work demonstrates is robust to a wide range of imaging challenges. Also, there are is a vast literature on the graph analysis subject and a large number of methods have been established for that matter.

In this dissertation, we develop and test novel graph identification and registration algorithms using a diverse database of vascular data obtained by fluorescence microscopy and angiography of murine and human subjects. We start from pre-processing of the data for binary image extraction and continue with building graph-based models for general (i.e., non-tree) networks. The data of interest for these parts are collected from microvasculature of murine cortex via 3-D fluorescence microscopy. Finally, we have investigated the registration problem of the graph-based models. We used magnetic resonance angiography

(MRA) and 3d rotational angiography (3dRA) images of the arterial network of the human cortex as a basis for graph matching purpose.

## 1.1 Volumetric extraction of vascular structures

As it is common in vascular detection methods, an initial stage is necessary to denoise, enhance, and binarize the raw data [12, 13]. The binary image is then used as the basis for the rest of the GGM derivation processing. Segmentation of vasculature is also of high importance for quantitative analysis and visualization purposes in diverse fields of study such as neuroscience [14] and tumor monitoring [15]. The segmented data set provides a means to extract crucial quantitative information about the vasculature such as surface areas, diameters, tortuosities, and branching patterns of vessels. It also can serve as a platform for performing further advanced processing [2].

Of particular interest to us is the case of cortical microvasculature determination in murine models from 3-D fluorescence microscopy data stacks that manifest vessels of low tortuosity. This data of interest indeed calls for pre-processing as accurate and fast segmentation and volumetric reconstruction of the complex microvasculature networks from fluorescence microscopy images faces challenges owing to the existence of numerous imaging artifacts shown in Figure 1.1: uneven illumination, non-homogenous intensity distribution inside the vessels, low SNR regions, high spatial density or closeness of vessels, reduced contrast at edges, broken or faint vessels, and low frequency background variations caused by scattered light [12, 16]. The noise stems from several sources such as stochastic photon counting, thermal and electrical fluctuation in the imaging device, biological background, and non-uniform fluorophore distribution [16, 17]. Many of these problems are related to the photon counting nature of the imaging system. For that matter, the image quality is directly determined by the number of detected photons that is in turn controlled by the exposure time which has to be limited to preserve the health of the specimen as excessive fluorophore excitation causes cell phototoxicity and photobleaching [18]. Thus, lower number of detected photons results in an SNR reduction in the obtained images. Also, images of poorly stained samples are likely to show structural irregularities such as vessel breakage [19].

These issues result in two challenges: (1) identifying the smaller structures along with their connectivity (breakages are prevalent for these cases) and (2) the recovery of larger vessels that tend to be surrounded by heavy imaging artifacts making the boundaries more difficult to perceive (over segmentation is an issue). Therefore, developing segmentation

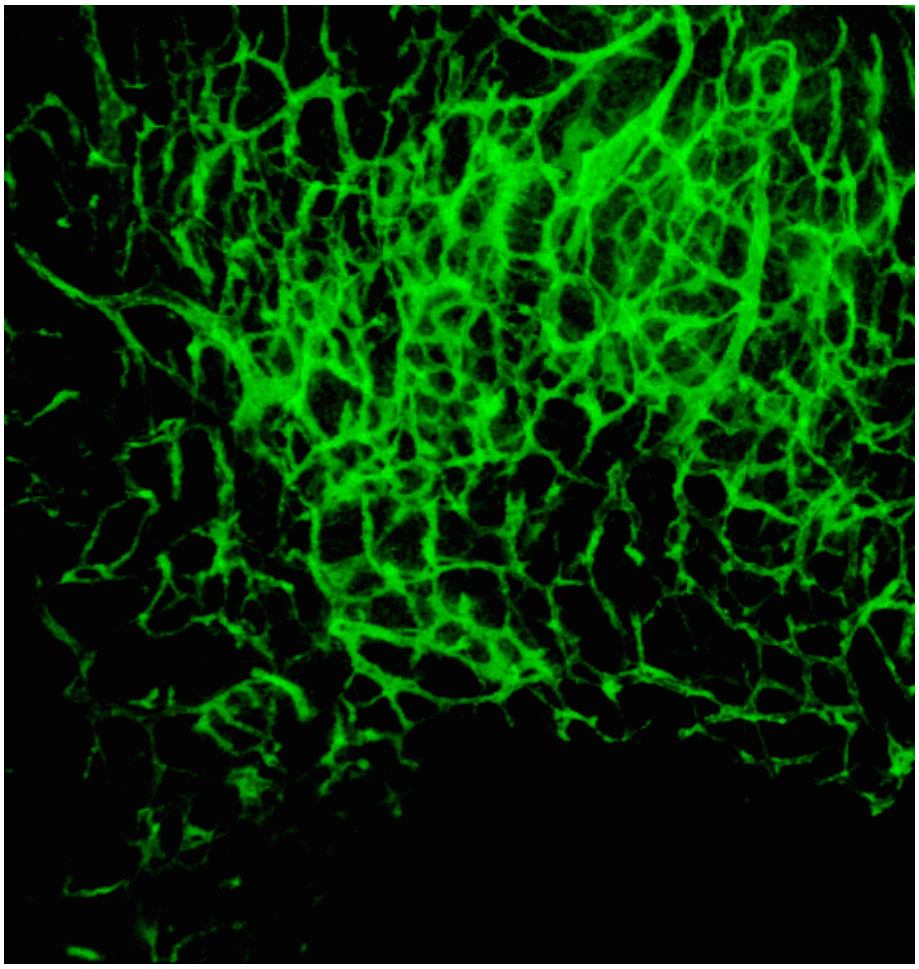

Figure 1.1: In this maximum intensity projection of 3-D fluorescence microscopy image of murine cranial tissue, miscellaneous imaging artifacts are visible: uneven illumination (upper vs. lower parts), non-homogenous intensity distribution inside the vessels (visible in the larger vessels located at top right corner), low SNR regions (lower areas), high spatial density or closeness of vessels (majorly in the center-upper parts), reduced contrast at edges (visible as blurs mostly for the central vessels), broken or faint vessels (lower vessels), and low frequency background variations caused by scattered light (at higher density regions).

algorithms that can overcome imaging artifacts, are robust to the imaging artifacts and structural variations is of great importance.

Several studies have been done on the subject of vascular or in general term tubular structures segmentation for different imaging modalities [2, 8, 20]. They include methods such as active contours [21,22], geometric model-based techniques [23,24], or region growing approaches [25], tracking [26], and template-based methods [27]. Tracing-based algorithms

work by following vascular segments starting from some initial seed points. These methods fail at recovering broken vessels and are highly dependent on the seed point selection. Matched filtering based approaches model the vessel structure as the intensity-ridges of a multiscale vesselness function [28]. These algorithms are susceptible to outliers and are not robust to noise [29]. Active contour approaches are flexible in terms of finding the intricate vessel shapes. However, they are prone to leakage into the background where edges have low contrast. This property can drastically undermine the performance of active contours where the segmented structure is dense and leakage will lead to merging of separate vessels. A popular region accumulation approach is the watershed transform, but this approach can result in over segmentation and requires further processing [30]. The method proposed in [31] that uses a combination of clustering and classification techniques to segment vasculature segments vasculature suffers from broken vasculature and requires a linking post processing. Also, its parameters are selected regardless of the structures size and undermine the performance of segmentation in networks of varying size vasculature. Finally, model-based methods require *a prior* information on the vascular structures [2]. Therefore, developing an efficient algorithm that can jointly retrieve microvascular volume and remove noise from data is necessary.

We have developed a new iterative algorithm that is able to provide precise segmentation of data without the requirement of denoising or performing any image quality boosting operations. The iteration starts with a robust initialization scheme that is unbiased to the non-uniform illumination or lower SNR conditions and is based on local statistical analysis of image intensities. A full segmentation is achieved by iteratively augmenting the seed points through clustering/voting of feature vectors formed by voxels location, local intensity gradient, and non-linear statistical measures information such as median level. We perform vessel segmentation with the following contributions. First, we remove *a priori* geometrical assumptions such as curvature or branching pattern about the vessels except for the local diameter. Then, the segmentation is designed in such a way that it restores the vasculature while rejecting the imaging artifacts. This method is automatic and does not require manual interaction. Collection of these features allows us to get the best segmentation out of the 3-D fluorescence microscopy data. Experimental results obtained from synthetic and real datasets confirm that the proposed algorithm greatly improves upon the previous segmentation methods performed on vasculature data.

## 1.2 Geometrical graph-based model identification

Typically, problems of finding graph-based models are solved in a three-step fashion. First, a comprehensive segmentation of the image is obtained using methods such as active contours [21,22], geometric model-based techniques [23,24], or region growing approaches [25]. Then, the tubular structure's skeleton is found using methods such as thinning [32]. Finally, a graph-type model is derived from the skeleton as a post processing step. These methods face a number of difficulties. Perhaps most importantly, common detailed segmentation methods are difficult to automate. Even state of the art methods require extensive human interaction [2,8,20]. This can be a major shortcoming for large problems and when the vascular network is comprised of very closely spaced structures. Also, in the presence of high noise level, intensity contrast between the object and background decreases and boundaries weaken resulting in a loss of accuracy in segmentations obtained by region growing and edge detection methods [33]. Additionally, a segmentation-first approach does not necessarily give rise to an accurate network graph. For example, many of the skeletonization methods struggle when segmentation yields gaps in the vessels [2]. Establishing a graph based on the skeleton needs a tracking step that adds to the complexity and error rate of the process. These three-step types of methods have been developed primarily for networks with tree-type structures such as neural, bronchial, and breast ductal networks [34–38]. For these cases where the graph has a tree structure, different implementations of the minimum spanning tree using Euclidian [7] or Mahalanobis distances [39] have been proposed to determine the graph from the segmented images. Because vascular networks are not always of a tree-based shape given fluorescence microscopy data of mixed image quality, these techniques are not applicable and new methods are required.

Recently there have been some efforts in identifying centerlines directly from the data without first performing a high-resolution segmentation. Ridge-based methods [40] and minimal path techniques [41] are the most common algorithms of this type. The former locates the tubular structures' skeleton by finding and following the image's intensity ridges [8]. Vessel tracking algorithms start from a set of seed points and follow the centerline by maximizing an energy function correlating to the vessel centerlines [2]. These methods both require the beginning and end points generally or the root point for vascular trees and hence are most appropriate for interactive work [2]. Due to the required human interaction, they are inefficient in manipulation of large data sets where manual selection of such points would be burdensome. Error accumulation along the tracking routes produced by the noise or other imaging artifacts is another drawback of these types of methods [42].

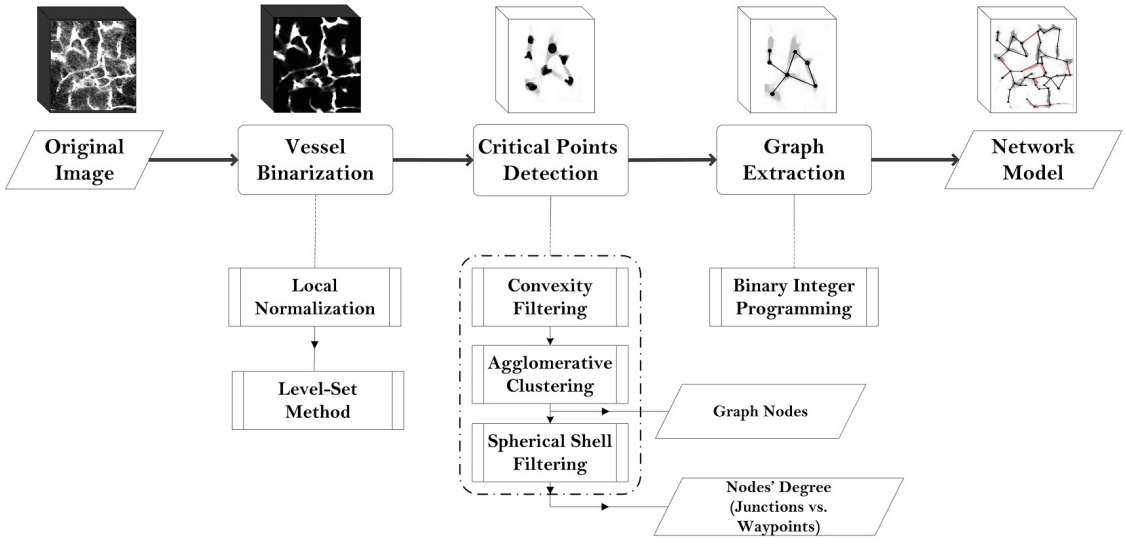


Figure 1.2: Overall view of the proposed network modeling method. Dashed lines encompass the detailed steps of each stage while parallelograms indicate the outputs.

Relevant to the problem of interest however are recent methods directed at recovering loopy structures [43]. The method proposed in [43] first builds an overcomplete graph representing the network by connecting a set of evenly spaced nodes located on the directly connected structures. Subsequently, a globally optimal graph is computed from this initial graph. This approach though is not able to handle cases such as those encountered in the problem of interest here where challenges with the data are apparent including breaks or dimness in the vasculature. In another paper [44], the centerline is found by tracing the intensity ridge paths along a set of manually selected seed points. Additionally, as with the work in [43], this "tracing-based" algorithm was not developed to address the issue of broken vessels.

The specific processing chain is illustrated in Figure 1.2. Critical points that are comprised of both vasculature junctions and points of relatively high curvature along individual branches are detected in the next stage.

This work contributes to the existing state-of-the-art through the development of a novel microvascular network model identification approach using BIP that approximates a general vasculature's skeleton by its GGM without the need for first performing a detailed segmentation of the data, deriving the structure's centerline, or manually selecting the seed points. Since the number of CPs in a network sample can be huge, manual intervention has to be minimal. Our approach is free of prior assumptions on the degree of junctions (*i.e.*, the number of connections) or orientation of the connected branches making it well suited

for the structural variability and compactness across a given volume. Graph extraction is accomplished in each image by solving a binary integer programming (BIP) problem [45] where the variables represent potential edges of the graph. A binary variable is associated with every possible edge linking pairs of CPs. Using the binary images, each such edge is assigned a "utility" constructed to reflect both local and global features of the microvascular structure. The BIP then determines the inclusion of edges in the final graph of each data volume in order to maximize the associated utility.

This method eliminates the common need for feeding seed points to the algorithm while the graph is built based on the structurally critical points found by direction and scale invariant techniques. Since the graph's edges are not weighted solely based on local image attributes but rather more global measures, this method can easily overcome many common challenges such as slight vessel breakages, faint vessels, or the presence of spurious branches. Given all these features, graph-based post processings [2] are not required.

## 1.3 Geometrical graph-based model registration

To examine vasculature, assess state of a disease during diagnosis, monitoring, and treatment processes, it is crucial to match different images of vascular networks [46]. Therefore, image registration is an inevitable element of the process. It is important to develop methods that register pairs of vascular images taken at different times, scales, from different directions, or using different modalities with minimal intervention.

The problem of tubular network registration faces challenges in different ways. These structures do not have enough spatial texture and are structurally sparse in comparison to other organs, thus even small variations in their location result in wrong results. Also, their appearance varies largely between patients such that their intensity-based registration is inefficient and prone to errors [47]. One approach to overcome these challenges is to register vasculatures through their graph-based models. The geometrical transformation between two vascular networks is considered to be a combination of non-rigid or global transformation and morphing that is local and rather small due to the anatomical properties. Figure 1.3 illustrates the two types of transformations for two sample graph shapes. Analyzing the range of morphings for cranial vascular networks is the target of many fundamental neurobiological and neuroscientific studies. Advantageously, these structures can be represented by GGMs through integrating key geometrical and topological information of the vascular networks. Using such a model, graph matching can be used to tackle registration. It has been shown that graph matching based registrations usually perform superior to the

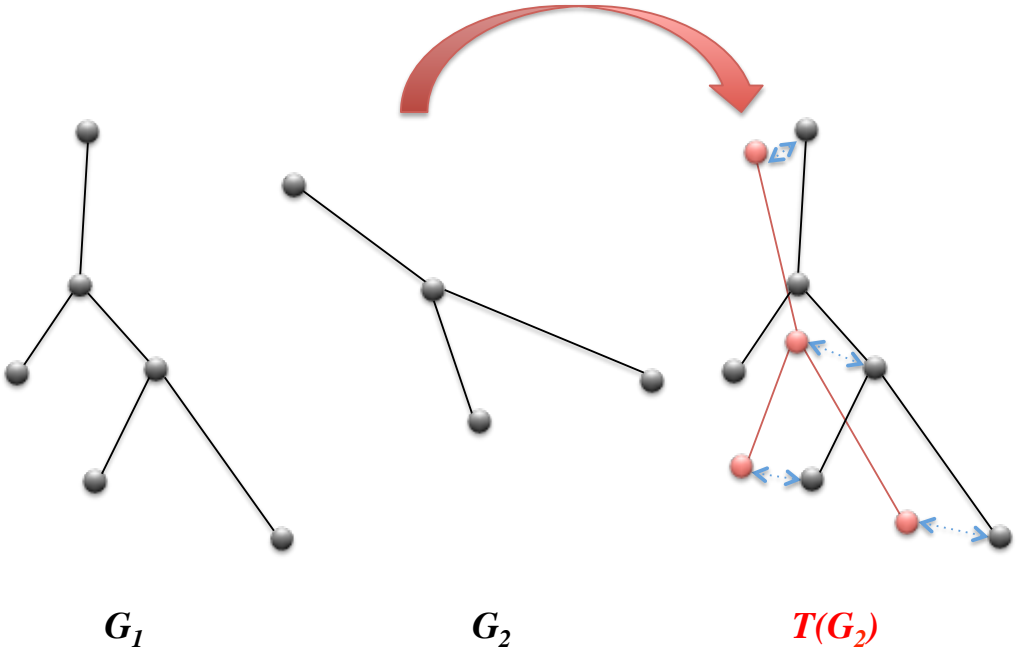


Figure 1.3: The non-rigid transformation $T$ of $G_2$ that globally aligns it with $G_1$ and the morphing between nodes of $G_1$ and $T(G_2)$.

ones that use contours or other shape descriptors [11].

Graph matching in general is a fundamental problem in computer vision and image processing required for many practical problems in pattern recognition [48], object recognition [49], and bioinformatics [50, 51]. Generally speaking, a matching problem seeks to find node and edge correspondences across two graphs based on specific optimality measures. The optimality can be in regard with graphs' alignment or node labeling for instance [52]. The graph matching is a NP-hard combinatorial optimization with factorial complexity by nature.

In the simplest case that graphs are of the same cardinality (equal number of nodes), matching amounts to finding an exact one-to-one correspondence *i.e.* an optimal permutation. This type of problem is considered as bipartite matching that can be solved with the Hungarian method [67]. However, in real world applications, graphs are extracted from data and through methods that are susceptible to noise and processing artifacts. Thus they are hardly of the same cardinality, and we face an inexact graph matching problem. This means that some nodes do not have any correspondences in the other graph. These nodes are called *outliers*. Medical images usually suffer from such cases as they are affected by noise-induced errors in segmentation, reconstruction, or modality fusion. This is even more

intense for skeleton-representing trees that show many variations and are hardly identical in their geometrical and topological characteristics.

Inexact graph matching searches for the optimal isomorphism between the largest possible subgraphs (Garey and Johnson, 1979). This problem is also NP-hard and there is no known polynomial time algorithm to solve it (Garey and Johnson, 1979). A substantially studied and used form of inexact graph matching is formulated as a quadratic assignment problem (QAP) [52, 53]. Joint inclusion of affinity and assignment matrices in the QAP yields simultaneous correspondence determination of nodes and edges [54]. Several methods are developed to relax the QAP and approximating the optimal matchings for tackling computational cost and boosting its scalability.

The above discussions motivates developing new matching methods that register GGMs robustly and additionally address the computational bottleneck.

We have developed a general method for matching 3-D tree-type structures via their GGMs. For this purpose, the geometrical graphs are modified by removing waypoints and their connected edges and replacing abstract edges between junctions to produce the attributed graphs. Node attributes are defined to be the junctions location and edge attributes are corresponding vessels approximated length and curvature. A novel feature termed signature is proposed for matching attributed graphs nodes, that utilizes geometrical attributes and topological information of graphs simultaneously. Edge correspondences are derived subsequent to node matching. We take advantage of the intuition that two nodes are correspondent if their neighbors also correspond maximally to build signatures and formulate the matching problem in a point correspondence form. As a result of encoding the local topologies in an algebraic form, we have eliminated the need to enter the adjacency matrix into computations. Thus, matching is converted to a linear assignment problem that is computationally less expensive than the alternate method for QAP which is NP-hard. Inspired by the graduated assignment method, we relax the assignment matrix to be a doubly stochastic with continuous elements that turns the combinatorial problem into a convex optimization. The performance is tested using synthetic and clinical data obtained from 3-D angiography images. Synthetic data are derived from clinical data through nonlinear operations resulting in node removal and displacement. We have controlled the parameters contributing to these operations to evaluate the method against node displacement and problem size factors. Quantitative results confirm the high reliability of this method when challenged by different settings. Effectiveness of our method has also been tested for inter-subject cases where graphs are obtained from clinical data of different patients. Both qualitative and quantitative results confirm high performance of the method in this regard

too. Finally, data of different modalities (MRA and 3DRA) have been matched through the proposed method to assess its performance for scenarios where only partial structural homogeneities exists.

## 1.4 Contributions

**Volumetric extraction of vasculature**:

To overcome the challenges imposed by the nature of fluorescence microscopy images that are characterized by a range of imaging artifacts including space-varying signal to noise ratio (SNR), scattered light, and non-uniform illumination, we developed a novel iterative method that segments the 3-D microvasculature directly from the original fluorescence microscopy images instead of employing pre- and post-processing steps such as noise removal and segmentation refinement as used with the majority of segmentation techniques. Our algorithm achieves the goal of segmentation via design of an iterative approach that extracts the structure through clustering/voting of feature vectors formed by voxels location, local intensity gradient, and median value. Our algorithm starts from some automatically selected seed points found by a robust binarization scheme that is unbiased to the non-uniform illumination or lower SNR conditions. Qualitative and quantitative analysis of the experimental results obtained from synthetic and real data prove the efficacy of this method in comparison to the state-of-the-art segmentation methods.

**Geometrical graph-based model identification**:

An automatic and novel approach to determine the global topological structure of a vascular network that does not require the detailed segmentation of the vessel structure is developed in this work. The method directly computes a piecewise linear approximation to the vasculature skeleton by constructing a graph in three dimensions whose edges represent the skeletal approximation and vertices are located at Critical Points (CPs) on the microvasculature. The CPs are defined as vessel junctions or locations of relatively large curvature along the centerline of a vessel. Our method consists of two phases. First, we provide an automated CP detection technique that eliminates the common need for providing seed points to the vascular identification algorithm. This method does not require any *a priori* geometric information about the junctions in particular such as direction or degree. Via using the convex hull of the local segments of vasculature we have made the detection robust to the non-smooth boundaries.

Second, connectivity between detected nodes is determined via the solution of a Binary

Integer Program whose variables determine whether a potential edge between nodes is or is not included in the final graph. The utility function in this problem reflects both intensity-based and structural information along the path connecting the two nodes. Finally, because of variability in the data across a given volume, it proves advantageous to solve this graph construction problem over non-overlapping blocks in the full data set. An optimization-based graph interpolation technique is developed to allow merging of sub-images' derived graphs to form a global model. Qualitative and quantitative results confirm the utility and accuracy of this method. Employing the graph concept makes this work unique and distinguished because of its ability of restoring weak structures such as dim or broken vessels and eliminating the need for the gap filling and other post processing methods common to use for these problematic structures.

**Geometrical graph-based model registration**:

The cranial artery networks show specific geometric properties in structure that has motivated us to investigate the application of graph matching as a tool for general vasculature registration. In this dissertation, we exploit the intuition that the correspondence of two nodes is also a function of the correspondence of their neighbors to build a novel feature that embodies geometrical attributes of nodes (location of junctions) and edges (length and curvature of vessels) in a topology encoded form. This feature structure is used to formulate the matching problem as a linear assignment problem that is computationally less expensive to solve than the alternate QAP method which is NP-hard.

Inspired by the graduated assignment method, we relaxed the combinatorial problem into a convex optimization and developed an algorithm to solved it. Then the edge correspondences are determined using a heuristic approach. The performance of this method is tested and validated using clinical angiography images and synthetic data sets. Finally, we have shown that nodes at higher levels from the CoW have larger spatial variation via the proposed graph registration technique.

## 1.5 Thesis organization

This dissertation is organized with Chapter 2 describing the technical details of the methods used in the remainder of the work. In Chapter 3, we present the proposed microvasculature segmentation technique in two parts of initialization and vessel recovery method. This chapter also presents the segmentation evaluation results obtained from synthetic (quantitative in terms of sensitivity and specificity) and real data (qualitative). The segmentation

performance is compared to state-of-art methods using real fluoroscopic data. Chapter 4 describes the microvasculature network identification algorithm in detail including pre-processing, critical point detection, and graph-based connection mapping. It discusses the empirical results that are given in both qualitative and quantitative demonstrations. In Chapter 5, we present the proposed graph matching technique and the non-linear approach to solve the developed formulation. The evaluation results obtained from synthetic and clinical data are presented in this chapter. Finally, Chapter 6 concludes the dissertation and indicates the possible future paths for continuing this study.

# Chapter 2

# Technical Background

In this chapter, we cover the algorithmic details of the techniques that have been exploited in this dissertation.

## 2.1 Clustering Techniques

Clustering or cluster analysis refers to the act of grouping objects such that objects assigned to the same group are the closest given a specific distance metric. Clustering has a wide range of applications in data analysis, image segmentation, pattern recognition, and machine learning. Depending on the application and separation criterion, different clustering methods have been developed. In the following sub-sections, three types of the most popular clustering methods are described comprehensively.

### 2.1.1 $k$-means Clustering

As a centroid-based clustering method, the $k$-means algorithm divides $N$ data points $x_1, x_2, \ldots, x_N \in \mathbb{R}^d$ into $k \leq N$ partitions $S_1, S_2, \ldots, S_k$ with prototypes (usually means) $\mu_1, \mu_2, \ldots, \mu_k$ aiming to minimize the within cluster sum of squares or the squared-error distortion

$$\arg\min_{r_l^i, \mu_l} \sum_{l=1}^{k} \sum_{i=1}^{N} r_l^i \|x_i - \mu_l\|. \tag{2.1}$$

where $r_l^i$ is the assignment index defined as

$$r_l^i = \begin{cases} 1 & \text{if } x_i \in S_l \\ 0 & \text{else} \end{cases}. \tag{2.2}$$

This clustering problem is solved through iterative disjoint optimizations of $r_l^i$ and $\mu_l$ where at each stage the other parameter is held fixed. The method starts from a set of initial prototypes. There are two common approaches to initialize the $\mu_l$s: Forgy and random partition methods. The Forgy method that is more popular in the literature first randomly chooses $k$ points as initial means, then assigns each data point to the closest mean. This way, the initial means have more spread among the data points. The random partition method however, randomly forms the partitions, and then computes the means. This method gives means that are mainly distributed around the center of data set.

Given the initial $\mu_l, l = 1, \ldots, k$, determining the optimal assignment indices, $r_l^i, i = 1, \ldots, N$, is equivalent to finding the mean with minimum distance to each data point formulated as

$$\arg\min_l \{\|\mu_l - x_i\|\}, \quad i = 1, \ldots, N. \tag{2.3}$$

In the case that a tie happens meaning that a data point is equidistant from two means, $l$ is set to be the smallest of the two.

Since the least-square estimator is the Euclidean mean value, solving (2.1) for $\mu_l$ reduces to finding Euclidean mean values of the new clusters determined on the indices obtained from (2.3). The new clusters' means are updated according to

$$\mu_l = \frac{1}{R^l} \sum_{i=1}^{N} r_l^i x_i, \quad l = 1, \ldots, k, \tag{2.4}$$

where $R^l$ is the number of data points assigned to the $l^{th}$ cluster or

$$R^l = \sum_{i=1}^{N} r_l^i, \quad l = 1, \ldots, k. \tag{2.5}$$

The $k-$means clustering is investigated as a variation of the gradient descent algorithm in [56] and it has been proved to converge. At convergence, the $k$-means clustering yields a set of data points classified into Voronoi cells [57, 58] with the least error rate.

The $k-$means clustering is known as an NP-hard problem to solve. Since achieving the optimal solution is not guaranteed, its approximation is commonly searched instead. A well-known method of approximation for this purpose is Lloyd's algorithm [57]. Through this method, the most optimal solution is sought among the results obtained from several clustering runs using different initializations.

One instance of the $k-$means algorithm is demonstrated in Figure 2.1 for a two-dimensional data set given $k = 4$. Clusters are signified by presenting their associated points with distinguishing mark styles where means are shown by red circles. Figure 2.1(a)

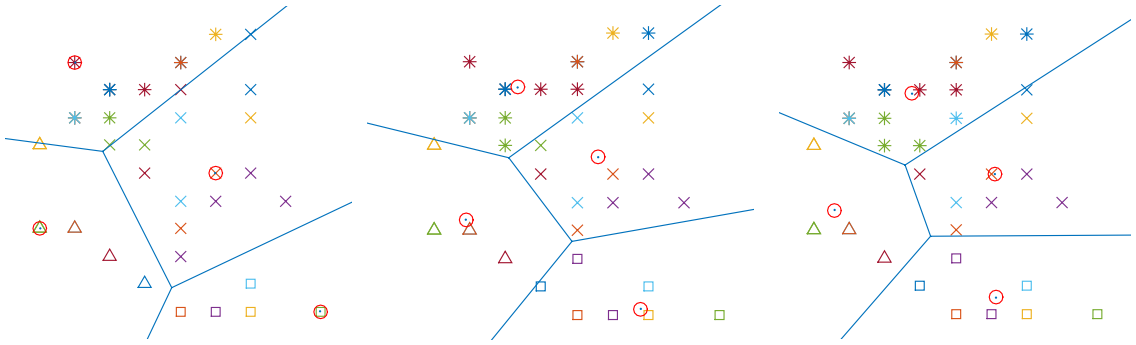

(a) (b) (c)

Figure 2.1: (a) Initial means (red circles) and clusters, (b) updated means according to the new partitioning, and (c) converged clustering.

shows the initial means and their clusters where Figure 2.1(b) presents the updated means and clusters. Figure 2.1(c) demonstrates the converged means and their corresponding clusters. The Voronoi diagrams that mark the clusters' boundaries are shown with blue lines.

This method works best for data points with similar distributions. For the cases that $k$ is not specified in advance, the distortion is calculated for different counts of clusters. As the number of clusters or centroids increase, the squared error distortion smoothly decreases as a result of lowering distances [59]. After some point however, these decreases tend to diminish as one sees a "knee" in the curve of distortion versus $k$. The location of this knee then can be used to select an appropriate number of clusters [60].

### 2.1.2 Otsu Method

Otsu's algorithm is an automatic (unsupervised) clustering based segmentation/ thresholding technique that is considered as a variant of the linear discriminant analysis (LDA) methods [61]. The LDA methods generally classify a set of points or objects with a linear combination of well-separating features especially variance-based metrics [62]. Given a gray-level histogram, the Otsu's method method seeks an optimal threshold yielding two classes of $C_1$ and $C_2$ with the most inter-class variance. This type of variance provides a strong measure of separability between the classes.

For an image data with $L$ discrete intensity levels and a threshold value of $k$, $C_1$ equals to the pixels with intensities $= 1, \ldots, k$, and $C_2$ includes the remaining pixels, points with

intensities $= k+1, \ldots, L$. Thus, the mean of $C_1$ and $C_2$ are

$$\mu_1 = \sum_{i=1}^{k} i\, Pr(i|C_1) = \tfrac{1}{\omega_1} \sum_{i=1}^{k} i\, p_i$$
$$\mu_2 = \sum_{i=k+1}^{L} i\, Pr(i|C_2) = \tfrac{1}{\omega_2} \sum_{i=k+1}^{L} i\, p_i \tag{2.6}$$

where $p_i = n_i/N$ is the probability (occurrence rate) of intensity level $i$ with $n_i$ repetitions in a data of size $N$, and $\omega_1$ and $\omega_2$ are probabilities of each class such that

$$\omega_1 = Pr(C_1) = \sum_{i=1}^{k} p_i$$
$$\omega_2 = Pr(C_2) = \sum_{i=k+1}^{L} p_i. \tag{2.7}$$

The following relations hold between these parameters where $\mu_T$ is the total mean, $\mu_T = \sum_{i=1}^{L} i p_i$.

$$\omega_1\mu_1 + \omega_2\mu_2 = \mu_T$$
$$\omega_1 + \omega_2 = 1. \tag{2.8}$$

The single class variances are

$$\sigma_1^2 = \sum_{i=1}^{k} (i-\mu_1)^2 Pr(i|C_1) = \tfrac{1}{\omega_1} \sum_{i=1}^{k} (i-\mu_1)^2 p_i$$
$$\sigma_2^2 = \sum_{i=k+1}^{L} (i-\mu_2)^2 Pr(i|C_2) = \tfrac{1}{\omega_2} \sum_{i=k+1}^{L} (i-\mu_2)^2 p_i \tag{2.9}$$

and the inter-class variance is defined as

$$\sigma_B^2 = \omega_1(\mu_1 - \mu_T)^2 + \omega_2(\mu_2 - \mu_T)^2 \;=\; \omega_1\omega_2(\mu_2 - \mu_1)^2. \tag{2.10}$$

Letting $\sigma_T^2$ to be the total variance of the data, $\sigma_W^2 + \sigma_B^2 = \sigma_T^2$, maximization of the $\sigma_B^2$ is equivalent to minimization of the combined intra-class variance (spread) defined as the weighted sum of clusters variances

$$\sigma_W^2 = \omega_1\sigma_1^2 + \omega_2\sigma_2^2 \tag{2.11}$$

that yields the optimal threshold $k_{opt}$. Otsu's method iterates through all the possible $k$ values, from 1 to $L$ here, and calculates $\sigma_W^2$ or $\sigma_B^2$ as a measure of intensity level spread in $C_1$ and $C_2$. The $k_{opt}$ is the threshold value that maximizes $\sigma_W^2$ or minimizes $\sigma_B^2$. Figures 2.2(a,b) show two images where their histograms are presented in Figures 2.2(c,d). The first image has a rather bimodal histogram whereas the second image shows a single dominant mode. The segmented images are shown in Figures 2.2(e,f). It is clear that the segmentation quality is strongly correlated with the bi-modality of histograms and increases in Figure 2.2(e) compared to the Figure 2.2(f).

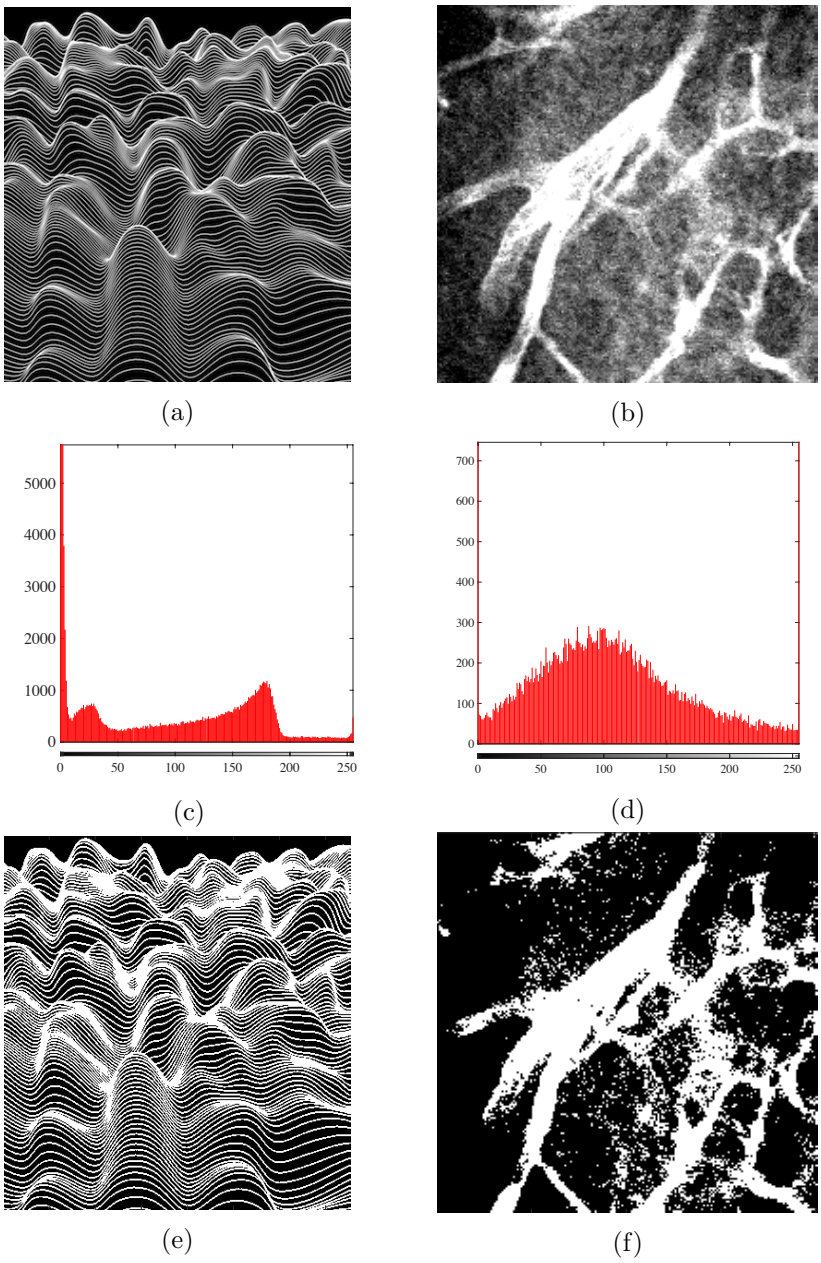


Figure 2.2: (a,b) Original images, (c,d) histograms, and (e,f) clustered images obtained using the Otsu's method.

### 2.1.3 Agglomerative Clustering

Agglomerative clustering belongs to the group of hierarchical clustering algorithms (HCA) that only require a measure of distance between the observations to operate. The HCAs perform either from top level (total data) down or from the bottom (separate single data

points) up [63]. The bottom-up or agglomerative clustering algorithm (ACA) counts each data point as an independent cluster at the finest partitioning, $P_0$, and then merges or agglomerates pairs of clusters in hierarchies generating $P_{i+1}$ from $P_i$, $i > 0$. The ACA continues cluster merging until when all of the clusters are merged into a single cluster that includes the entire data points, $P_f$. Figure 2.3 shows a simple schematic view of the agglomeration process. The clusters in each $P_i$ are labeled with $c_1, \ldots, c_{n_i}$. Thus, $n_0 = N$ and $n_f = 1$ where $N$ is the number of data points.

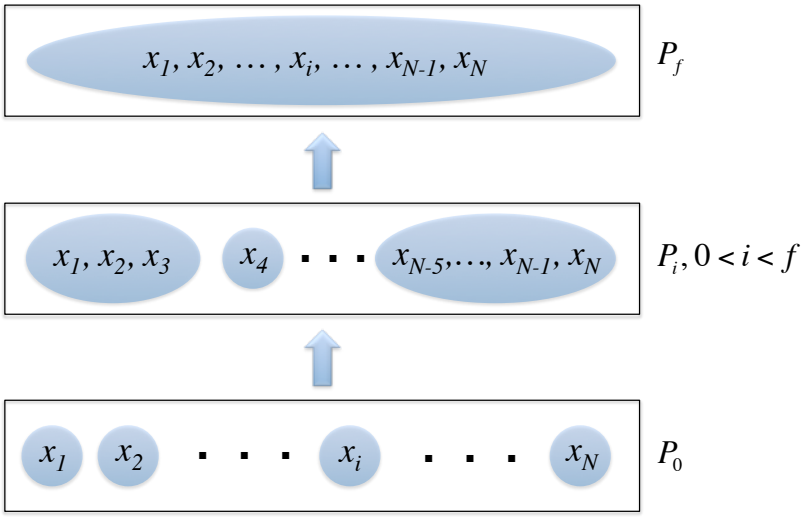


Figure 2.3: The schematic view of agglomerative clustering. The agglomerated clusters, blue regions, start from disjoint groups of data points $x_i$, $i = 1, \ldots, N$ at zeroth level partitioning, $P_0$, and merge together until reaching a single cluster made by the entire data points at the final partitioning level, $P_f$.

The basis on which the agglomerative clustering algorithm decides to merge the clusters is a measure of their dissimilarity and a linkage criterion which determines dissimilarities as a function of the pairwise distances of data points across the clusters. The choice of dissimilarity metric and linkage criterion controls the clustering manner and depends on the application of interest. Commonly used in the literature are the Minkowski metrics defined as

$$L_p(x, y) = \left( \sum_{i=1}^{k} |x_i - y_i|^p \right)^{\frac{1}{p}}. \tag{2.12}$$

Depending on the $p$ value, different types of distances can be obtained from this family. The Manhattan distance for which $p = 1$ equals to the $L_1$ norm. The Euclidean metric or $L_2$ norm results from letting $p = 2$, and for the limit of the $L_\infty$, the Chebychev metric is produced where $L_\infty(x, y) = max|x_i - y_i|\,, 1 \geq i \leq k$.

Matrix $D$ is formed by pair-wise distances of the clusters where $D(i,j) = d(c_i, c_j)$. The procedure through which these distances are calculated is based on the linkage criterion type. The linkage criterion determines clusters' distance as a function of their elements pair-wise distances. The most common criteria are maximum (complete) linkage defined as

$$d(c_i, c_j) = \max_{x \in c_i,\, y \in c_j} d(x, y), \tag{2.13}$$

minimum (single) linkage as

$$d(c_i, c_j) = \min_{x \in c_i,\, y \in c_j} d(x, y), \tag{2.14}$$

and mean (average) linkage for which

$$d(c_i, c_j) = \frac{1}{|c_i||c_j|} \sum_{x \in c_i} \sum_{y \in c_j} d(x, y) \tag{2.15}$$

where $|c|$ is the cardinality of cluster $c$. Finally, given that $c_i^*$ and $c_j^*$ are the centroids of $c_i$ and $c_j$, the centroid linkage is defined as

$$d(c_i, c_j) = d(c_i^*, c_j^*). \tag{2.16}$$

At each partitioning level, the ACA searches for the closest pair of clusters. Then, it replaces the rows and columns related to the closest clusters in $D$ with single row and column representing the new agglomerated cluster. The entries of matrix $D$ will be updated in the way that the revised elements reflect the distances of the cluster with the rest of the clusters. The ACA iterates $N-1$ times to deliver a hierarchy of agglomerated clusters until reaching $P_f$.

The dissimilarities grow by advancing in the agglomeration levels. Thus, one can use distance criterion to achieve the desired clustering precision. For the same purpose, the number criterion is an alternative if having a specific number of clusters, $n_i$, best fits the problem. When neither of the distance and number criteria is specified, the clustering can be stopped when there is a relatively large difference in the similarity measure of choice between two consecutive partitioned sets, $P_{i-1}$ and $P_i$.

The computational complexity of the ACAs is generally $\mathcal{O}(N^3)$. Therefore, they perform rather slow for larger data sets. However, they do not require a priori knowledge of the number of clusters.

## 2.2 Binary Integer Programming

A binary integer program (BIP) is of the form

$$\begin{aligned} \max \quad & c^T x \\ s.t. \quad & Ax \leq b \\ & x \in \{0,1\} \end{aligned} \tag{2.17}$$

where $c \in \mathbb{R}^{N\times 1}$ is the utility vector and $A, b, A_{eq}$, and $b_{eq}$ define the constraints on the binary variables to be optimized $x = (x_1, x_2, \ldots, x_N)^T$.

Solving an integer program in general is a difficult task. The difficulty stems from the fact that feasible regions of integer optimization problems consists of a discrete set of points or a lattice (red points in Figure 2.4) rather than a convex set (blue polytope region in Figure 2.4) that is the case for linear optimization problems with continuous variables.

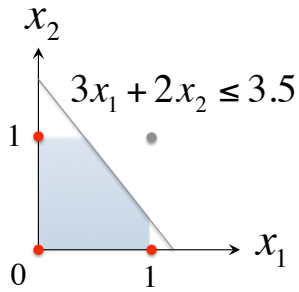


Figure 2.4: Two types of feasible region for discrete and continuous variables are shown for the given linear constraint: red points for BIP and blue convex region for continuous variables, $x_1, x_2 \in [0, 1]$ .

The convexity of feasible region guarantees the global optimality of any locally optimal solution while global optimality has to be investigated for integer problems. One approach to ease this complexity is relaxing the binary variables to continuous values in a convex set. Thus, the BIP can be transformed into a linear program (LP) that is computationally less complex to solve and in practice gives good approximations. Also, several efficient methods in computational mathematics exist that solve the LP. One approach to have LP numerically solve the BIP problems is through using the Branch and Bound technique. This algorithm constructs a sequence of relaxed LP subproblems (binary variables are replaced by $0 \leq x_i \leq 1, i = 1, \ldots, N$) attempting to converge to a solution of the BIP [64]. The following subsection describes the branch-and-bound method in greater detail.

### 2.2.1 Branch and Bound

The branch-and-bound algorithm [64, 65] builds a binary search tree in which every node is a solution to a LP-relaxation and each edge represents branching due to a new constraint creating a new sub-problem. The relaxed sub-problems are solved via the simplex method [66].

The method starts from the root node that solves the relaxed original problem. After solving the relaxed BIP at each node, the method chooses a non-integer variable $x_j$ (based on a fixed criterion *e.x.* having the largest fractional part) and splits the problem in two $x_j = 0$ and $x_j = 1$ cases.

The branching continues until reaching a binary solution, an infeasible problem, or a solution with objective value less than the updated lower bound. The lower bound on the objective value serves as a threshold to discard un-improving branches. It is updated per achieving every new largest objective value produced by a binary solution. Then, the algorithm chooses the node with the highest objective function value among all that are available to explore. These stages iterate until reaching a binary solution with the greatest optimal value among the available results.

## 2.3 Assignment Problems

The assignment problem requires the determination of an optimal mapping between elements of two disjoint sets $S_1$ and $S_2$ with cardinalities $n_1$ and $n_2$ via the solution of the following optimization problem:

$$A = \underset{a_{ij} \in \{0,1\}}{\arg\min} \quad \sum_{i=1}^{n_1} \sum_{j=1}^{n_2} c_{ij} a_{ij} \tag{2.18}$$

for non-negative $c_{ij}$s that determine the cost of assigning $s_i \in S_1$ to $s_j \in S_2 \, \forall i = 1, \ldots, n_1$ and $j = 1, \ldots, n_2$. The $a_{ij} = 1$ indicates that $s_i \in S_1$ is assigned to $s_j \in S_2$. Generally, this problem is constrained with $\sum_{i=1}^{n_1} a_{ij} \leq 1$, $j = 1, \ldots, n_2$ and $\sum_{j=1}^{n_2} a_{ij} \leq 1$, $i = 1, \ldots, n_1$ to guarantee an injective and not necessarily surjective correspondence. The inequality in the above constraints allows for "outliers" which are the points that do not match meaningfully to any point in the other set.

The assignment problem is commonly considered in the context of graph theory as a bipartite graph matching problem. One example is shown in Figure 2.5 where the optimal assignment is marked with bolder red links.

In the following subsections, the Hungarian and graduated assignment methods are

$$C = \begin{bmatrix} 4 & 2 & 6 & 2 \\ 3 & 5 & 7 & 1 \\ 1 & 2 & 0 & 2 \\ 2 & 3 & 1 & 5 \end{bmatrix}$$

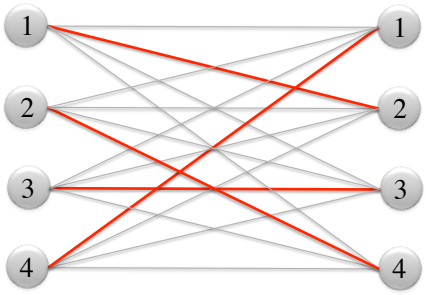


Figure 2.5: The optimal assignment between two sets of four points and for the given cost matrix is shown with the red bolded links.

described that tackle exact (between sets of same size) and inexact (between sets of differing sizes) matching problems respectively.

#### 2.3.0.1 Hungarian Algorithm

The Hungarian algorithm solves the problem of exact or bijective matching meaning that all the elements in each set have to be matched one-to-one. Thus, the following restrictions hold:

$$\begin{aligned} \sum_{i=1}^{n_1} x_{ij} = 1, \quad j = 1, 2, \ldots, n\,, \\ \sum_{j=1}^{n_2} x_{ij} = 1, \quad i = 1, 2, \ldots, n \end{aligned} \tag{2.19}$$

The Hungarian method is founded on two theorems [67]:

**Theorem 1**: If a constant is added to (or subtracted from) every element of any row (or column) of a matrix, the optimal assignment of the new matrix remains intact.

**Theorem 2**: If there exists a solution $x_{ij}, i, j = 1, \ldots, n$ that satisfies $\sum_{i}^{n} c_{ij} x_{ij} = 0$ for non-negative costs, $c_{ij} \geq 0$, it is optimal.

Exploiting the first theorem, the Hungarian algorithm starts with row and column subtraction. First, the minimum entry of every row is subtracted from all the entries of the respective row in $C$. Then, the same operation repeats but for columns. The new $C$ is throughly searched for zero elements starting from the rows or columns that include exactly one zero. The indices of such zero entries are assigned to each other. In the next step, the rest of zeros located on the same row or column with the respective zero are crossed out from further operations. These operations continue successively on rows and columns until all zeros have either been assigned or crossed out. If there is a tie between elements, as happens in the example of Figure 2.5 between the 3$^{\text{rd}}$ and 4$^{\text{th}}$ elements on the

left side and the 1st and 3rd elements on the right side, it can be broken arbitrarily. If the number of assignments equals $n$, the optimal assignment is achieved. Otherwise, the rows and columns including zeros are ignored, and the minimum element will be deducted from all the remained entries. The zeros produced at this stage determine the new assignments. This operation continues until the number of assignments reaches $n$.

#### 2.3.0.2 Graduated Assignment

The graduated assignment (GA) method was first proposed in the context of non-rigid point correspondence problem [75]. This method modifies the $A$ with addition of an extra row and column as shown for example in Figure 2.6 for indexing outliers such that for

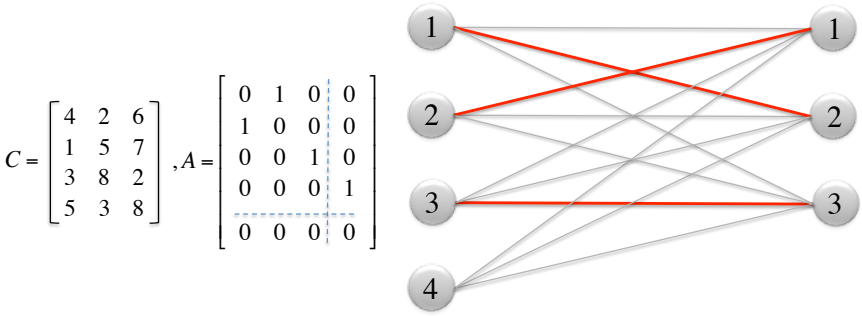


Figure 2.6: The optimal assignment between two point sets of different sizes for the given cost matrix is shown with the red bolded links. The node 4 in the left set is an outlier.

every $s_i \in S_1$ that is an outlier, $a_{i,n_2} = 1$. Also, if $s_j \in S_2$ is an outlier, $a_{n_2,j} = 1$. With the new definition of $A$, the assignment constraints are updated accordingly where $\sum_{i=1}^{n_1} a_{ij} = 1,\ j = 1,\dots,n_2+1$ and $\sum_{j=1}^{n_2} a_{ij} = 1,\ i = 1,\dots,n_1+1$. These constraints imply a slightly relaxed form of doubly stochasticity for $A$. Therefore, the GA method utilizes this fact to relax the binary constraint on the variables and allow them to take continuous values in the $[0,1]$ interval to convexify the optimization domain and avoid the computational burden of the combinatorial problems. It has been proved [110] that the doubly stochastic matrices in general form a convex set with corners that are matrices with binary entries as symbolically shown in Figure 2.7.

The property that differentiates the corners $(P_i, i = 1\dots,6)$ from other points of the convex set is their entropy that is shown by warmness of colors (red regions are associated with matrices with higher entropy). Defining the entropy of a matrix as $-\sum_{i=1}^{n_1}\sum_{j=1}^{n_2} a_{ij}\log a_{ij}$, the binary doubly stochastic matrices possess the lowest possible entropy level. Therefore, the GA method adds an entropy term to the relaxed version of the problem in (2.18) to force

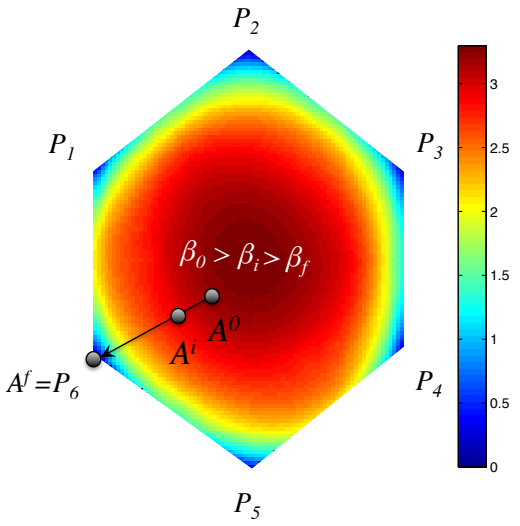


Figure 2.7: Figurative description of annealing process: The assignment matrix starts from regions of higher entropy (continuous valued doubly stochastic matrices that are convex combination of six permutation matrices $P_i, i = 1, \ldots, 6$) depicted by warmer colors and moves toward one of the polytope conners ($P_6$ here) with reduction of $\beta$.

the results to take binary values. The new problem is defined as

$$\begin{aligned} A = \arg\min_{a_{ij}\in[0,1]} \quad & \sum_{i=1}^{n_1}\sum_{j=1}^{n_2} a_{ij}c_{ij} + \beta \sum_{i=1}^{n_1}\sum_{j=1}^{n_2} a_{ij}\log a_{ij}, \\ & \sum_{i=1}^{n_1} a_{ij} = 1,\ j = 1, \ldots, n_2 + 1, \\ & \sum_{j=1}^{n_2} a_{ij} = 1,\ i = 1, \ldots, n_1 + 1. \end{aligned} \tag{2.20}$$

where $\beta$ controls the entropy level of the solution or convexity degree of the optimization problem. The solution moves toward taking binary values as the control parameter decreases. This technique of enforcing bipolarity via a monotonically decreasing regulating parameter is called deterministic annealing and the $\beta$ is referred to as annealing rate.

In the medical image processing field, anatomically-driven features are usually spatially restricted. As a result, to control the biological meaningfulness of the correspondences, there has to be a trade-off between the assignment rate ($\sum_{i=1}^{n_1}\sum_{j=1}^{n_2} a_{ij}$) and the cost functions. This means that even though the problem in (2.20) tends to maximize the number of assignments, it is not desirable to correspond points that have assignment costs larger than a threshold determined by the anatomical specifies and can be set manually by an expert evaluation of data. For example, in the problem of corresponding the junctions of cranial vasculature across different images, an average measure of the minimum distance

between the junctions of individual samples would provide such a threshold. In other words, the point displacements are limited. This threshold is set by a parameter named $\lambda$ here. Embedding this specificity in the assignment problem results in

$$\begin{aligned} A = \underset{a_{ij}\in[0,1]}{\arg\min} \quad & \sum_{i=1}^{n_1}\sum_{j=1}^{n_2} a_{ij}(c_{ij}-\lambda) + \beta \sum_{i=1}^{n_1}\sum_{j=1}^{n_2} a_{ij}\log a_{ij}, \\ & \sum_{i=1}^{n_1} a_{ij} = 1,\ j = 1,\dots,n_2+1, \\ & \sum_{j=1}^{n_2} a_{ij} = 1,\ i = 1,\dots,n_1+1. \end{aligned} \tag{2.21}$$

or equivalently

$$\begin{aligned} A = \underset{a_{ij}\in[0,1]}{\arg\min} \quad & \sum_{i=1}^{n_1}\sum_{j=1}^{n_2} a_{ij}c_{ij} - \lambda\|A(1:n_1,1:n_2)\| + \beta \sum_{i=1}^{n_1}\sum_{j=1}^{n_2} a_{ij}\log a_{ij}, \\ & \sum_{i=1}^{n_1} a_{ij} = 1,\ j = 1,\dots,n_2+1, \\ & \sum_{j=1}^{n_2} a_{ij} = 1,\ i = 1,\dots,n_1+1. \end{aligned} \tag{2.22}$$

where the $A(1:n_1,1:n_2)$ notation means a matrix that equals to $A$ but without the extra last row and column related to the outliers. The negativity of the second term yields the trade-off such that the optimization favors the assignments with costs less than $\lambda$ so that produce negative values and lower the overall cost. On the other hand, the assignments with $c_{ij}$s larger than $\lambda$ that give rise to the cost have to be penalized by receiving null matchings, $a_{ij} = 0$. When $s_i \in S_1$ receives null matchings with all the nodes in $S_2$, it will be detected as an outlier and $a_{i,n_2+1} = 1$. This problem's cost is bounded from below by the doubly stochasticity of the assignment matrix. The Frobenius norm matrices with this condition does not exceed $n_1 \times n_2$ that happens for perfect matchings where $n_1 = n_2$ and there is no outliers. To sum up, the existence of outliers introduces the above-mentioned trade-off and keeps the solution from having the maximal assignment rate (reaching the lower bound).

The approach in [75] uses a combination of soft assign [87] and deterministic annealing [88] techniques to find the optimal solution of this problem. The soft assign method enforces positivity on the $a_{ij}$s using *e.x.* exponentiation. Then, the summation to one constraints are guaranteed by performing iterative row and column normalization operations as suggested in [89] under the name of Sinkhorn technique.

The GA algorithm takes the following steps to achieve the optimal results. First, given the initial assignment matrix $A^0$, the $A$ is updated as

$$a_{ij} = \tfrac{1}{\beta}\exp\left(-a^0_{ij}\tfrac{(v_i-w_j)^T(v_i-w_j)}{2\beta}\right) \tag{2.23}$$

for $i = 1, \ldots, n_V$ and $j = 1, \ldots, n_W$,

$$a_{n_V j} = \frac{1}{\beta_0} \exp\left(-a^0_{n_V j} \frac{(v_i - w_{n_W+1})^T (v_i - w_{n_W+1})}{2\beta_0}\right) \tag{2.24}$$

for $j = 1, \ldots, n_W$, and

$$a_{in_W} = \frac{1}{\beta_0} \exp\left(-a^0_{in_W} \frac{(v_{n_V+1} - w_j)^T (v_{n_V+1} - w_j)}{2\beta_0}\right) \tag{2.25}$$

for $i = 1, \ldots, n_V$.

Using the Sinkhorn technique, the rows and columns are normalized consecutively with the operations

$$\begin{aligned} a_{ij} &= \frac{a_{ij}}{\sum_{j=1}^{n_W+1} a_{ij}}, \quad i = 1, ..., n_V \\ a_{ij} &= \frac{a_{ij}}{\sum_{i=1}^{n_V+1} a_{ij}}, \quad j = 1, ..., n_W. \end{aligned} \tag{2.26}$$

until $A$ converges to a specific form of doubly stochasticity. The result will replace the $A^0$ and the operations in (2.23-2.26) repeat for a lower $\beta_r\beta$ rate.

It is suggested to set the initial value of the $\beta$, $\beta_0$, equal to the largest square distance of all the points across $V$ and $W$ [86] and decrease it with the annealing rate $\beta_r$. The $\beta_r$ controls the convergence rate and robustness (the transition smoothness from continuous to discrete $A$). It is of high importance to set $\beta_r$ with a value that balances between these two operational factors. For the outliers, $\beta_r = 1$. The annealing continues until reaching $\beta_f$ which is set by the average of the squared distance between the nearest neighbors in data sets.

# Chapter 3

# Voting-based Vessel Recovery and Enhancement

Building GGMs requires rough binary representation of vascular images in which artifacts such as noise, non-uniform illumination, and fluorescence backprojection are suppressed. In this chapter, we explain the basics of a vessel extraction process from 3-D fluorescence microscopy images that efficiently delivers such desired segmentation. There are two primary components to this process: initialization and vessel recovery. Basis of the extracted structure is founded in the initialization stage, and the full vasculature is formed recursively in the vessel recovery part. Details of each process are provided in the following sections. The notations in Table 3.1 will be used for the rest of this chapter.

Table 3.1: Notations used for the vessel recovery process.

| | |
|---|---|
| $I$ | Grayscale image |
| $\rho_1$ | Smallest radius of all the vessels |
| $\rho_2$ | Largest radius of all the vessels |
| $m_s$ | Median filtered $I$ by small scale kernels |
| $m_l$ | Median filtered $I$ by large scale kernels |
| $\nabla$ | First order finite difference approximation to gradient operator |
| $\|.\|$ | Euclidean distance |
| $\oplus$ | Morphological dilation |
| $\ominus$ | Morphological erosion |
| $sph_1$ | Spherical structural element of radius 1 |

## 3.1 Initialization

We propose a two scale kernel-based method to determine a set of seed points for further processing. This initialization approach is similar to the ideas in [90] where signals are detected by thresholding mean-to-mean ratio of different kernels. However, the complex nature of artifacts in the data of interest calls for a more effective measure. Rank-ordered statistical filters are an efficient choice here for their robustness (effectiveness in suppressing Poisson and shot noise [91]) and low computational cost. The most well-known of this group is the median filter that balances noise reduction and over smoothing which is an inevitable by-product of majority of the denoising methods that causes blurred edges and lowered contrast [92]. We have observed that median values of concentric kernels (cubes) of two different scales (side length) differ markedly if the center point is located on the microvasculatures. Microvasculature is of a spatially sparse structure, thus the median value of the smaller kernel $m_s$ even if the vessels are faint in intensity will be significantly higher than the median value of the larger kernel $m_l$ in which lower intensity background voxels will dominate. Therefore, this feature is robust to non-uniform illumination where median of kernels are analyzed locally.

Four cases of bright vessel (A), noisy background (B), faint vessel (C), and dark background (D) are specified on maximum intensity projection (MIP) of a 3-D image in Figure 3.1 to illustrate this intuition. Histograms for the intensity distribution of the points located in the kernels of scales $s$ (small) and $l$ (large), $s < l$, are shown on the right side of the figure where median values are marked by blue and red diamond topped bars for small and large scale kernels. For background points, these values either do not differ considerably or the median in the larger neighborhood exceeds the smaller neighborhood in the proximity of other microvasculature. Therefore, the ratio obtained from the median filtered images using kernels of $s \times s \times s$ and $l \times l \times l$ size, centered on voxels $(x, y, z) \in I$, where $m_l(x, y, z) \neq 0$ delivers a well-separable set of feature points by clustering of which one can obtain robust seed points $\Gamma_0$ regardless of the mixed-noise, non-uniform illumination, and other imaging artifacts. One example of this ratio that is calculated for 2-D slice of the image in Figure 3.1 is shown in Figure 3.2. According to this figure, dimmer vessels especially in the lower and upper left corners have received larger $\frac{m_s}{m_l}$ levels (visualized by larger intensity values).

Non-uniformity of vessel sizes and noise variance over the data gives a range of values to the $\frac{m_s(x,y,z)}{m_l(x,y,z)}$ ratio. However, a good selection of $s$ and $l$ ensures the least overlap between the clusters. Here, $s$ and $l$ are selected based on the vessel radius measurements obtained

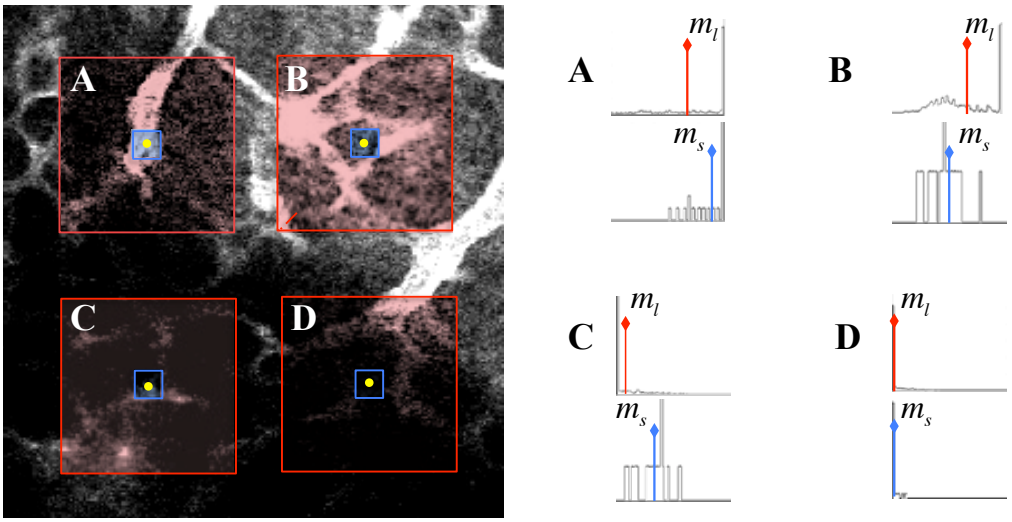


Figure 3.1: Four different classes of voxels observed in the original data are indicated here: Bright vessel (A), noisy background (B), faint vessel (C), and dark background (D). Histograms for the intensity distribution and the median value of the points located in the $s$ and $l$-scale kernels are shown on the right side. Diamond topped bars mark median values on the histograms. Distinguishable comparative situation of median values is used as the basis for detecting relevant structures.

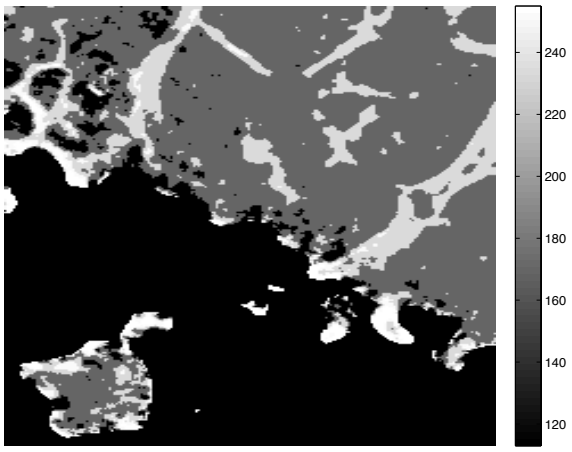


Figure 3.2: The $\frac{m_s}{m_l}$ ratio obtained from the median filtered images using kernels of $s \times s \times s$ and $l \times l \times l$ size for pixels with $m_l \neq 0$.

from the image $I$. The $s$ is set as the smallest vessel radius, $\rho_1$, to ensure the preservation of small structures. In order to balance locality and inclusiveness, $l$ is chosen as twice the largest vessel diameter, $4\rho_2$. This amount allows for the incorporation of enough background and vasculature in the larger box. The radius at each foreground point in $I$ is estimated by means of the method used in [40]. We first compute the ratio for all points, run $k$-means

($k = 2$) clustering [57], then set the $\Gamma_0$ as the voxels in of the larger centroid cluster. Finally, to guarantee the structural enhancement besides recovery of faint vessels, $\Gamma_0$ is augmented by inclusion of the points that are located in the brightest regions as they may not pass the 2-means thresholding in the highly noisy regions (where $m_l$ is also large):

$$\Gamma_0 = \Gamma_0 \cup \{(x, y, z) | m_s(x, y, z) = max(m_s)\}. \tag{3.1}$$

## 3.2 CREVER: Constrained Region Evolutionary Vessel Enhancement and Recovery

Given the detected seed points, $\Gamma_0$, we recover the entire structure through a novel method termed "CREVER". The CREVER technique eliminates the need for first denoising and then segmenting images in a recursive region-growing approach that rejects imaging imperfections simultaneously. This method is developed based on the observation that microvasculature's local median intensity typically decreases as the central point moves away from the centerlines. Figure 3.3 illustrates this claim on the mesh plot of a 2-D grayscale slice of a median filtered microvasculature image. The structured ridges marked by the brightest shades belong to the microvasculature. The brightness decreases smoothly as the filter kernel is moving away from the vessels centerline. Then, it drops abruptly by reaching the blood vessels boundaries. Isolated bright spots in the background are image artifacts.

The number of iterations, $N$, in the CREVER method is determined by the cardinality of the monotonically decreasing sequence $\delta_1 = max(m_s), \delta_2, \ldots, \delta_i = \delta_{i-1} - 1, \ldots, \delta_N = min(m_s)$ (line 3 of the CREVER pseudocode). At the $i^{th}$ iteration, new voxels are voted as part of the structure when they satisfy three constraints: adjacency to the retrieved regions, having median intensity of equal or greater than the one determined by the iteration number ($m_s \geq \delta_i$), and having a low normalized absolute gradient value ($I_g = \frac{|\nabla m_s|}{\|m_s\|} < \tau$) (line 10) where

$$\nabla m_s = \frac{\partial m_s}{\partial x}\hat{i} + \frac{\partial m_s}{\partial y}\hat{j} + \frac{\partial m_s}{\partial z}\hat{k}. \tag{3.2}$$

The last criterion prevents leakage across vessel boundaries. Finally, to avoid missed detections caused by imaging artifacts in the microvasculature, retrieved regions are morphologically closed at each step using a spherical structuring element of radius one (line 11). Selection of $\tau$ has an important role in the method's overall performance. For a small $\tau$, region growing will be halted prematurely, and some regions will be missed. On the other hand, for a $\tau$ that is too large, many of the noisy background voxels will be included in the

**Algorithm 1** CREVER

**Inputs:** Grayscale image $I$, $\rho_1$, and $\rho_2$
**Initialization:**
$m_s \leftarrow$ Median of $I$ in $s \times s \times s$ kernels
$m_l \leftarrow$ Median of $I$ in $l \times l \times l$ kernels
Sequence: $\delta_1 = max(m_s), \delta_2, \ldots, \delta_i = \delta_{i-1} - 1, \ldots, \delta_N = min(m_s)$
$\Gamma_0 \leftarrow 2 - \text{means clustered}(\frac{m_s}{m_l}),\ m_l \neq 0$
$\Gamma_0 \leftarrow \Gamma_0 \cup \{(x,y,z)|\ m_s(x,y,z) = \delta_1\}$
$\Gamma_{old} \leftarrow \Gamma_0$
$n \leftarrow 1$
$I_g = \frac{\nabla m_s}{\|\nabla m_s\|}$
**while** $n < N$ **do**
    $\Gamma_{new} \leftarrow \Gamma_{old} \cup \{(x,y,z)|m_s(x,y,z) \geq \delta_{n+1}, \|\Gamma_{old},(x,y,z)\| \leq \sqrt{3},\ |I_g(x,y,z)| < \tau\}$
    $\Gamma_{old} \leftarrow (\Gamma_{new} \oplus sph_1) \ominus sph_1$
    $n \leftarrow n + 1$
**end**
$I_B \leftarrow \Gamma_{old} > 0$
**Output:** $I_B$

retrieved vasculature. This parameter is set as the mean of two clusters centroids found by the 2-means clustering of $I_g$ to avoid either of these deficiencies.

Figure 3.4 shows an example of the microvasculature segmentation via the CREVER

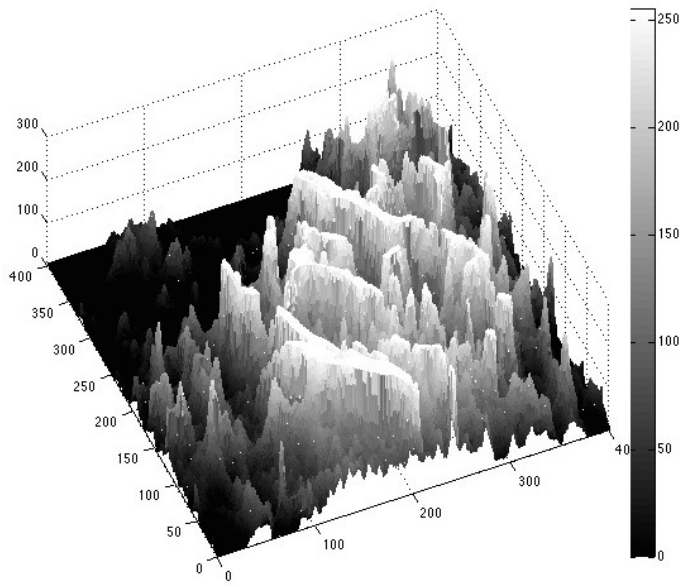


Figure 3.3: Mesh plot of a 2-D slice of a locally median filtered fluorescence microscopy image. Structured ridges marked by the brightest shades belong to the microvasculature.

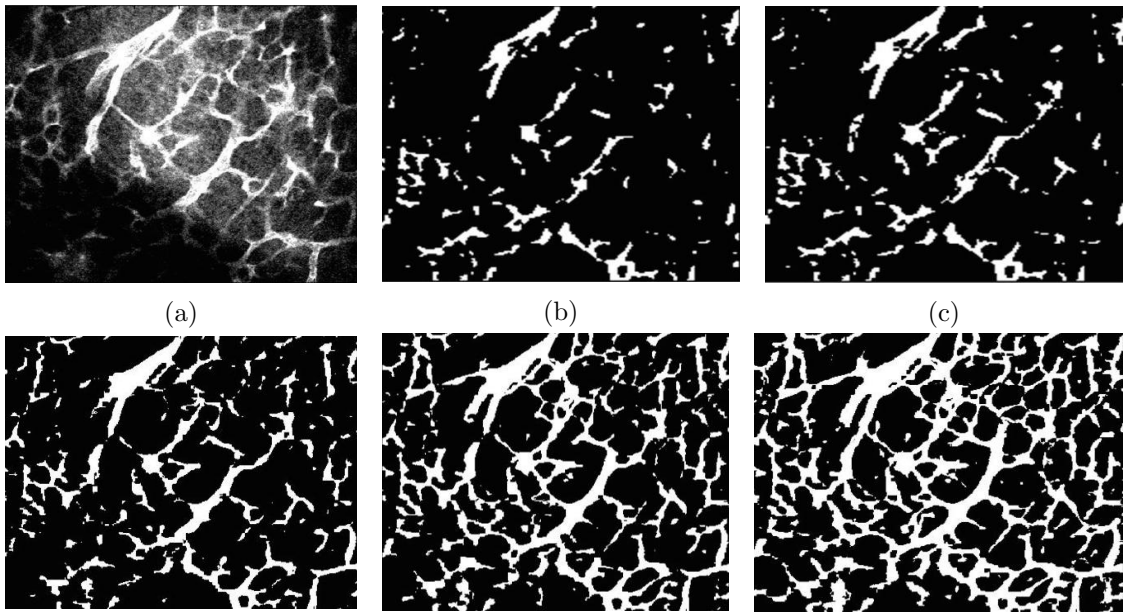


Figure 3.4: (a) A slice of an original 3-D fluorescence microscopy image, (b) seed points, recovered microvasculature at (c) 25, (d) 50, (e) 75, and (f) 100% of the CREVER method's development.

method for a 2-D slice of a three dimensional fluorescence microscopy image from iteration 0 (seed points) to the last iteration. The final image demonstrates the accurate recovery of structures from noisy, artifacted, and low contrasted areas. To be specific, the results obtained for the lower left part of the image supports this claim. Inhomogeneous illumination greatly lowers the visibility of the vasculature in this part that is the reason of being missed by other denoising-segmenting methods as it will be shown in Section 3.2. Since the computations are done in cubic kernels, some of the structural content from the above and below slices of the current one are included in the enhancement process, which is the reason for having a slightly more complete structure than the original image in the final result. Processing in the cubic regions is the key feature of CREVER in reducing vessel breakages and improving the accuracy.

## 3.3 Experiments

In this section, efficiency of the proposed method is assessed. First, the quantitative performance measures are calculated using synthetic data and the ground truth. Next, the vessel enhancement power is qualitatively shown and compared with other relevant methods using

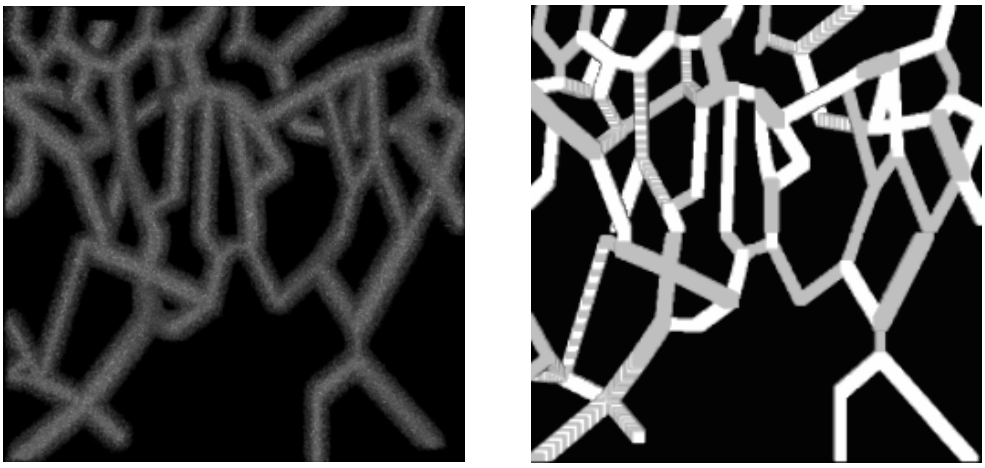

(a) (b)

Figure 3.5: (a) MIP of synthetic image with PSNR= 5 dB and (b) the segmentation obtained by the CREVER method.

real data. Finally, we investigate the effect of parameters on the performance of the method.

### 3.3.1 Quantitative analysis

To conduct the quantitative evaluations, a set of synthetic images are generated from a single structure corrupted by varying amounts of noise to simulate different SNRs. In detail, a synthetic image is formed by developing an interconnected tubular network from a specific ground truth graph similar to the approaches discussed in [93] using the same parameter values. This structure is shown in Figure 3.5(a). The volume obtained from CREVER are provided in Figure 3.5(b). All the images are shown in their MIPs. To achieve a target PSNR (peak signal-to-noise ratio), a common approach in Poisson noise assessment literature [17, 94] is used that is based on scaling the maximum intensity of image defined as

$$PSNR = 10\, log_{10}\left(\frac{I_{max}^2}{MSE}\right)(db) \tag{3.3}$$

with MSE being the mean square error between the noisy and noise-free versions. For the following experiments, PSNR levels are changed from 2 to 15 dB in ten steps. For each PSNR, experiments are repeated ten times and the average is reported as final result. Then, performance of five segmentation and binarization methods are compared with the CREVER: the level-set method [21] applied to locally normalized data (details are provided in [93]), Otsu [61] derived binarization of the denoised images obtained by the Candle method [95], non-local mean filtering with combination of the variance stabilizing Anscombe

transform [16], non-local median filtering [96], and finally Wiener filtering [97]. The true positive rate ($TPR$) or sensitivity and false positive rate ($FPR$) or (1-specificity) calculated as below

$$TPR = \frac{\text{Number of correctly detected foreground voxels}}{\text{Number of true foreground voxels}},$$
$$FPR = \frac{\text{Number of falsely detected foreground voxels}}{\text{Number of true background voxels}} \tag{3.4}$$

are used to draw the receiver operating characteristic (ROC) curves of these methods, shown in Figure 3.6, applied to the synthetic data. Results suggest that CREVER is superior in

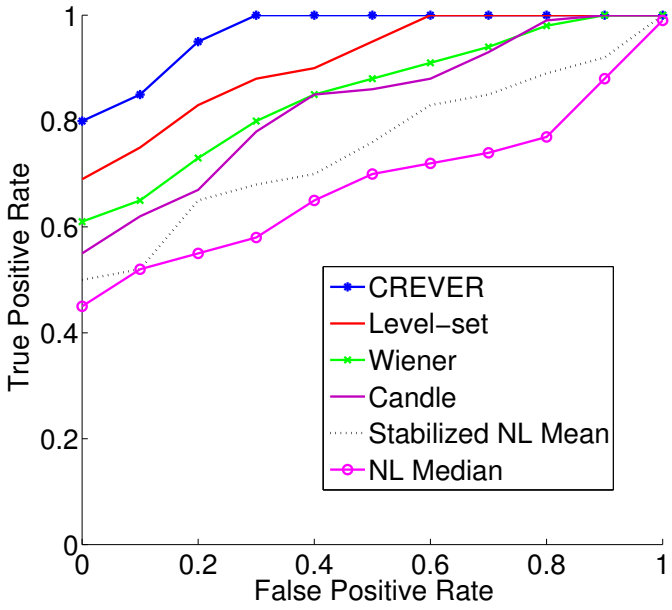


Figure 3.6: The ROC curves obtained using the proposed method (CREVER), level-set method initialized on locally normalized images, Otsu segmentations of the denoised images by Candle, non-local median filtering, stabilized non-local mean denoising by the Anscombe transform, and Wiener filtering algorithms using synthetic images with PSNRs in the range of 2 to 15 dBs.

performance having the largest area under curve (AUC). Besides a high level of $TPR$, this method performs very well in rejecting background artifacts as measured by low false positive rates. Level-set method provides the next best performance behind CREVER. Binarization of the Wiener filter, Candle method, stabilized non-local means, and non-local median denoising algorithms with th eOtsu's method perform worse than CREVER.

### 3.3.2 Comparative qualitative analysis

Qualitative validation of the proposed algorithm has been completed by applying it to three sets of 3-D vascular images from murine nervous tissue. Testing datasets were selected such that they show a range of structural and noise properties. To generate these data, heterozygous Plexin-D1-fGFP transgenic mice were used to visualize GFP-expressing developing blood vessels in the embryonic thalamus. All animals were maintained and treated with approved Institutional Review Board protocol according to the National Institutes of Health guidelines and approved by the Institutional Animal Care and Use Committee at Harvard Medical School. Three dimensional vascular images ($z$-stacks) were acquired using a Leica LSM 510 META confocal microscope in embryonic thalamus. The SNR of images ranges from 3 to 7 dB roughly.

The first image, of size $200 \times 450 \times 50$ voxels, is shown in Figure 3.7(a) with MIP where the MIP of its segmentation obtained by the CREVER method is also shown in Figure 3.7(b). The next data is obtained from a more homogenous (in vessel shape and size senses) microvascular network. However, the noise distribution differs markedly throughout the image as apparent from Figure 3.7(c). This image is of size $500 \times 500 \times 45$ voxels. The segmented image is shown in Figure 3.7(d). This image has been collected from a thinly cut layer of tissue, thus isolated points are formed from recovery of those partial structures. The last dataset that is of size $400 \times 400 \times 50$ voxels incorporates a spatially dense microvascular network with high noise content apparent in the original image shown in Figure 3.7(e). However, the segmentation presented in Figure 3.7(f) proves stability of the CREVER in presence of strong noise and artifact elements. The CREVER method has recovered the vasculature regardless of its local statistical variations, noise level, and structural properties such as vessel radius measure. Considering all cases, it is obvious that the proposed method produces an overall high quality segmentations of microvasculature from 3-D fluorescence microscopy images. It well preserves the structural specifications such as continuity and smoothness of the vessel boundaries while noticeably removing imaging artifacts and noise.

Carrying on to the qualitative evaluation of CREVER, it is compared with the five denoising/segmentation algorithms mentioned in Section 3.3.1 applied to the image in Figure 3.4(a). The segmentation obtained from CREVER is shown in Figure 3.8(a) where denoised images are shown in Figure 3.8(c,e,g,i) and segmented versions are shown in Figure 3.8 (d,f,h,j). These figures suggest that CREVER provides a superior result. The results also show that the denoising methods tend to over-smooth the image especially in lower SNR parts. As a result, small or low resolution structures will be missed and false negative

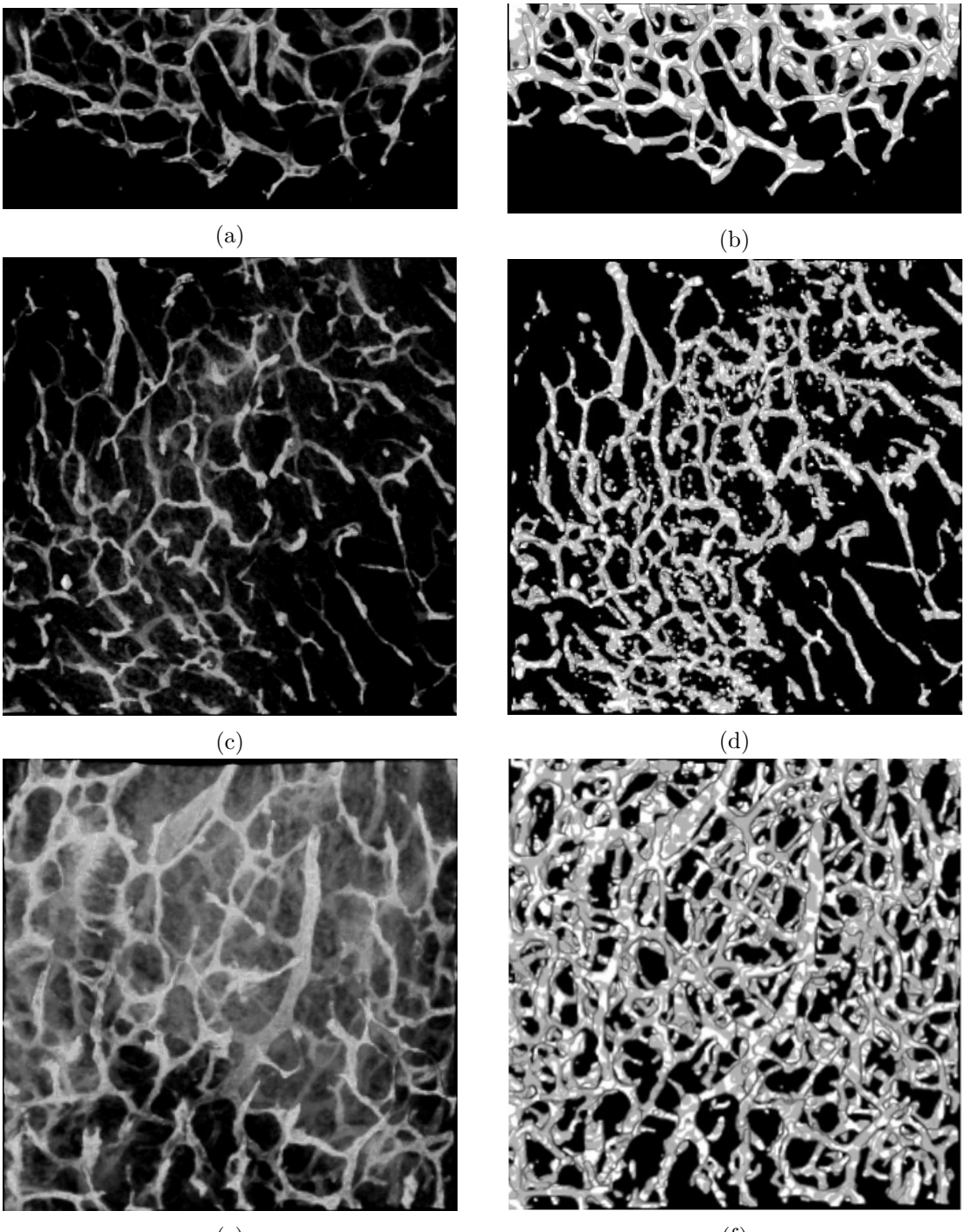

(a) (b) (c) (d) (e) (f)

Figure 3.7: (a,c,e) The MIP of real data sets and (b,d,f) their segmentations obtained via the CREVER method.

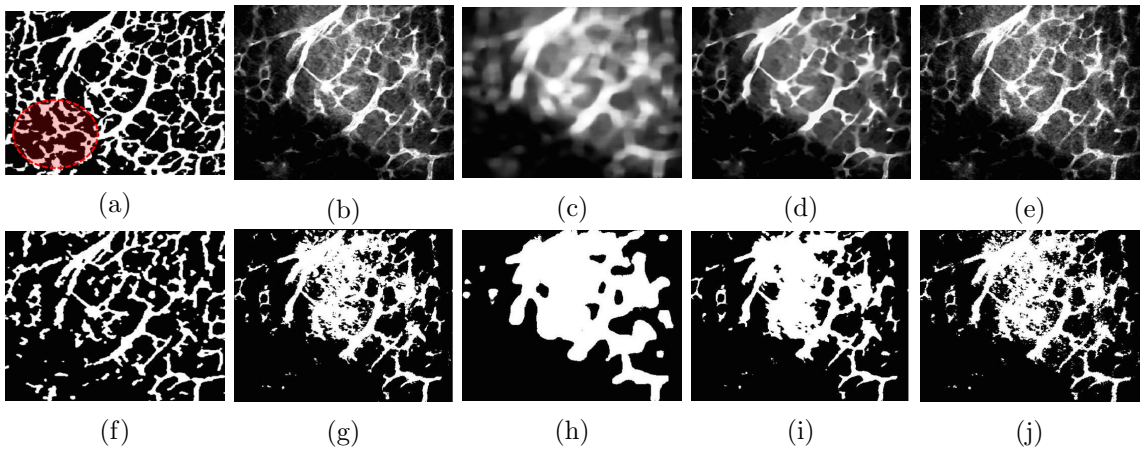


Figure 3.8: (a) Segmentation of Figure 3.4(a) obtained via the CREVER, denoised images (b,c,d,e) and their Otsu derived segmentations (g,h,i,j) acquired by Candle algorithm, non-local median filtering, non-local mean filtering of the Anscombe transformed image, and Wiener filtering respectively, and (f) level-set method initialized on the locally normalized image.

rate increases as opposed to the CREVER method that recovers the vasculature in a more non-selective manner regarding illumination uniformity, contrast level, and vascular size being more robust to image artifacts. This effect is specifically more discernible in the left and lower left parts of the images marked by a red dashed circle on Figure 3.8(a).

The computational complexity of the CREVER method is dominated by the median filtering's cost that is in turn dependent on the larger kernel size, $\mathcal{O}(l^3)$. Since $l$ is dependent on the largest vessel radius in the given data, computational complexity is consequently relative to the imaged tissue's vasculature measure. The iterations count in the CREVER part however, is data independent and is bounded by the maximum voxel intensity of the data. Finally, this method scales to data of arbitrary size as all the operations are parallelizable for disjoint partitions from an image.

### 3.3.3 Parameter analysis

In section 3.1, it was shown that parameters $s$ and $l$ are set by approximations of the smallest and largest vessel radii. Here, we show that these assignments are optimal and show that deviation from these values deteriorates the performance. Figure 3.9 shows the mesh plot of the segmentation accuracy ($ACC$) metric defined as

$$ACC = \frac{TPR + TNR}{TPR + TNR + FPR + FNR} \tag{3.5}$$

where $TNR$ and $FNR$ are true and false negative rates. The $ACC$ is measured over the segmentations obtained from the synthetic image in Figure 3.5(a) vs. varying $s$ and $l$ values where vessel radius ranges from $1(=\rho_1)$ to $4(=\rho_2)$ in the synthetic image. This plot shows that the best $ACC$ is achieved when the parameters are around the same ratio of the vessel radii as discussed in Section 3.1, $s = 1(=\rho_1)$ and $l = 15(\approx 4 \times \rho_2)$.

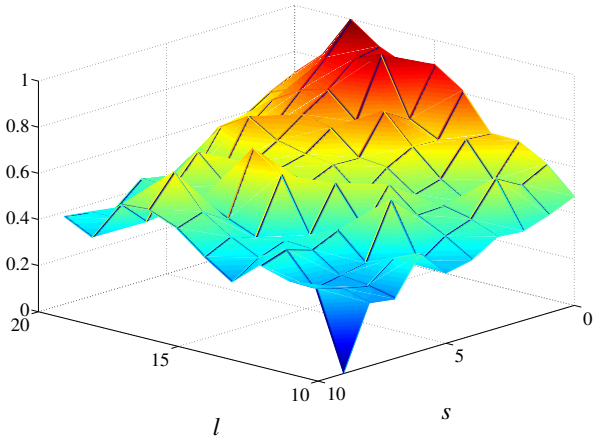


Figure 3.9: Mesh plot of the $ACC$ obtained from segmentations of the synthetic image in Figure 3.5(a) vs. $s$ and $l$.

# Chapter 4

# Geometrical Graph-based Model Identification of Histological Tubular Structures

A geometrical graph-based model is comprised of a collection of nodes representing critical points along with the edges that stand for the piece-wise linear parts of vasculature. In this chapter, it will be shown how these features are extracted from a rough segmentation of the vasculature.

## 4.1 Critical Points Detection

Critical points (CPs) are intended to capture locations of significant structural change in the microvasculature. These locations are where vessels either branch or significantly bend. Here, we refer to branch points as *junctions* and points of significant bending as *waypoints*[1]. The CP detection process is comprised of three stages: convexity filtering, CP clustering, and branching node detection. Figure 4.1 illustrates the essence of each of these steps.

### 4.1.1 Convexity filtering

By relating the primary geometric structure of CPs to the non-convexity of the vasculature in their vicinity, we obtain an easy and effective method for identifying groups of points as potential CPs as shown in Figure 4.2. In this figure, we show three typical cases of

[1] In constructing our vascular graph, these waypoints basically allow for a piecewise linear approximation of the vasculature.

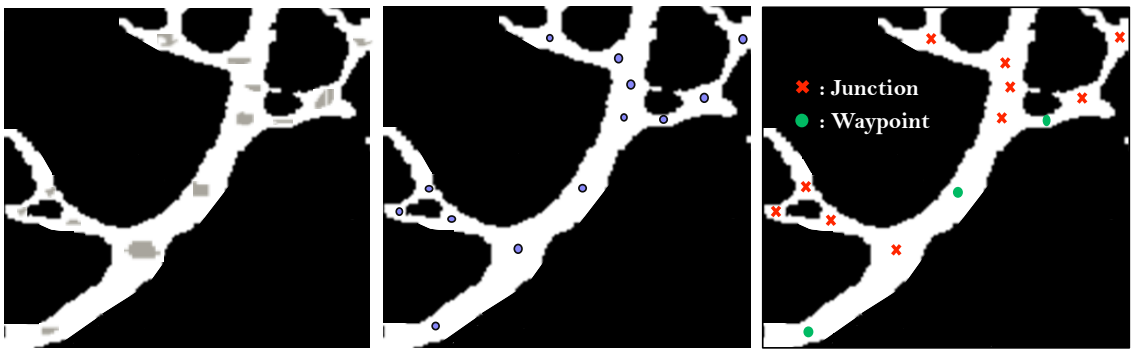


(a) Convexity filtered patches (b) CPs (c) CP differentiation

Figure 4.1: Critical points detection process: (a) Detected critical point patches obtained by convexity filtering, (b) Clustered patches and identified CPs as the clusters' centroids, (c) Junctions are identified through the spherical shell filtering and marked by crosses where waypoints are shown by disks.

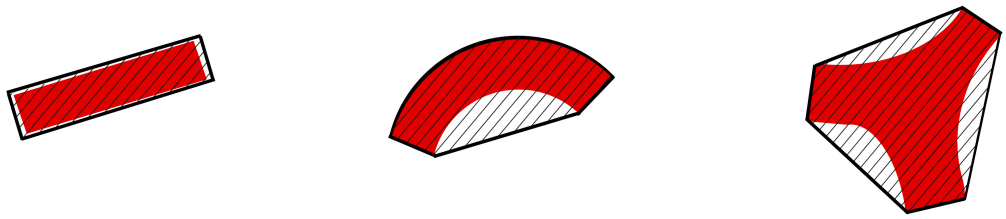

(a) (b) (c)

Figure 4.2: Three types of vessel deformation with their convex hulls: (a) Non-changing (Straight): $H \approx 1$, (b) Bending (Waypoint): $H > 1$, and (c) Branching (Junction): $H \gg 1$.

vasculature geometry model and their associated convex hulls. For the straight vessel in Figure 4.2(a), there is negligible difference between the vessel and its convex hull. For the bending vessel in Figure 4.2(b) as well as the junction in Figure 4.2(c), the convex hull volume, $v_{cx}$, differs markedly from that of the vascular structure, $v$.

The convex hull of a groups of non-zero voxels in a binary image is easily determined and provides a reliable means for determination of structural deformation. Best tailored for low quality images cases, this approach does not require an explicit segmentation and smooth discretization of the vasculature surface. Thus, we define a convexity metric as $H = \frac{v_{cx}}{v}$ that is computed in small neighborhoods of every foreground points in the binarized image, $I_B$, to find the CPs.

For this purpose, we start by computing the $H$ over cubes of width $a$. The quantity $v_{cx}$ is then the number of voxels in the convex hull of the foreground points and $v$ is the volume of foreground points in the cube. We let $a = 4\rho$ where $\rho$, the nominal vessel radius measured in voxels, is estimated using the method proposed in [40]. This value of $a$ allows for inclusion of enough structure of interest in the cube and exclusion of the neighboring vessels for more precise results. Critical points are then defined to be those points whose convexity metric is above a threshold that is automatically determined using Otsu's method applied to the entire data set.

### 4.1.2 Critical point clustering

Convexity filtering results in a collection of voxels in the vicinity of each CP that may not be necessarily connected due to the image imperfections or closeness of two CPs resulting in merged patches. Thus, hierarchical agglomerative clustering [63] is employed to cluster these voxel collections. The CPs are then defined as the center of these clusters. This method is particularly useful for our application as it does not require prior knowledge about the number of clusters and forms clusters based entirely on the distances between voxels. As illustrated in Figure 4.1, without clustering, each patch of filtered voxels would produce a CP resulting in multiple points associated with a single junction or waypoint and missed CPs in the case of merged patches. Therefore, this step increases robustness to image artifacts and makes the overall performance more accurate in finding the CPs location. This process is illustrated in Figure 4.3 where the white pixels are convexity filtered voxels, dashed circles indicate their formed clusters, and the set of CPs are marked by crosses. In this example, agglomerative clustering successfully has distinguished CPs in spite of the patches' discontinuity.

In the experiments, Euclidean distance is chosen as the dissimilarity measure, and the dissimilarity threshold is set equal to the diameter of the vessel to which the voxels belong. This threshold value provides results within an acceptable structural resolution.

### 4.1.3 Branching node detection

Finally, in preparation for the graph construction described in Section 4.2, CPs are divided into disjoint groups of junctions and waypoints. Junctions are distinguished by an improved version of the spherical shell filtering method employed in [98]. This approach is based on the geometrical fact that part of the vasculature masked with a 3-D spherical shell, $\{x | r_1 \leq |x - x_0| \leq r_2\}$, with inner radius $r_1$ (greater than the vessel radius), center point

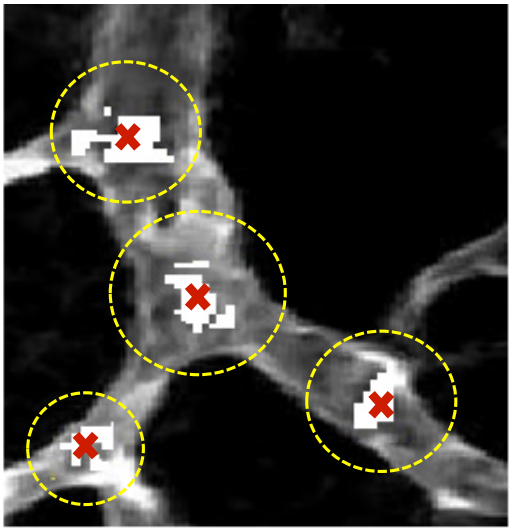

Figure 4.3: Convexity filtered voxels are shown by white patches overlaid on MIP of a real data. In three out of the four cases we see multiple, disconnected patches that are clearly associated with the same CP. Agglomerative clustering provides a single representation of these patches and associates a CP (cross mark) to each of the clusters.

$x_0$, and the outer radius $r_2$ is comprised of three or more connected components within the shell volume where it is concentric with a junction. Indeed, in Figure 4.4 we see in cases "a" and "b," that the number of connected components is three for nominal junctions with three branches while case "c," a CP located at a waypoint, gives rise to two connected components.

Parameters $r_1$ and $r_2$ are set as $\rho$ and $\rho+\delta_\rho$, where $\rho$ is the nominal vessel radius determined in the convexity filtering step, and $\delta_\rho$ is the shell thickness. Due to the compactness of the microvasculature, it is possible that parts of neighboring vessels will be included in the spherical shell masked regions of a point. This proximity results in false junction detections caused by a rise in the number of connected components produced by the spherical shell filtering. One instance for this problem is the case "d" in Figure 4.4, where the number of masked connected components is three due to the presence of a structure from a neighboring vessel in the spherical shell region. To avoid false junction detection, we only need to ensure that the number of connected components in the larger sphere does not exceed one. Finally, collections of junctions and waypoints are denoted with $J = \{j_k, k = 1, ..., n_J\}$ and $W = \{w_l, l = 1, ..., n_W\}$ where $n_J$ and $n_W$ are the number of junctions and waypoints respectively.

### 4.1.4 Boundary points

It is necessary to supplement the junction and waypoint sets with an additional set of boundary nodes defined as the center of vessel cross sections at the boundaries of the image. As seen in Figure 4.5, such structures are typically circular except in cases where a boundary divides a vessel along its length. To separate these two classes, Frangi's vesselness measure [99] is used to find the non-vessel shapes and the Eucleadian centers of the resulting regions signified by $R = \{r_i, i = 1, ..., n_R\}$ are taken as border points where $n_R$ is their overall count. The final CP set is defined to be $P = J \cup W \cup R$ and its cardinality is $n_{CP} = n_J + n_W + n_R$.

## 4.2 GGM Identification

Given CPs identified in Section 4.1, graph-based model identification is formulated as a BIP problem. Designed for the graph extraction problem, binary variables represent the possible edges in the geometrical graph. The set of edges is denoted as $E = \{e_l, l = 1, 2, ..., n_E\}$ where $n_E = \binom{n_{CP}}{2} = \frac{n_{CP}(n_{CP}-1)}{2}$ is the number of possible edges of a complete graph built

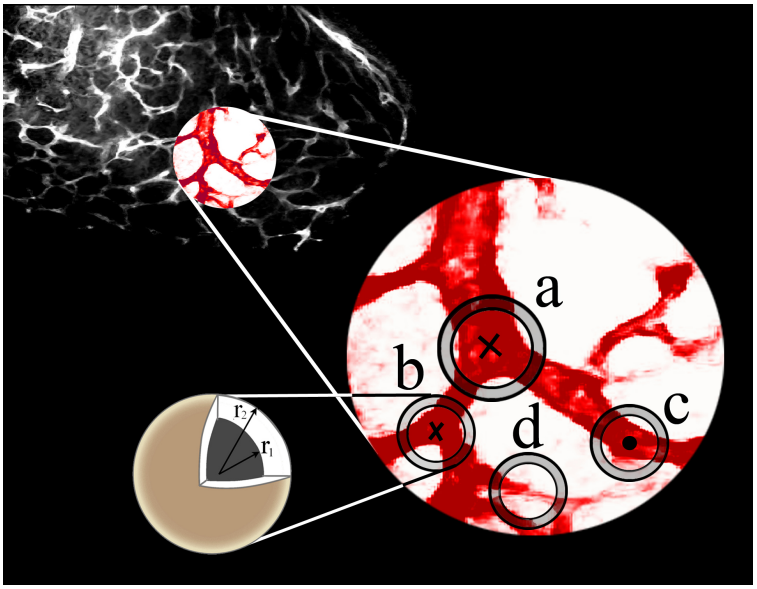


Figure 4.4: Critical points are divided into junction (crosses) and waypoint (circles) groups based on the number of connected components, darker red regions located on the spherical shells, made by the spherical shell filtering. An example of a non-junction point with three connected components in its masked spherical shell neighborhood is provided in the case "d". Presence of more than one connected component in the larger sphere causes dismissal of the point from being declared as a junction.

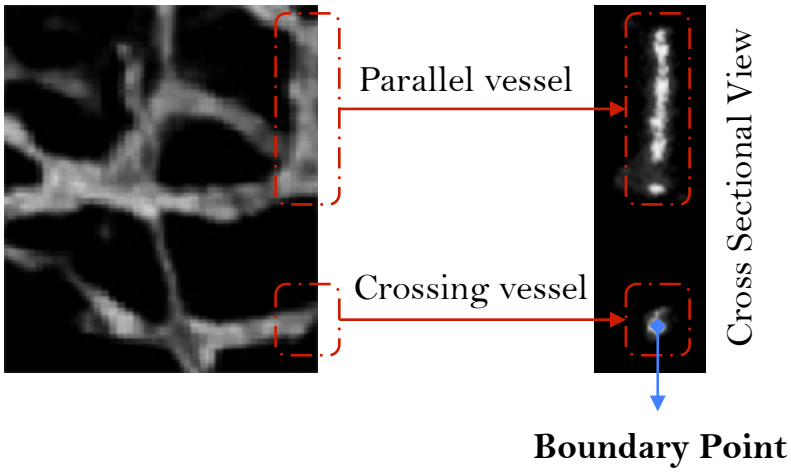


Figure 4.5: Front (on the left) and side (on the right) view of parallel (upper) and non-parallel (lower) vessel cross sections at an image edge.

from the pair of points picked from CPs. The BIP problem finds a subset of edges that best form the microvasculature network's skeleton model via

$$\arg\max_{e_l} \sum_{l=1}^{n_E} \alpha_l e_l$$

$$\text{s.t.} \quad e_l \in \{0,1\},$$

$$\sum_{e_l \in E_{J_i}} e_l \geq 3 \quad , \quad \sum_{e_l \in E_{W_j}} e_l = 2,$$

$$l = 1,2,...,n_E \quad i = 1,2,...,n_J \quad j = 1,2,...,n_W. \tag{4.1}$$

The utility function $\alpha_l$ associated with edge variable $e_l$ is defined to quantitatively capture structural information from the binarized image such as the degree to which an edge is localized on and aligned with the vasculature. The constraint $\sum_{e_l \in E_{J_i}} e_l \geq 3$ ensures that the degree of a junction is greater than or equal to three where $E_{J_i}$ is the collection of edges attached to node $j_i \in J$. Similarly, the constraint $\sum_{e_l \in E_{W_j}} e_l = 2$ ensures that the degree of a waypoint is strictly equal to two where $E_{W_j}$ is the collection of edges attached to node $w_j \in W$. The utility function $\alpha_l$ is defined as

$$\alpha_l = \alpha_{L,l} + \alpha_{A,l} + \alpha_{S,l} \tag{4.2}$$

where three components of $\alpha_{L,l}, \alpha_{A,l}$, and $\alpha_{S,l}$ stand for vessel Localization, vessel Alignment, and Shortcutting degree (to be defined below) of each edge.

The first element $\alpha_{L,l}$ is intended to provide high utility for edges passing through the

microvasculature itself as opposed to the background and is analytically modeled as

$$\alpha_{L,l} = H_\zeta \left( \frac{\|I_l\|_1}{d_l} \right) \left( \frac{\|I_l\|_1}{d_l} \right) \tag{4.3}$$

where $I_l$ is a vector comprising the intensity profile along the $l^{th}$ edge in the binary image $I_B$, and $d_l$ is that edge's Euclidean length. Equation (4.3) is motivated by the fact that microvasculature network is a collection of tubular, or generally, elongated structures. In such a setting, a possible edge passes through background, cuts through cross-section of multiple vessels, or stands mostly on a vessel. Thus, averaged binary intensities along each edge, $\frac{\|I_l\|_1}{d_l}$, is expected to be around zero for the first two cases or one for the latter cases. The function $H_\zeta(x)$ defined as 1 if $x > \zeta$ and zero else, is required to exclude highly unlikely edges, *i.e.*, those of the first two varieties from the computations. This function increases the utility when an edge is located on vascular regions ($\frac{\|I_l\|_1}{d_l}$ increases). Otherwise, the first term in (4.3) goes to zero. Taking this into consideration, we take the threshold $\zeta$ as the mean of the two cluster centroids found by $k$-means ($k = 2$) clustering of the set $\{\frac{\|I_l\|_1}{d_l}\}$.

The quantity $\alpha_{A,l}$ is motivated by two factors. First, due to the imperfections of fluorescence microscopy data discussed in Chapter 1, many smaller vessels manifest as faint and narrow structures in the image such that their accumulative intensity and consequently $\alpha_{L,l}$ are quite small. Also, while the enhancement improves dim vessels' presentation, it still fails to provide a detailed approximation of the vasculature. Most notably, many vessels remain broken. These structures would be undervalued in terms of $\alpha_{L,l}$ and ultimately missed in the creation of the graph-based model. Second, for large vessels, two nodes that do not belong to the same edge may be located close enough to one another resulting a large $\alpha_{L,l}$. Such a situation is illustrated in Figure 4.6 by means of a dashed red line where the true graph edges are shown by gray solid lines. Here, the directional filtering component is designed specifically to overcome these issues by selecting edges in a manner that reflects the underlying directionality of the structure in the vicinity of the potential edges. This alignment of potential edge with the corresponding vessel ensures accuracy of the final result as an estimation of the skeleton.

To obtain the local directionality information, direction filtering ideas are implemented using 3-D steerable filters [100] and $\alpha_{A,l}$ is defined as

$$\alpha_{A,l} = \frac{E_{str,l}}{d_l} \tag{4.4}$$

where $E_{str,l}$ is the energy or Frobenius norm of the directional filter's output calculated in a tubular region around the $l^{th}$ edge from the binarized image defined as

$$\bar{I}_l = \{(x, y, z) | \text{Euclidean distance}((x, y, z), l^{th} \text{ edge}) < \frac{(\rho_1 + \rho_2)}{2}\} \tag{4.5}$$

with $\rho_1$ and $\rho_2$ being the local vessel radii at two ends of the $l^{th}$ edge computed from $I_B$. The energy measures the alignment of the structure in that region of interest (ROI), $\bar{I}_l$, with the edge and is calculated as $E_{str,l} = \|R_2^{\theta,\phi}\|_2^2$ with

$$R_2{}^{\theta,\phi} = \left[H_2^{\theta,\phi} * G\left(\frac{x}{\sqrt{2}\sigma_G}, \frac{y}{\sqrt{2}\sigma_G}, \frac{z}{\sqrt{2}\sigma_G}\right)\right] * \bar{I}_l \tag{4.6}$$

According to (4.6), $R_2^{\theta,\phi}$ is calculated by convolving $\bar{I}_l$ first with a Gaussian kernel with standard deviation $\sigma_G = 3$ to smooth the structure. Then, the result is filtered by $H_2^{\theta,\phi}$, the Hilbert transform of $G_2^{\theta,\phi}$ (defined below) [100], in order to map the alignment degree of the vessel boundaries with the direction made by the spherical coordinate pair $(\theta, \phi)$ for each edge as shown in Figure 4.7(a). The term $G_2^{\theta,\phi} = \sin(\theta)[G_2^x \cos(\phi) + G_2^y \sin(\phi)\,] + G_2^z \cos(\theta)$ refers to the second order directional derivative of a 3-D Gaussian kernel $G(x, y, z) = e^{-(x^2+y^2+z^2)}$ where

$$\begin{aligned} G_2^x &= \frac{\partial^2 G}{\partial x^2} = (-2 + 4x^2) \times G(x, y, z), \\ G_2^y &= \frac{\partial^2 G}{\partial y^2} = (-2 + 4y^2) \times G(x, y, z), \\ G_2^z &= \frac{\partial^2 G}{\partial z^2} = (-2 + 4z^2) \times G(x, y, z). \end{aligned} \tag{4.7}$$

Finally, $\alpha_{A,l}$ is normalized by the edge length $d_l$ for coherency between different edges. Figure 4.7(b) shows three edges with different orientations with respect to the vasculature

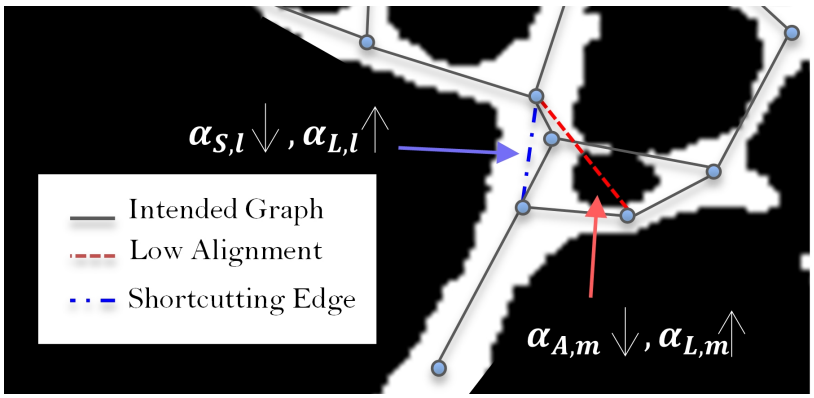


Figure 4.6: The motivation of alignment and skeletonness terms is shown as prevention of red and blue dashed lines cases that do not best match the microvasculature centerline. These edges are shown on a 2-D binarized frame with the intended graph overlaid by solid gray lines. Although $\alpha_{L,l}$ and $\alpha_{L,m}$ are rather large (majority of edges being located on the foreground), low skeletonness, small $\alpha_{S,l}$, of the blue line and low alignment with the local structure, small $\alpha_{A,m}$, of the red line make them undesirable results.

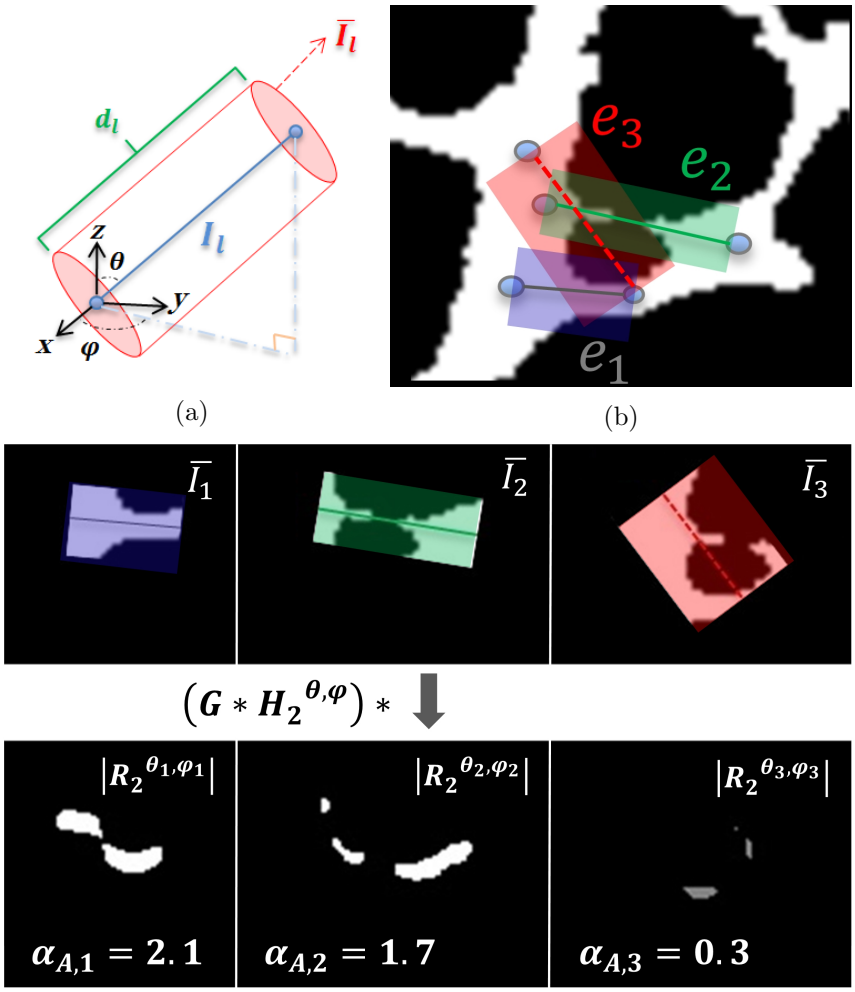


Figure 4.7: (a) Spherical coordinates $\theta$ and $\phi$ of edge $e_l$ along with other terms used for the directional filtering concept are shown in a Cartesian system, (b) An example consisting three different scenarios of the edge layouts on a vascular structure is provided. The utilities of $e_1$ (which clearly passes through a vessel) and $e_2$ (which is well aligned with the local direction of vasculature) are both higher than that of $e_3$ (which is poorly aligned with the vasculature and passes through a good deal of the background), (c) Three ROIs of the edges (top) and the absolute value of the directionally filtered ROIs and their alignment term, $\alpha_{A,l}$, with respect to each edge's direction (bottom). The edge $e_3$ that is not aligned with the vasculature in its ROI has the smallest alignment value.

in a 2-D demonstration. The first edge $e_1$ is located on a solid vascular branch. The second edge $e_2$ represents a broken vessel. The last edge, $e_3$, is an incorrect edge unaligned with the structure in its vicinity. Figure 4.7(c) provides visual understanding of how $\alpha_{A,l}$ contributes

to the graph model extraction by emphasizing the first two examples and penalizing the last case. The ROIs for the three scenarios are shown in the top section of the Figure 4.7(c). The absolute values of the directionally filtered ROIs with respect to each edge's direction are plotted and the computed $\alpha_{A,l}$s are shown in the bottom part of this figure. The $\alpha_{A,l}$s are larger in area and brighter in intensity for $e_1$ and $e_2$ that are aligned with the vascular structure. The result for the $e_3$ is smaller with lower intensity in comparison to the other edges.

The last component of the edge-based utility function is $\alpha_{S,l}$. The microvasculature network has a rather high spatial density (compactness) so that it may happen that a prospective edge "shortcuts" a path made by two or more other edges as shown by the blue line in Figure 4.6. These types of edges have relatively large $\alpha_{L,l}$ and $\alpha_{A,l}$ that happens to increase their utility and produce spurious and false edges in the resulted graph. The term $\alpha_{S,l}$ defined below penalizes such scenarios

$$\alpha_{S,l} = - \sum_{k=1,\ldots,n_{CP} \notin C_l} \langle I_l * G\left(\frac{x}{\sqrt{2}\sigma_S}, \frac{y}{\sqrt{2}\sigma_S}, \frac{z}{\sqrt{2}\sigma_S}\right), P_k * G(x,y,z) \rangle \tag{4.8}$$

where $C_l$ is the set of two end nodes of the $l^{th}$ edge, $\rho$ is the nominal vessel radius, $\sigma_S = \frac{\rho}{3}$, $P_k$ is the $k^{th}$ CP, and $G$ is the Gaussian function defined in the $\alpha_{A,l}$ formulation. By convolving nodes with a Gaussian kernel, equation 4.8 effectively decreases the utility of an edge when either (a) the number of nodes around that edge increases from zero or (b) the distance of other nodes to the edge decreases to less than the vessel radius. In Figure 4.8(a), two correct edges with no node in their Gaussian neighborhood are shown. Effect of close nodes to a shortcutting edge's utility function is schematically shown in Figure 4.8(b). The standard deviation of Gaussian kernel convolved with the edge is selected as one third of the vessel radius so that farther nodes have negligible effect on the inner product.

## 4.3 Graph Interpolation: A split and merge technique

Binary integer programs, which are known to be NP-hard, are a type of linear programming problems constrained to binary (0 or 1) unknown variables [101]. Most BIP problems have a finite number of feasible solutions, however this number can grow exponentially with the number of decision variables [45]. Here, the "branch and bound" approach described in Chapter 2 is used to find a solution of the BIP. While in principle one could formulate and solve the graph construction BIP for an entire data set, such an approach is challenging for two reasons. First, a universal and non-adaptive selection of parameters for the entire

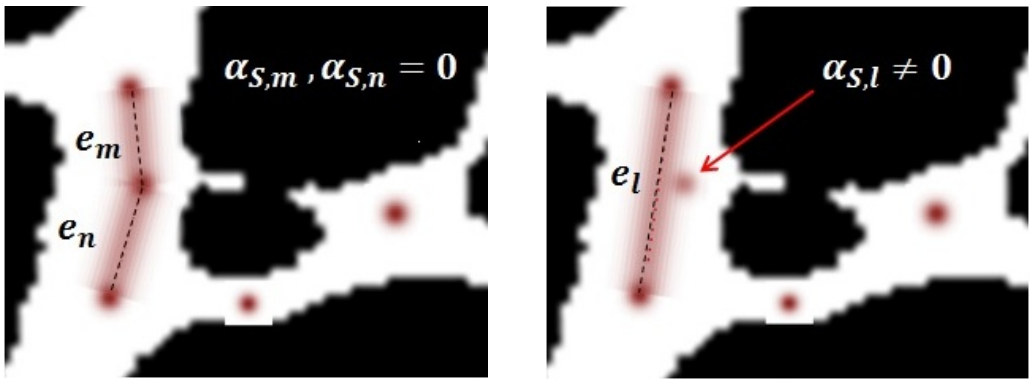


(a) Correct connections (b) Shortcutting connection

Figure 4.8: (a) A couple of correct edges with no node in their Gaussian induced neighborhood. (b) The effect of close nodes to a shortcutting edge's utility function as the inner product of the node's and edge's Gaussian convolution. The standard deviation of Gaussian kernel is selected such that the induced neighborhood is limited to the corresponding vessel and farther nodes have negligible effect on the shortcutting degree.

data set results in reduction of precision in the final graph as the structure shows variety of scales. Vessel radius for instance varies over the microvasculature by up to a factor of two as it is apparent from Figure 4.10. Second, BIPs are of exponential computational complexity thus run-time increases rapidly with growing CP collection. To compensate for these issues we consider an alternate idea in which data is divided into non-overlapping yet exhaustive partitions, then BIP is solved independently for each block. The resulting graphs are then "stitched" together using the approach described in the Algorithm 2.

Formally, a bipartite matching method [52, 67] is used to connect boundary points (defined in Section 4.1.4) across neighboring block faces. We start by constructing a matrix of costs associated with all possible node pairings between two faces and then use the Hungarian matching algorithm [67] to determine the matching with the lowest cost. Weights of this problem are defined as Euclidean distances between nodes when two sub-images are put side-by-side on the side of interest. Thus nodes with the smallest distance from each other will be matched. This process is exemplified in Figure 4.9. In this figure, matched points are connected with dashed lines where each set of the boundary nodes are indicated by green dashed boxes. This approach allows for unmatched node cases as shown by the middle node in the right hand side of Figure 4.9(a). After finding all the matching pairs, we replace them with a single new node located at midway between the two points in the interpolated graph as shown in Figure 4.9(b) and update the edge set of the interpolated graph to reflect the new nodes' connections.

**Algorithm 2** Graph Interpolation

**Inputs:** Binary image $I_B$
**Initialization:**
$\{B_i\}_{i=1,\dots,n} \leftarrow$ Non-overlapping and homogenous divisions of $I_B$
$g_i \leftarrow$ BIP obtained GGM of $B_i, i = 1, \dots, n$
$\{r_{i,j}\}_{j=1,\dots,n_{r_i}} \leftarrow$ Boundary points of $B_i, i = 1, \dots, n$
$G_T \leftarrow \cup_{i=1}^{n} g_i$
$I \leftarrow 1$
**for** $i = 1 : n$ **do**
    **for** $j = i + 1 : n$ **do**
        If $B_i$ and $B_j$ are neighbor:
        $C_{i,j}(k, l) \leftarrow \|r_{i,k} - r_{j,l}\|$, $k = 1, \dots, n_{r_i}$ and $l = 1, \dots, n_{r_j}$
        New nodes $\leftarrow$ Bipartite matching of boundary points given $C_{i,j}$.
        If facing a longside-bisected vessel: Do the orientation selective matching.
        **Update**: $G_T$
    **end**
**end**
**Output:** Total graph $G_T$

For the situations in which a vessel is bisected along its length at a block boundary (highlighted by a red shadowed region in Figure 4.9(a)), graph interpolation cannot be accomplished as there is no single boundary point associated with each sides' structures. This vessel layout related issue is overcome with an orientation selective matching approach.

The orientation selective matching method is comprised of a secondary matching in the direction orthogonal to the current matching direction. For achieving this aim, we start with processing the non-circular cross sectional areas identified with the approach mentioned in Section 4.1.4 to find the midpoint heights. We first stitch and then divide the two blocks of interest at the height level orthogonal to the vessel direction. At this point, updated boundary and CPs are detected for both of the new blocks and their connectivity is found via solving disjoint BIPs in new partitions. Finally, graph interpolation is used to match the new blocks. Node and edge sets will also be updated accordingly in the final graph. The overall graph interpolation process is demonstrated in Figures 4.9(c-d) where the final solid graph is shown in Figure 4.9(e). This proposed graph interpolation approach refines connections as well by introducing new waypoints and junctions at the secondary matching stage.

## 4.4 Experiments

The utility of the proposed graph-based network model identification algorithm is supported by the experimental results provided in this section. The performance of this approach is evaluated using synthetic and real data. Performance is quantified in terms of the network model detection precision and in the case of the synthetic data, robustness to noise. The

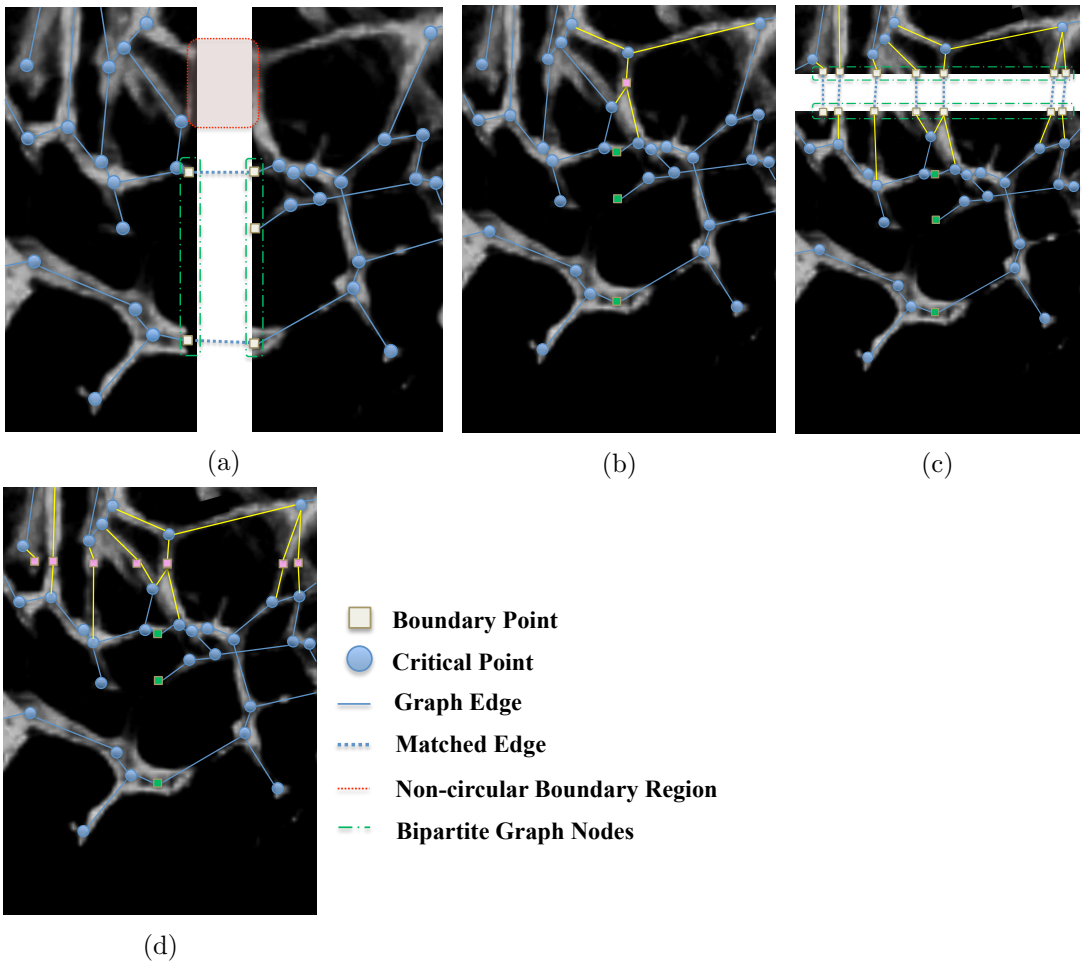


Figure 4.9: Graph interpolation between two pre-found graphs via matching boundary points of their shared side. (a) Dashed lines denote the matched points via bipartite matching where two parts are encircled by green dashed boxes. Non-circular vessel cuts are highlighted by a red box. (b) Secondary graph matching between the new boundary points is performed first by splitting the reference image horizontally at the height level of the non-circular region's mid-point. Then, new connections (yellow lines) are derived by performing BIP over the critical and boundary points of the new partitions. (c) New points are labeled as the final graph's nodes and newly found connections are included in its edge set. (d) Final graph-based model.

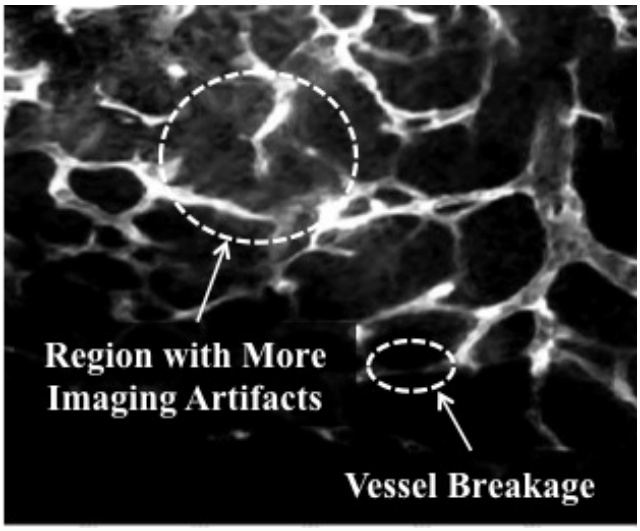


Figure 4.10: An example of false fractions in the structure caused by imaging imperfections and an area of more artifacts in MIP of a 3-D fluorescent microscopy image of microvasculature.

proposed method needs no manual interaction or parameter tuning except for the $\delta\rho$ and $\sigma_G$ parameters in the junction detection and directional filtering stages which are set as 2 and 3 respectively. The BIP has been solved by means of the built in MATLAB function "bintprog" that uses the branch and bound method for which the branch variables with the maximum integer infeasibility will be chosen for branching and the node variables with the lowest bound on the objective function will be selected in the search tree.

### 4.4.1 Pre-processing

The graph-based model extraction process is designed to be performed on a rough binary estimation of the vasculature. In Chapter 3, it was shown that the CREVER method yields rough segmentations of 3-D fluorescence microscopy images with high accuracy. To evaluate the geometrical graph-based modeling with the least dependency on segmentation accuracy, we also consider the level set method to binarize the raw images. However, due to the poor contrast and higher level of imaging artifacts of testing data *i.e.* fluorescence microscopy images, obtaining a reasonably accurate binarization exclusively through the level set algorithm is difficult. As illustrated in Figure 4.10, fluorescence microscopy images are challenging to process due to noise, non-uniform illumination, fluorescent background signal, and staining-related artifact contents [12, 16]. Larger vascular structures result in higher average intensity and consequently larger noise variance while smaller structures

suffer from lower photon counts and less signal content. These issues, which are shown in Figure 4.10, result in two challenges: (1) identifying the smaller structures along with their connectivity and (2) the recovery of larger vasculatures that tend to be surrounded by heavy noise.

To address the challenges discussed above, we make use of the local normalization method [102] as a means of initializing the level-set binarization step. The local normalization method transforms an input image, $I$, according to

$$I_{LN}(x,y,z) = \frac{I(x,y,z) - m_I(x,y,z)}{\sigma_I(x,y,z)} \tag{4.9}$$

where $I(x,y,z)$ is the original image intensity, $m_I(x,y,z)$ is the local average intensity, $\sigma_I(x,y,z)$ is the local standard deviation of intensity, and $I_{LN}(x,y,z)$ is the locally normalized intensity at point $(x,y,z)$. The quantities $m_I$ and $\sigma_I$ are computed in Gaussian windows with standard deviations $w_1$ and $w_2$ centered on $(x,y,z)$. The quantities $w_1$ and $w_2$ are selected such that the locally normalized image will have a bimodal intensity distribution that is ideal for a clustering-based thresholding such as Otsu's method [61]. Bimodality is maximized when the inter-class variance [61] between two modes is maximized. Thus, the optimal values of $w_1$ and $w_2$ are those that maximize the inter-class variance level. Through brute-force searching over different amounts of $w_1$ and $w_2$, it has been found that $w_1 = 15$ and $w_2 = 20$ produce the best results for the datasets of interest in this work. Otsu's thresholding of the normalized images is then used for initializing the level set method. Specifically, the level set function is initialized as the union of circles of radius one voxel centered on each of the thresholded voxels.

### 4.4.2 Validation metrics

The method's accuracy has been investigated by means of six metrics that quantitatively measure similarity of the identified network and ground truth. Both of the geometrical and topological specifications of a curvilinear structure are taken into account in definition of these metrics. The first four metrics of $C_{FPR}$, $C_{FNR}$, $G_{FPR}$, and $G_{FNR}$ come from the NetMets software package [103] where $C_{FPR}$ is Topological False Positive Rate defined as

$$C_{FPR} = \frac{Total\ number\ of\ falsely\ detected\ edges}{Total\ number\ of\ detected\ edges}. \tag{4.10}$$

The Topological False Negative Rate, $C_{FNR}$, is

$$C_{FNR} = \frac{Total\ number\ of\ missed\ edges}{Total\ number\ of\ edges\ in\ the\ ground\ truth}. \tag{4.11}$$

The $G_{FPR}$ and $G_{FNR}$ are geometrical peers of $C_{FPR}$ and $C_{FNR}$ where they capture lengths rather than numbers such that

$$G_{FPR} = \frac{Total\ length\ of\ falsely\ detected\ edges}{Total\ length\ of\ detected\ edges} \tag{4.12}$$

$$G_{FNR} = \frac{Total\ length\ of\ missed\ edges}{Total\ length\ of\ edges\ in\ the\ ground\ truth}. \tag{4.13}$$

Finally, $J_{FPR}$ and $J_{FNR}$ determine the junction detection precision as:

$$J_{FPR} = \frac{Total\ number\ of\ falsely\ detected\ junctions}{Total\ number\ of\ detected\ junctions} \tag{4.14}$$

$$J_{FNR} = \frac{Total\ number\ of\ missed\ junctions}{Total\ number\ of\ junctions\ in\ the\ ground\ truth} \tag{4.15}$$

### 4.4.3 Results: Synthetic Data

Synthetic images are formed by developing tubular interconnected networks from ground truth graphs inspired by the approaches discussed in [104, 105]. First, the ground truth graph is transformed into a binary 3-D volume, $S$, by means of the Bresenhamn's line algorithm [106]. Next, each of the lines in this binary image is dilated with a spherical structuring element with diameter of interest. The resulting image is then convolved with a 3-D Gaussian function with standard deviation of two in order to smooth the boundaries. From these "noise-free" images, simulated data are generated as $Poisson(\lambda_0 + \bar{N}_{q,q,q}(x,y,z))$. Here $\bar{N}_{q,q,q}(x,y,z)$ is the mean of $N_{q,q,q}(x,y,z)$ that is a $q-$by$-q-$by$-q$ neighborhood around the point $(x,y,z)$ in the noise-free image. Despite the lack of meaningful structures in dark regions of fluorescence microscopy images, voxels of these areas are slightly noisy [16]. We have modeled this background noise by adding an offset amount $\lambda_0$ to the mean value. Finally, the intensity range is scaled to span the range of seen in real data.

Figure 4.11(a) shows a synthetic image of size $400 \times 400 \times 200$ generated with $\lambda_0 = 10$ and $q = 10$. The same formula as (3.3) is used here to establish desired PSNR levels. This data is designed such that every step of the GGM identification process (CP detection, BIP, and graph interpolation) is challenged. For instance, vessel radius, branch density, and spatial density vary over different regions. The synthetic network includes more than one layer of structure to create higher 3-D depth and avoid a planar ground truth. The ground truth and extracted graph model are shown in Figures 4.11(c,d) for PSNR=5 dB. Performance metrics are presented in Table 4.1 for two pre-processing techniques. When all the error rates are relatively low, the method's performance with lower false negative

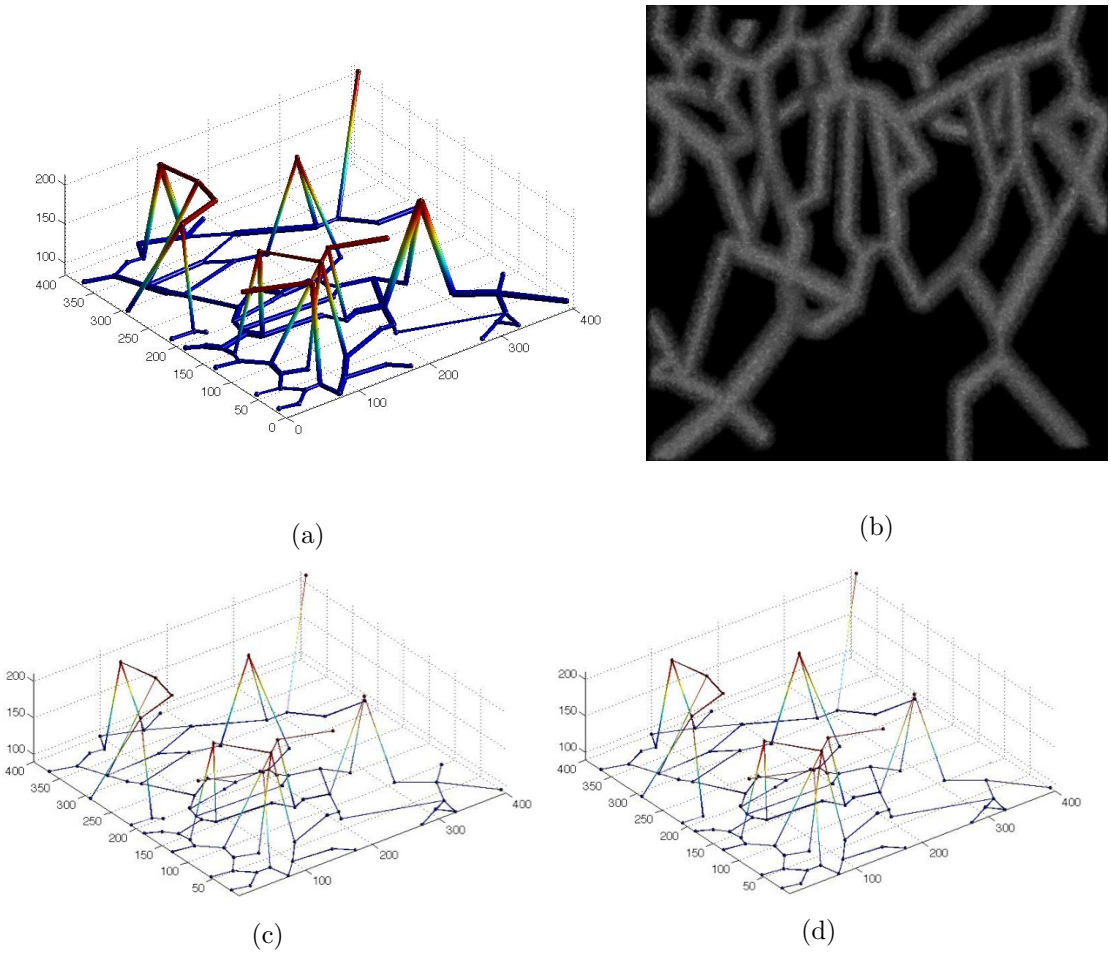


Figure 4.11: (a) Synthetic noiseless image, (b) MIP of synthetic noisy image with PSNR= 5 dB, (c) Ground truth, and (d) Obtained graph-based model synthetic noisy data.

Table 4.1: Performance metrics computed for synthetic image

| **Data set** | $J_{FPR}$ | $J_{FNR}$ | $C_{FPR}$ | $C_{FNR}$ | $G_{FPR}$ | $G_{FNR}$ |
|---|---|---|---|---|---|---|
| Complete (using CREVER method) | 0.082 | 0.013 | 0.044 | 0.043 | 0.062 | 0.038 |
| Complete (using level-set method) | 0.082 | 0.013 | 0.042 | 0.047 | 0.059 | 0.043 |
| 1 | 0.091 | 0.062 | 0.027 | 0.077 | 0.041 | 0.058 |
| 2 | 0.076 | 0.000 | 0.054 | 0.000 | 0.069 | 0.000 |
| 3 | 0.0105 | 0.000 | 0.100 | 0.100 | 0.104 | 0.092 |
| 4 | 0.000 | 0.000 | 0.000 | 0.000 | 0.000 | 0.000 |
| Complete (with graph interpolation) | 0.082 | 0.013 | 0.048 | 0.042 | 0.061 | 0.041 |

junction detections is seen to be outstanding. Higher false positive error rate in junction detection has given rise to the edge related error rates though they are still small and show the utility of the method. According to the results, the GGM identification algorithm performs at similar precision level for the CREVER and level-set methods that shows its robustness against reasonable structural deformations. The CREVER binarization leads to lower false negative rates where level-set method produces slightly less false alarms.

To test the graph interpolation performance, the network is decomposed into four sub-regions as shown in Figure 4.12(a) denoted by datasets 1-4. A common vessel has been considered between data sets 1 and 2 to allow for the use of orientation selective graph interpolation technique. Besides, radius and location of the vessels cross sections have been chosen slightly different at the two sides of the boundaries to test the node matching performance when there is an offset between the nodes to be matched. These differences are larger between the upper and lower images. The ground truth and complete identified graph model of the synthetic image binarized with the CREVER method are shown in Figures 4.12(b,c) in a 2-D view. Visual comparison of these two graphs proves an overall strong performance in capturing the synthetic network's model and interpolating the sub-graphs through matching the boundary points in spite of the implemented perturbations (missed branch in dataset 3 and slight differences in the CPs location). The performance metrics for this case are also presented in Table 4.1. These metrics are provided both separately for each of the datasets and for the complete simulated data. Comparison of these results with the "no interpolation" case suggests that the interpolation process improves the performance by reducing the false negative error rates.

For the purpose of noise analysis, noiseless synthetic image has been transformed into 100 volumes where every ten volumes are of the same PSNR level. The maximum intensity has been scaled with ten discrete values to the range of $(5, 255)$ such that PSNRs fall in the range of 2 to 15 dBs. Quantitative measures of the performance are calculated from derived graphs and are provided in Figures 4.13(a-f). For lower PSNR values, $J_{FNR}$ is increased noticeably indicating that more junctions are missed by the CP detection method. In such cases, small loops involving thick vessels may be closed as all the junctions around them are transformed into a single junction. Also, thicker branches get closer to each other such that junctions in their vicinity will be omitted during the spherical shell filtering. However, it is obvious that $J_{FPR}$ is less impacted by the higher noise levels.

Concerning the $C_{FPR}$ and $C_{FNR}$ metrics shown in Figures 4.13(c,d), a noise level dependency is more obvious. When an image is noisier, its enhanced binary version will be more dilated. The inflation of structures comes with smoother and less concave boundaries

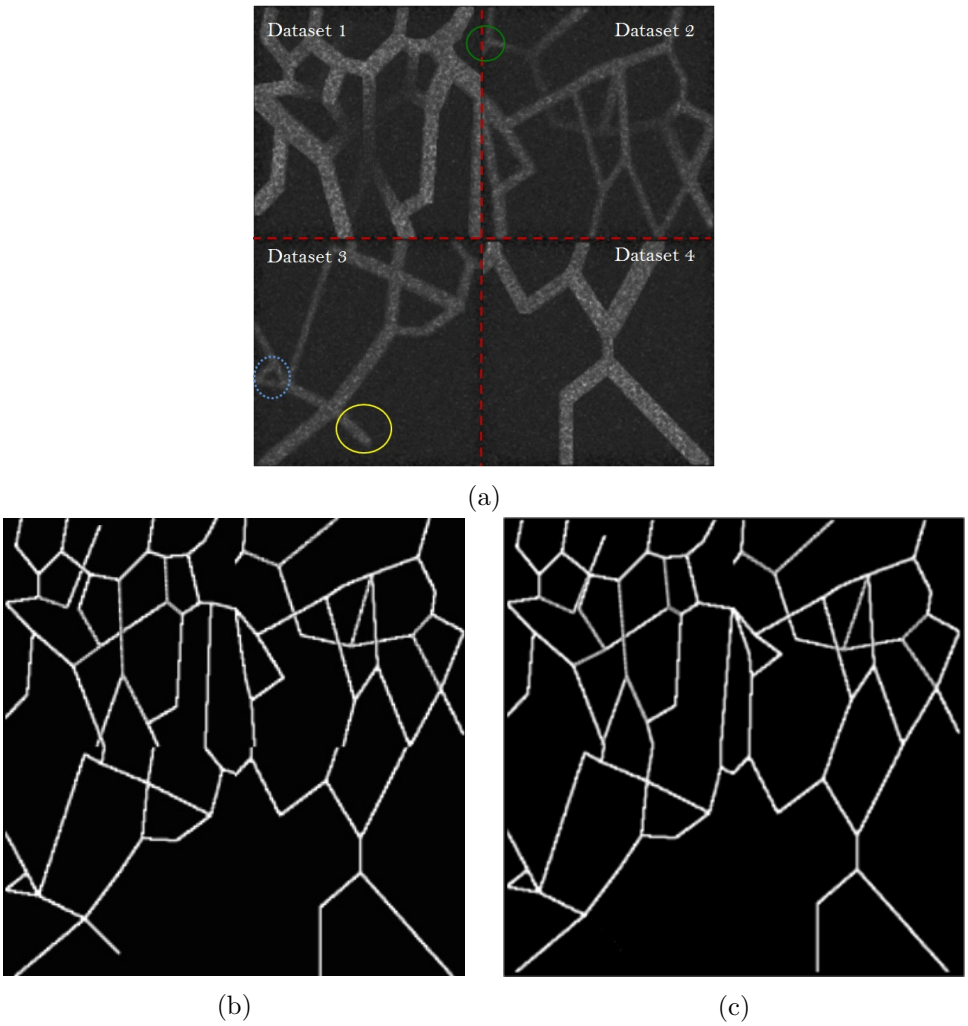


Figure 4.12: (a) Four sets of synthetic noisy images with PSNR= 5, (b) The ground truth, and (c) Overall graph-based model after graph interpolationa.

resulting in lower convexity degrees. Thus, a higher number of voxels cannot pass the convexity filtering step that leads to missing waypoints. An increase in missed waypoints yields a less complete graph and missed connections as a consequence.

Finally, the results for $G_{FPR}$ and $G_{FNR}$ are presented in Figures 4.13(e,f). In comparison to the $C_{FPR}$ values, $G_{FPR}$ is slightly larger especially for the lower PSNR values indicating a tendency for detection of longer edges by the method when there are missed junctions. From the analytical perspective, utilities increase for longer edges since their "skeletonness" increases as a result of missing more CPs. On the other hand, geometrical false negative rates have not deviated from the $C_{FNR}$ rates noticeably, and for a number of

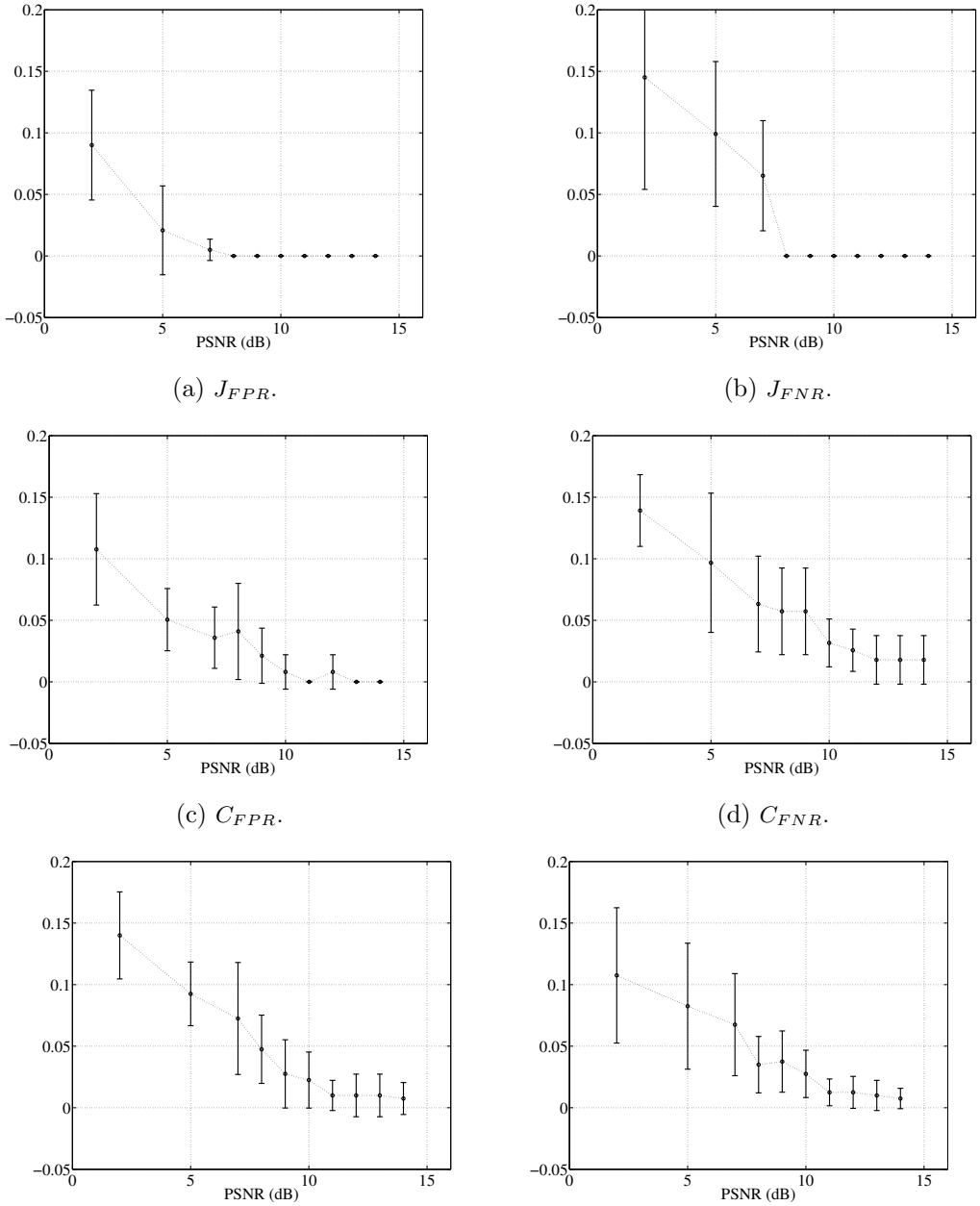


(a) $J_{FPR}$. (b) $J_{FNR}$.

(c) $C_{FPR}$. (d) $C_{FNR}$.

(e) $G_{FPR}$. (f) $G_{FNR}$.

Figure 4.13: Error rate bars of the (a) false positive junction detection, (b) false negative junction detection, (c) false positive topological connections, (d) false negative topological connections, (e) geometrical false positive , and (f) geometrical false negative error rates in terms of their mean and standard deviation computed over ten data volumes generated for each of the ten PSNR levels.

PSNRs, they are higher than the $C_{FNR}$. This observation complies with the above statement that longer edges come with greater utilities causing shorter edges be missed with higher rate.

### 4.4.4 Results: Real Data

Validation of the GGM identification algorithm has been completed by its application to four sets of 3-D vascular images gathered from murine nervous tissue. Three of these datasets are shown in Section 3.3.2. As mentioned earlier, these datasets are selected for their wide variety of structural and noise properties. The real images are binarized using two approaches of Section 4.4.1 and CREVER to assess the stability of the proposed method against the binarization quality alteration. To avoid redundancy, only the segmentations obtained from the method of Section 4.4.1 are shown in this section, as the binarizations produced by the CREVER algorithm are presented in Section 3.3.2. The GGMs acquired from the two types of binarized images are plotted for each data set and have been quantitatively evaluated using the six error metrics. Measured results are provided in Tables 4.2 and 4.3 for the level set segmentation and CREVER binarization respectively. In these tables, $N_{J-GT}$, $N_{J-D}$, $N_{E-GT}$, and $N_{E-GT}$ refer to the number of junctions and edges in the ground truth and detected graph model.

The efficiency of the graph interpolation technique is tested first for all the data sets (binarized with the CREVER method) and compared with the "no interpolation" results in Table 4.3. Then, a more detailed evaluation of this technique is conducted for data set 4 that has the most complete and dense microvascular network. Final results are provided in Table 4.4.

#### 4.4.4.1 Dataset 1: Non-homogenous structure and illumination with homogenous noise distribution

The first image which is a real 3-D fluorescence microscopy image of murine cortical microvasculature of size $200 \times 450 \times 50$ voxels is shown in Figure 4.14(a) where the MIP of its binary version with the extracted graph overlaid is shown in Figure 4.14(b). The graphs obtained from three uniform divisions of data are shown in Figure 4.14(c). These sub-graphs are interpolated into the black graph in Figure 4.14(d) where the ground truth is shown in red. The GGMs obtained from the two level set and CREVER binarizations are presented in 3-D view in Figures 4.14(e) and (f). According to these results, the proposed network

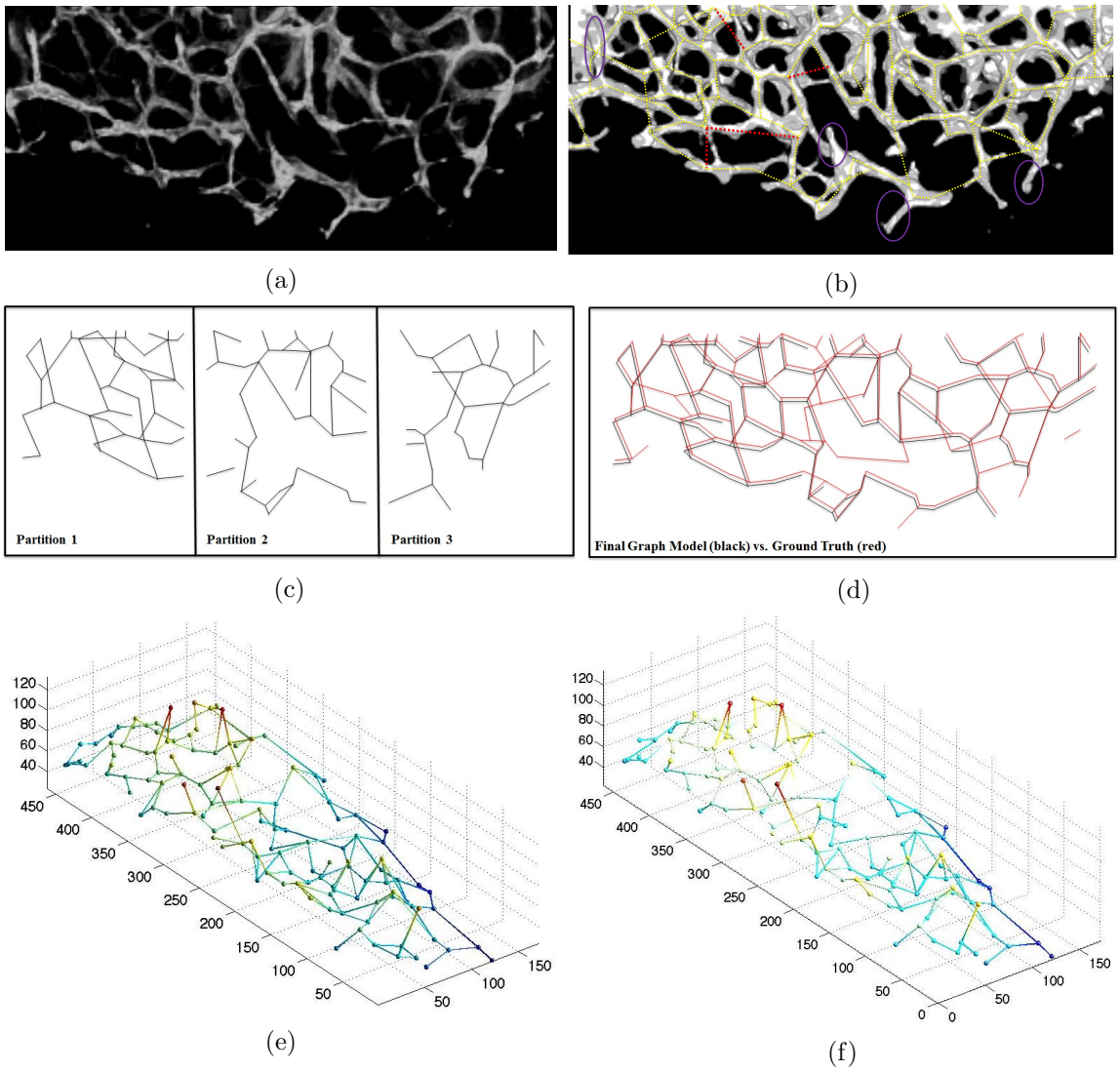


Figure 4.14: (a) Maximum intensity projection of dataset 1, a real 3-D fluorescence microscopy image of murine cortical microvasculature, (b) Enhanced binary image with illustration of the situations where graph extraction method fails to capture the correct structure. Purple ellipses identify vessels that are missed in the graph, and red edges are topologically correct but their locations are offset on one end. (c) Graphs obtained from three uniform divisions of data, (d) Interpolated graph in black vs. the ground truth in red, Extracted 3-D graph-based model obtained from the (e) level-set and (f) CREVER methods.

model identification algorithm has proved to be quite accurate in obtaining the microvasculature's skeletal model. While an overall satisfactory correspondence is observable between the raw data and the identified graph in Figure 4.14(b), two types of errors are highlighted.

Purple ellipses identify vessels that are missed in the graph because of being connected to an end point rather than a CP. Edges shown in red are topologically correct but their locations are offset on one end. These cases occur when one end node is missed in the CP detection process, yet due to the existence of another CP close to the missing node and the strength of the directional term in the BIP utility function, these edges are detected. Also, there are a few parts of the less visible and dimmer vessels along with the cut branches that have not been captured by the method.

#### 4.4.4.2 Dataset 2: Structures with high curvature

The second real data set is from the murine hippocampus and shown in Figure 4.15(a). This image is of size $600 \times 200 \times 24$ voxels. In spite of its larger size, the microvasculature has a simpler network layout with smaller vessel density relative to the other datasets considered here. This image also manifests a different structural shape; specifically, the manner in which it is "bent" along the left side of the image. In order to reproduce this curvature in the vasculature model, there has to be a higher ratio of waypoints (some of them are emphasized by squares in Figure 4.15(d)) to the total CPs testing the proposed technique from another perspective. Qualitative results for this dataset are presented in Figures 4.15(b-f). The binarized image is shown in Figure 4.15(b). This data is also partitioned into three regions and the extracted graphs are shown in Figure 4.15(c). The interpolated graph (in black) and ground truth (in red) are presented in Figure 4.15(d). The 3-D derived graphs are shown in Figures 4.15(e) and (f). Both types of results confirm that the method satisfactorily performs on the structure type of this data. Successful detection of CPs and waypoints in particular has resulted in a skeletal model quite close to the ground truth.

#### 4.4.4.3 Dataset 3: Structurally homogenous structure and non-homogenous noise distribution

The next data set relates to a more homogenous microvascular network in terms of vessel shape and size. However, the noise distribution differs markedly throughout the image as it is apparent from Figure 4.16(a). This image is of $500 \times 500 \times 45$ voxels size. The binary image is shown in Figure 4.16(b). The extracted sub-graphs from four uniform divisions of the data are demonstrated in Figure 4.16(c) where the ground truth in red and interpolated graph in black are presented in Figure 4.16(d). In spite of noisy voxels remained after the binarization, the graph-based model identification approach performs quite well on this challenging data set.

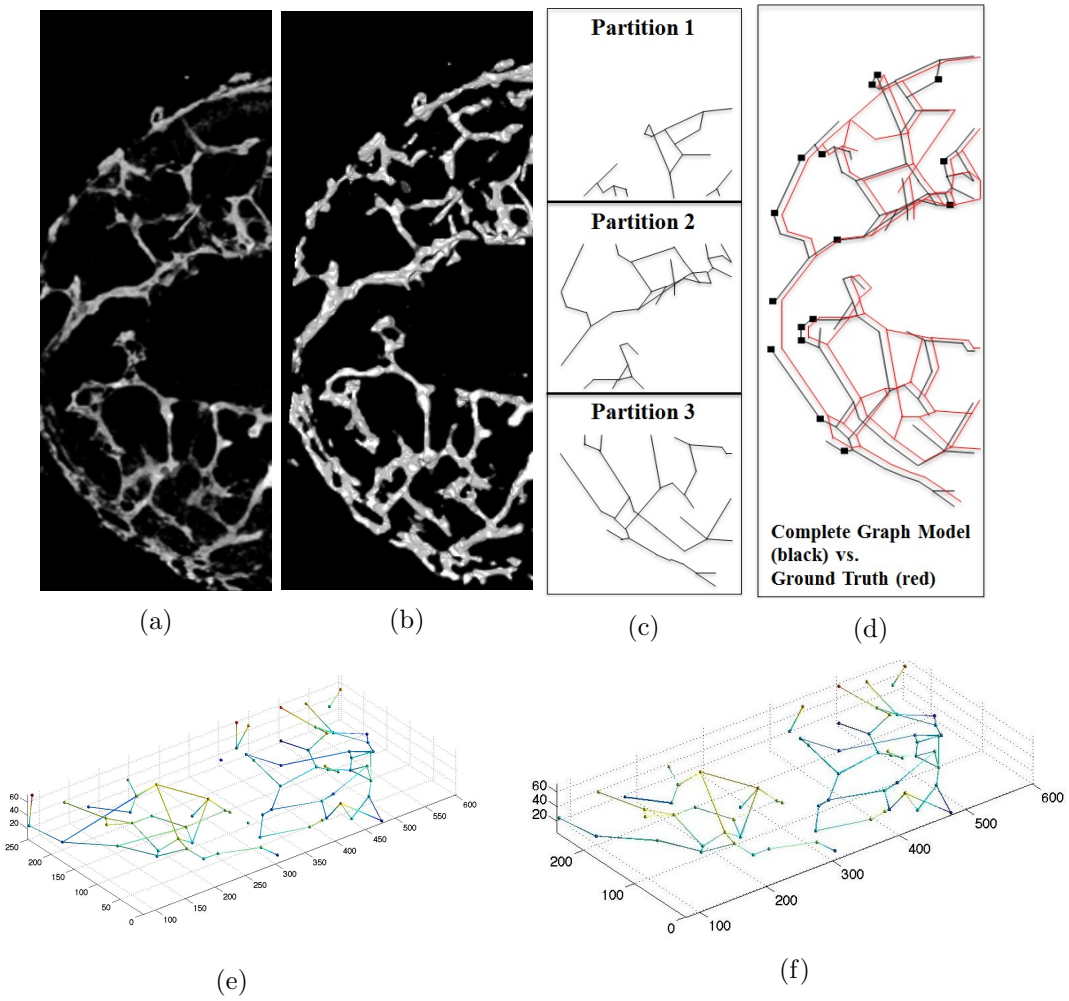


Figure 4.15: (a) Maximum intensity projection of dataset 2, a real 3-D fluorescence microscopy image of murine hippocampal microvasculature, (b) Maximum intensity projection of the binary image, (c) Graphs obtained from three uniform divisions of data, (d) Interpolated graph in black vs. the ground truth in red, Extracted 3-D graph-based model obtained from the (e) level-set and (f) CREVER methods.

#### 4.4.4.4 Dataset 4: Spatially dense structure and high variance noise

The last dataset, which is of $400 \times 400 \times 50$ voxels size, incorporates a very dense microvascular network with high level of noise content apparent in the original and binarized images shown in Figures 4.17(a,b). Due to the topological complexity of the network in this data set, we only focus on the quantitative analysis (Tables 4.2, 4.3, and 4.4) of the method where the graphs extracted from the upper left quarter of the full data set are shown in 3-D in Figures 4.17(c,d) for the level set and CREVER methods in this part of experiments.

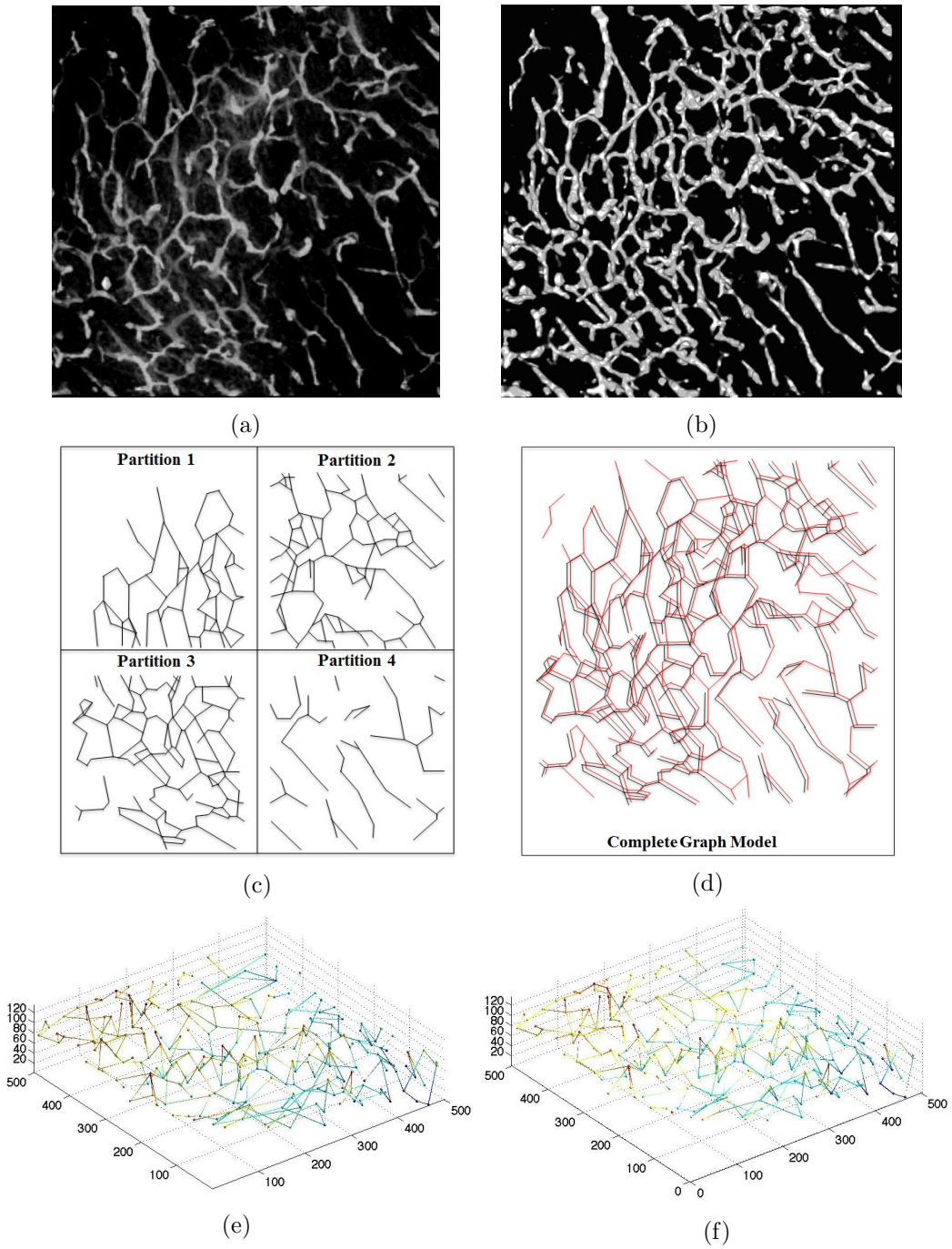


Figure 4.16: (a) Maximum intensity projection of dataset 3, a real 3-D fluorescence microscopy image of murine cortical microvasculature, (b) Maximum intensity projection of the binary image, (c) Graphs obtained from four uniform divisions of data, (d) Interpolated graph in black vs. the ground truth in red, Extracted 3-D graph-based model obtained from the (e) level-set and (f) CREVER methods.

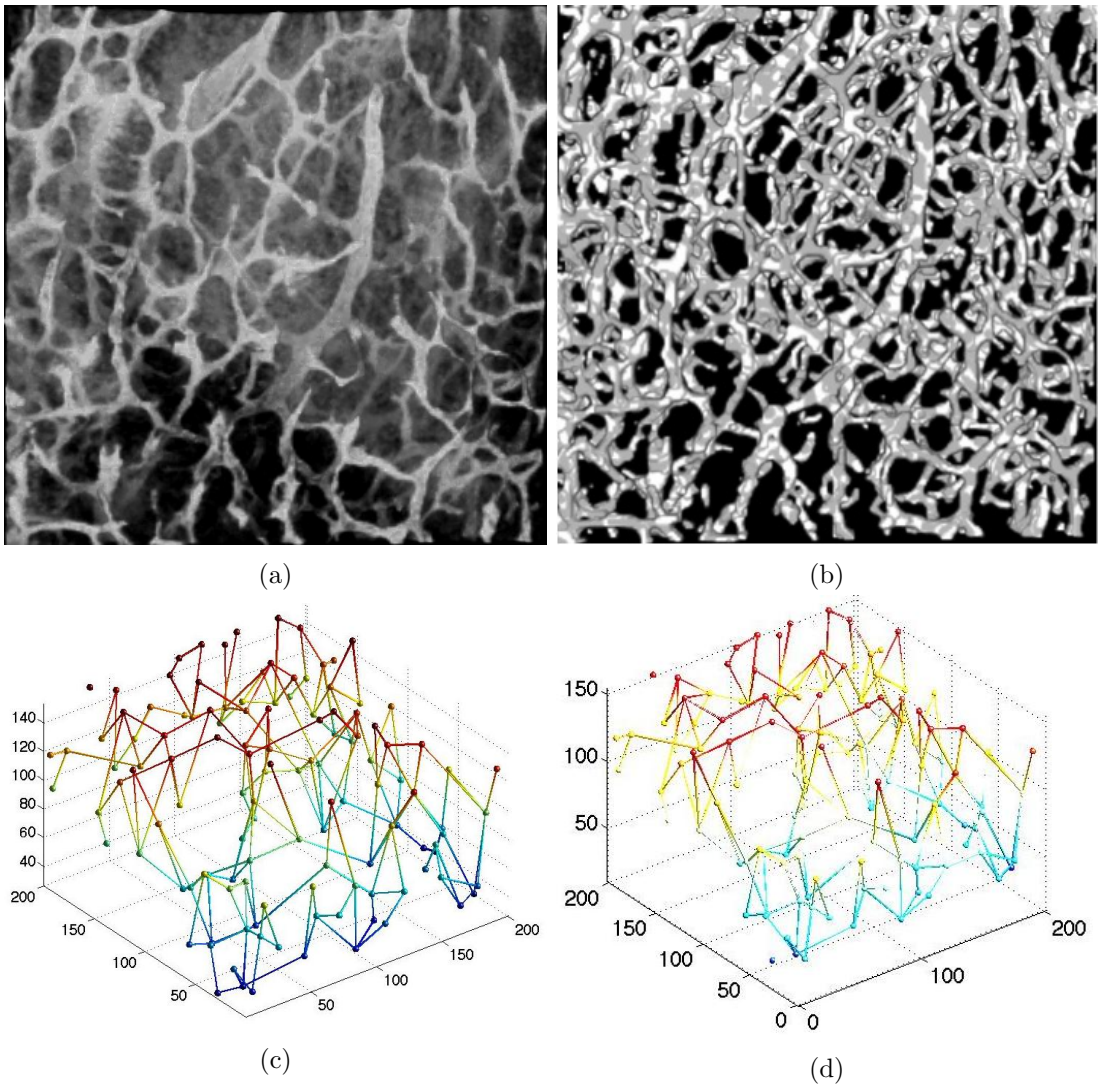


Figure 4.17: (a) MIP display of dataset 4, (b) MIP of its binarization, Extracted 3-D graph-based model of the upper left quarter of the image obtained from the (c) level-set and (d) CREVER methods.

Figures 4.18, 4.19, and 4.20 display the error rates for level-set (dashed lines with circular markers) and CREVER (solid lines with square markers) method vs. datasets. An overall comparison confirms that the CREVER method is superior in performance especially in the type II errors (FNR) for junction detection and type I error (FPR) in geometrical edge detection. CREVER yields higher error rates in $J_{FPR}$ only for datasets 1 and 2. This can be due to the higher ability of CREVER method in recovering the fainter or thiner structures prevalent in these datasets that consequently leads to higher rate of detections (true and false) in general.

Table 4.2: Performance metrics for real datasets pre-processed with the level set method.

| **Dataset** | $N_{J-GT}$ | $N_{J-D}$ | $J_{FPR}$ | $J_{FNR}$ | $N_{E-GT}$ | $N_{E-D}$ | $C_{FPR}$ | $C_{FNR}$ | $G_{FPR}$ | $G_{FNR}$ |
|---|---|---|---|---|---|---|---|---|---|---|
| 1 | 63 | 51 | 0.022 | 0.186 | 164 | 153 | 0.022 | 0.087 | 0.107 | 0.079 |
| 2 | 42 | 36 | 0.016 | 0.163 | 106 | 89 | 0.092 | 0.195 | 0.121 | 0.172 |
| 3 | 176 | 167 | 0.016 | 0.167 | 431 | 429 | 0.058 | 0.091 | 0.084 | 0.061 |
| 4 | 987 | 874 | 0.009 | 0.132 | 2804 | 2567 | 0.053 | 0.126 | 0.146 | 0.094 |
| Average | 317 | 282 | 0.036 | 0.162 | 876 | 809 | 0.056 | 0.125 | 0.114 | 0.102 |

Table 4.3: Performance metrics for real datasets pre-processed with the CREVER method with/without interpolation. The results for dataset 4 are obtained from the non-interpolated sub-graph of the upper left quarter.

| **Dataset** | $N_{J-GT}$ | $N_{J-D}$ | $J_{FPR}$ | $J_{FNR}$ | $N_{E-GT}$ | $N_{E-D}$ | $C_{FPR}$ | $C_{FNR}$ | $G_{FPR}$ | $G_{FNR}$ |
|---|---|---|---|---|---|---|---|---|---|---|
| 1 | 63 | 53 | 0.038 | 0.190 | 164 | 146/144 | 0.021/0.025 | 0.128/0.128 | 0.089/0.094 | 0.107/0.107 |
| 2 | 42 | 36 | 0.027 | 0.119 | 106 | 95/88 | 0.074/0.078 | 0.169/0.175 | 0.044/ 0.059 | 0.134/ 0.152 |
| 3 | 176 | 155 | 0.015 | 0.131 | 431 | 398/367 | 0.013/0.010 | 0.065/0.072 | 0.025/0.023 | 0.041/0.049 |
| 4 | 987 | 905 | 0.013 | 0.094 | 2804 | 2591 | 0.028 | 0.126 | 0.069 | 0.118 |
| Average | 317 | 287 | 0.023 | 0.134 | 876 | 807/ 200 | 0.034/0.038 | 0.102/0.125 | 0.056/ 0.059 | 0.100/0.103 |

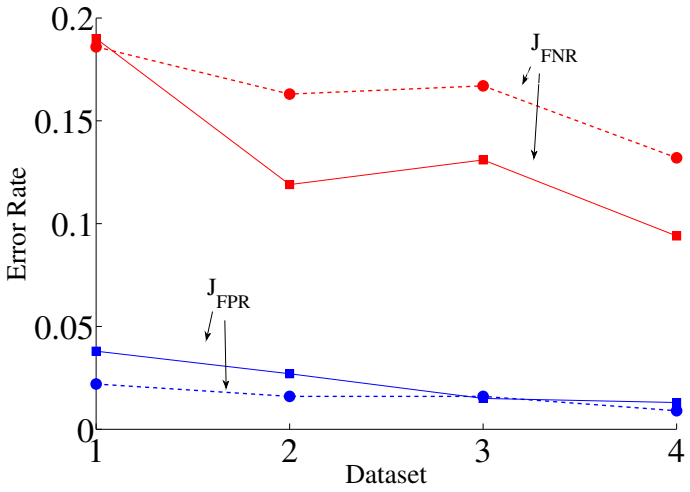


Figure 4.18: The junction detection error rates for the level-set (dashed lines with circular markers) and CREVER (solid lines with square markers) binarizations.

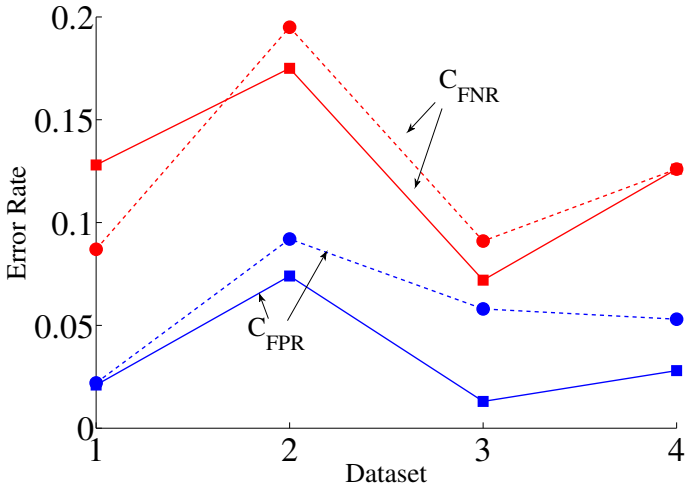


Figure 4.19: The topological edge detection error rates for the level-set (dashed lines with circular markers) and CREVER (solid lines with square markers) binarizations.

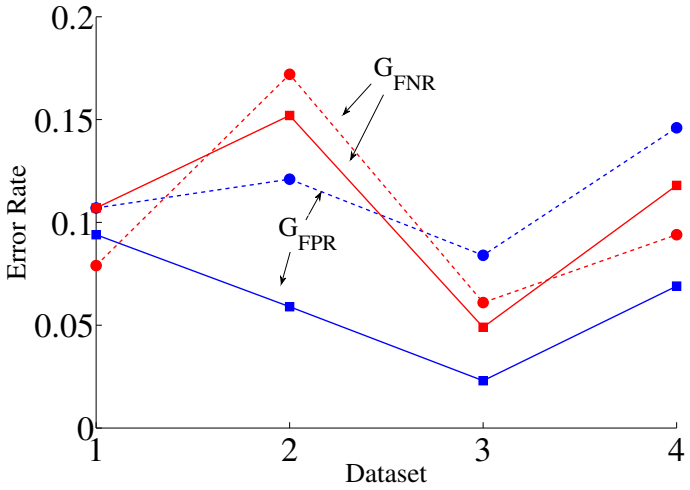


Figure 4.20: The geometrical edge detection error rates for the level-set (dashed lines with circular markers) and CREVER (solid lines with square markers) binarizations.

### 4.4.5 Divide and conquer procedure validation

The performance of the GGM identification method in conjunction with the graph interpolation improves in two main categories: speed and accuracy. The correlation of the partitions size and performance is investigated by running the algorithm on dataset 4 as it is divided into 2-by-2, 4-by-4, and 8-by-8 grids of non-overlapping and similar sized sections in the $x-y$ plane. Run time and performance metrics are measured for each case, averaged

Table 4.4: Effect of "split and merge" technique on the speed and error rates (extra computing times are referenced to the 8-by-8 layouts run time).

| Grid size | Run time (second) | Average number of variables, $n_E$, in each block | $J_{FPR}$ | $J_{FNR}$ | $C_{FPR}$ | $C_{FNR}$ | $G_{FPR}$ | $G_{FNR}$ |
|---|---|---|---|---|---|---|---|---|
| $2 \times 2$ | 22160 | 48828 | 0.013 | 0.094 | 0.088 | 0.095 | 0.154 | 0.069 |
| $4 \times 4$ | 3008 | 3321 | 0.013 | 0.094 | 0.062 | 0.098 | 0.111 | 0.072 |
| $8 \times 8$ | 704 | 300 | 0.013 | 0.094 | 0.028 | 0.102 | 0.069 | 0.118 |

over the same sized partitions, and presented in Table 4.4. These results demonstrate that operation time decreases dramatically as a result of the divide and conquer approach. The runtime from 8-by-8 to 4-by-4 grid patterns increases more than 4 times and from 4-by-4 to 2-by-2 grid the increase is about 7.4 times. One important factor that has to be taken into account for the divide and conquer application is density of the structure to be analyzed. If a sample image does not show a complicated and dense pattern such as is the case with dataset 2, dividing it into greater number of partitions appears to result in identifying false structures in each of the partitions which may actually decrease somewhat the overall accuracy (return to Table 4.3). Confirming this fact is the increase of false negative rate of the edges by dividing the image into smaller blocks. Based on the results given in Tables 4.3 and 4.4, the divide and conquer process does not affect the junction detection performance. On the other hand, the false positive rate of edge detection increases for the larger block sizes.

### 4.4.6 Computational complexity

As noted in the previous subsection, large BIPs can be challenging to solve. Here we explore the computational complexity and scalability of the proposed method empirically via testing the run times as a function of problem size. We take the full dataset 4 and consider "uniform", "horizontal", and "vertical" tessellations at three scales the coarsest of which is illustrated in Figure 4.21 and is comprised of four blocks for each tessellation. At the mid-scale, we have three sets of 16 blocks while the finest decomposition is into three sets of 64 blocks. Note that no division is performed in the third dimension since the dimensionality is quite low. All calculations were carried out on a PC platform with 2.53 GHz CPU, 6.00 GB RAM, and 64 bit OS running Matlab.

For the proposed algorithm, there are two components that drive the computational

complexity: calculation of the utility function terms and the solution of the BIP. In Figure 4.22(a), the logarithm of the run time is plotted against the logarithm of the problems size for all 192+48+12=252 blocks considered. In Figure 4.22(b), the logarithm of the run times versus the raw problem sizes are displayed. The linear nature of the relations in these plots indicates that the complexity of the utility function terms is proportional to problem size while, interestingly, the BIP solution processing time appears to rise exponentially with the size of the problem, but in a manner that varies with the scale of decomposition. From these plots, we also see that the processing time for this implementation of the approach is dominated by the image processing operations required to compute the utility function as opposed to the solver for the BIP. Finally, Figure 4.22 suggests that an approach based on decomposing the full problem into smaller sub-problems and then combining the results may offer a more efficient means of addressing large scale problems.

### 4.4.7 Parameter sensitivity

Finally, we turn our attention to exploring the sensitivity of the processing results to the non-automatically determined parameters, $\delta_\rho$ and $\sigma_G$ (the spherical shell thickness and the Gaussian kernel's standard deviation used in directional filtering). The experiments are completed on each of the sub-images produced by $8 \times 8 \times 1$ partitioning of dataset 4, and error rates are averaged over all the sets. First, performance measures are provided in Table 4.5 for $\delta_\rho$ equal to 1, 2, and 3 given $\sigma_G = 3$. Based on these results, junction detection precision shows a trade-off between false positive and negative rates when $\delta_\rho$ deviates from 2. However, the topological error rates seem to be directly affected by junctions and consequently the same trade-off as in junction detection performance exists for edge identification process. The $G_{FPR}$ follows the same pattern as $C_{FPR}$ and is smallest at $\delta_\rho = 2$. Therefore,

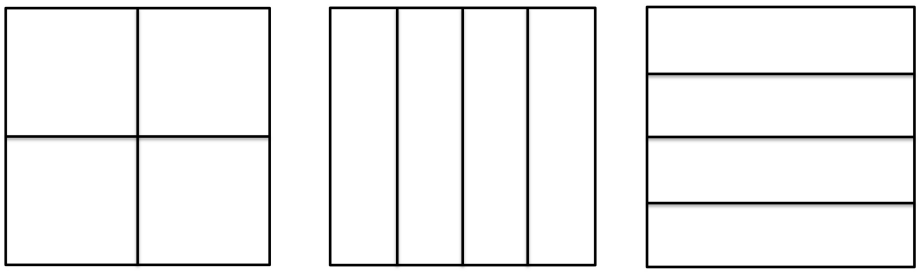

(a) (b) (c)

Figure 4.21: Three tessellations into four blocks using (a) "uniform," (b) "horizontal," and (c) "vertical" decompositions.

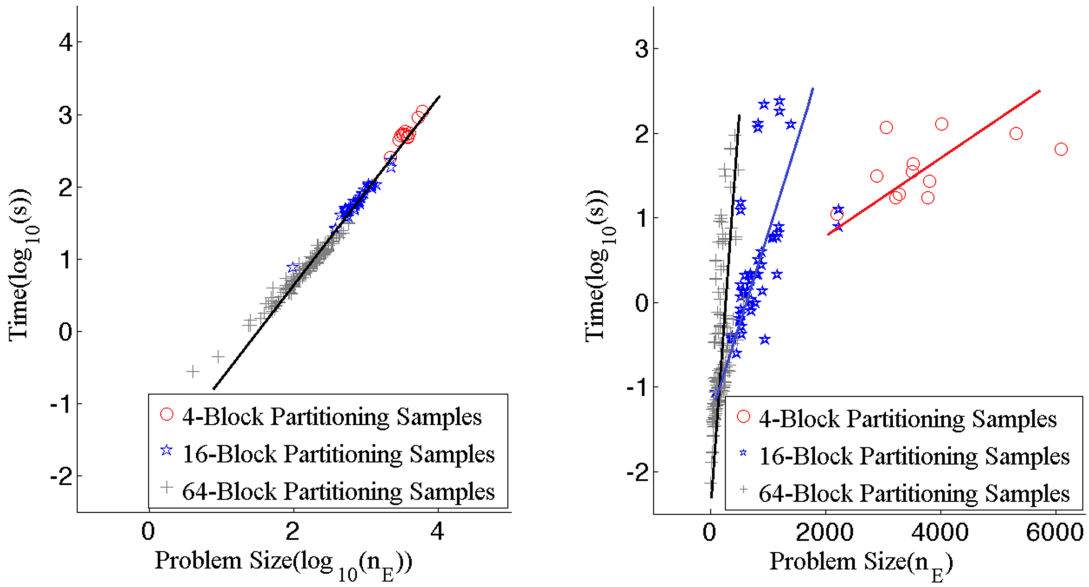


(a) Utility functions calculation

(b) BIP computation

Figure 4.22: Logarithm of the run time for all 252 blocks obtained from 4-block, 16-block, and 64-block partitioning and three different tessellations for (a) utility functions calculation and (b) BIP computation. A log-log plot is presented in (a) where the line indicates that complexity rises linearly with problem size for this calculation. A log-linear plot is provided in (b) where the linear structures indicate the exponential nature of the BIP complexity that depends on the scale at which the problem is decomposed.

Table 4.5: Performance measures with respect to $\delta_\rho$.

| $\delta_\rho$ | $J_{FPR}$ | $J_{FNR}$ | $C_{FPR}$ | $C_{FNR}$ | $G_{FPR}$ | $G_{FNR}$ |
|---|---|---|---|---|---|---|
| 1 | 0.123 | 0.060 | 0.271 | 0.069 | 0.198 | 0.115 |
| 2 | 0.019 | 0.088 | 0.033 | 0.094 | 0.079 | 0.111 |
| 3 | 0.014 | 0.105 | 0.039 | 0.156 | 0.075 | 0.254 |

to balance between the false positive and negative rates, $\delta_\rho$ has been set with 2.

Results produced by tuning the $\sigma_G$ with 2, 3, and 4 are provided in Table 4.6. Higher $\sigma_G$ leads to over-smoothing of the structure where smaller values of $\sigma_G$ does not change the image noticeably. Since, this parameter is used in forming the alignment term of the utility function, it only affects the edge-related error rates. Based on the results, a trade-off also exists for the topological and geometrical false positive and negative rates. In conclusion, the best error rates are obtained with $\delta_\rho = 2$ and $\sigma_G = 3$.

Table 4.6: Performance measures with respect to $\sigma_G$.

| $\sigma_G$ | $J_{FPR}$ | $J_{FNR}$ | $C_{FPR}$ | $C_{FNR}$ | $G_{FPR}$ | $G_{FNR}$ |
|---|---|---|---|---|---|---|
| 2 | 0.019 | 0.088 | 0.039 | 0.112 | 0.061 | 0.130 |
| 3 | 0.019 | 0.088 | 0.033 | 0.094 | 0.079 | 0.111 |
| 4 | 0.019 | 0.088 | 0.090 | 0.075 | 0.123 | 0.095 |

## 4.5 Discussion

Quantitative results in Tables 4.2 and 4.3 confirm the precision and sensitivity of the proposed algorithm challenged by different types of structures, noise levels, and pre-processing approaches. The proposed method proves to perform strongly in correct detection of junctions and edges given binarizations from the level-set and CREVER methods where the false positive rates for these statistics are around 0.036 and 0.056 for the former and 0.023 and 0.034 for the latter pre-processings. Regardless of the binarization quality, the method has performed the best in detecting the junctions for dataset 4. The highest false negative rate in junction detection is seen for dataset 1 which emanates from the fact that this data is characterized by many dim and broken vessels. Dataset 3 has the next highest rate of missed junctions due to the lack of good vascular connectivities and larger number of noisy voxels. These noisy voxels if located in the spherical shell will cause junctions to be missed due to the constraint on having one connected component in the larger sphere. In terms of edge detection, dataset 2 has the highest false positive error rate. This is caused first by the fact that a higher number of falsely detected nodes results in higher number of false edges. Second, an increase in the number of waypoints, seen in curvy structures, gives rise to the falsely detected edges. Since $G_{FPR}$ is higher than $C_{FPR}$ for all of the datasets, we can conclude that falsely detected edges are mainly of longer length than the average edge lengths. On the other hand, while the false negative rates do not change in correlation with the false positive rates, on an absolute scale, they are still relatively low and show the efficiency of the method in identification of the graph-based models. The $G_{FPR}$ is relatively lower for the CREVER results suggesting that it has been more efficient in retrieving vessels without causing spurious connections. All in all, the performance is slightly affected by the selected binarization technique and demonstrates better behavior for the CREVER method. However, the differences are negligible to the point that provided with a reasonable binarized version of any microvascular structure, the proposed method is able to yield an accurate GGM approximation of its skeleton.

Finally, sensitivity of the method is tested versus two non-automatically set parameters $\delta_\rho$ and $\sigma_G$. It has been shown that where $\delta_\rho$ as the spherical shell thickness primarily affects the junction detection process, $\sigma_G$ only affects the edge-based performance measures.

# Chapter 5

# Geometrical Graph-based Model Registration

The first step in analysis of GGMs is building a comparison means. For this purpose, these structure have to be registered to a template model to seek for their correspondences. We propose a novel and computationally efficient approach for GGM registration in this Chapter using the following notations:

Table 5.1: Notations used for the GGM registration.

| | |
|---|---|
| $\mathbb{R}^{N\times M}$ | Space of real matrices of size $N \times M$ |
| $\hat{\Pi}^{N\times N}$ | Space of permutation matrices of size $N \times N$ with unitary element at (1,1) |
| $\mathcal{E}^{N\times M}$ | Space of non-negative matrices of size $N \times M$ with rows that sum to one |
| $\mathcal{A}^{N\times M}$ | Space of assignment matrices of size $N \times M$ defined as binary matrices with rows that sum to one |
| $\|.\|_F$ | Ferobenius norm defined as $\|A\|_F = \sqrt{\sum_i \sum_j A_{ij}^2} = \sqrt{\text{tr}(A^T A)}$ |

## 5.1 Attributed graph generation

Given $m$ geometrical graph-based models, their attributed forms $G_i = (V_i, E_i, \phi_i, \zeta_i)$, $i = 1, 2, \ldots, m$ are generated as follows. The $G_i$ is characterized by a node set $V_i$ representing vascular junctions with cardinality $n_i = |V_i|$ and edge set $E_i \subset V_i \times V_i$ representing vessel branches that connect the junctions. The $\phi_i$ and $\zeta_i$ are vectors of node and edge attributes respectively.

To form $G_i$, waypoints and the chain of midway edges are first eliminated from the node

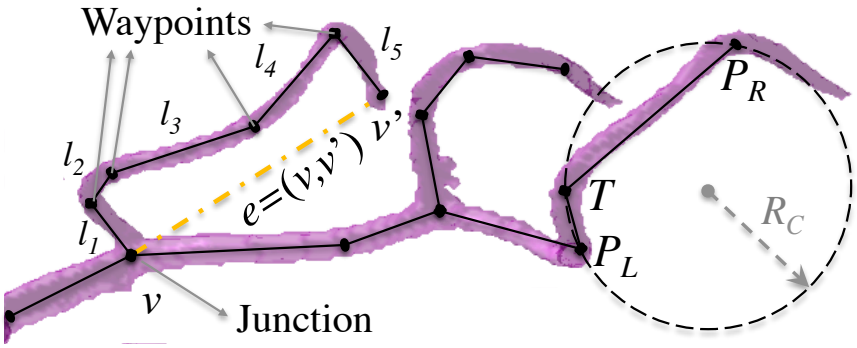


Figure 5.1: Part of a vessel along with its geometrical graph-based model (collection of piece-wise linear segments approximating skeleton) are presented. An abstract edge $e = (v, v')$ is shown with dashed yellow line between junction $v$ and terminal point $v'$. This edge replaces the segments located between $v$ and $v'$ during generation of attributed graph where waypoints will be omitted. Smoothed local curvature of a vessel at point $T$ can be estimated from its geometrical graph model as a function of $R_C(T)$ that is radius of the circumcircle of the triangle defined by $T$ and its neighboring waypoints $P_R$ and $P_L$.

and edge sets. Then, between two immediate neighbor junctions or between a junction and a terminal point (*e.x.* $v$ and $v'$ in Figure 5.1), an abstract edge ($e = (v, v')$) is placed that represents the vessel branch connecting those points.

Node attributes are determined by $\phi_i : V_i \rightarrow \mathbb{R}^{3\times1}$ that relates junctions location in 3-D space to their counterpart nodes in $V_i$ such that $\phi_i(v) = [x\ y\ z]^T, \forall i$. Subsequently, edge attributes are embedded in $\zeta_i : E_i \rightarrow \mathbb{R}^{2\times1}$ such that $\zeta_i(v_j, v_k)$ equals to the approximated length and smoothed curvature of the vessel connecting nodes $v_j$ and $v_k$ respectively. The first attribute of each abstract edge is an estimate of the vessel branch length. This value is defined to be summation of the length of all edges of the geometrical graph associated with the abstract edge; *e.g.*, in Figure 5.1, the length of $e = l_1 + l_2 + ... + l_5$. The second edge attribute is associated with the curvature of vessels. Local curvatures can be estimated at each waypoint from the change in the slope angle (angular difference between successive segments) of the lines [107]. Given the notations in Figure 5.1, curvature at waypoint $T$ is $C(T) = \frac{S}{R_C(T)}$ where $S = \text{sign}(\text{determinant}(\overrightarrow{TP_R}, \overrightarrow{TP_L}))$. The $R_C(T)$ is the radius of the circumcircle of the triangle made by $T$ and its neighboring waypoints $P_R$ and $P_L$:

$$R_C(T) = \frac{s_1\ s_2\ s_3}{\sqrt{(s_1+s_2+s_3)(s_1-s_2+s_3)(s_1+s_2-s_3)(-s_1+s_2+s_3)}} \tag{5.1}$$

where $s_1 = \|\overrightarrow{TP_R}\|$, $s_2 = \|\overrightarrow{TP_L}\|$, and $s_3 = \|\overrightarrow{P_RP_L}\|$. We define the smoothed curvature that is a measure of the vessels shape as the summation of the absolute value ($\|.\|_1$) of the $C$s calculated for all the waypoint along each edge.

The graphs of interest in this work are of the binary tree form. Therefore, non-leaf nodes have exactly three connections (a parent and two child nodes). Utilizing this specification, we convert graph matching from a quadratic assignment into a point correspondence problem by developing node features called *signatures* that simultaneously incorporate the geometrical and topological information of the graphs to be matched. A signature for the $i^{th}$ node in graph $k$ is defined as

$$\sigma_k(v_i) = \begin{bmatrix} \phi_k(v_i) & \phi_k(v_{i,1}) & \phi_k(v_{i,2}) & \phi_k(v_{i,3}) \\ \zeta_k(v_i, v_i) & \zeta_k(v_i, v_{i,1}) & \zeta_k(v_i, v_{i,2}) & \zeta_k(v_i, v_{i,3}) \end{bmatrix} \in \mathbb{R}^{5\times 4} \tag{5.2}$$

where $v_{i,1}, v_{i,2}$, and $v_{i,3}$ are the three connections of $v_i$. Since there is no loop (buckle) in these graphs, $\zeta_k(v_i, v_i) = 0, \forall i$. Then, correspondences are found based on node-to-node signature affinity. Where two nodes have similar signatures, it indicates that those nodes and their connections are located closely and the corresponding edges are also of alike shapes so they are the best matches. The correspondence procedure will be described in detail in Section 5.3.

## 5.2 Global alignment

Inspired by the Procrustes analysis [108], we establish a reference graph space in which the graphs to be matched are are embedded in a manner that basically normalizes for translation rotation and scaling. First, centers of gravity of graphs are placed on the origin so that $\sum_{j=1}^{n_i}(\phi(v_j)) = [0\,0\,0]^T, \forall i$. As we show in Section 5.5.5, nodes of higher levels (farther from Circle of Willis (CoW)) show larger variance in location or face higher chance of removal due to segmentation errors. Thus, we choose three junctions located on the CoW as anatomical landmarks for the balance of the alignment processing. These anatomical points that are marked by white circles in Figure 5.2 are the most homologous features among the cranial artery network samples. To achieve the scale invariance, we scale graphs such that their nodes that correspond to the crossed landmark in Figure 5.2 place at $(1, 0, 0)$. Finally, graphs are aligned by rotational transformations that project two other landmarks onto the $x - y$ plane.

## 5.3 Objective formulation

In this section, we formulate and solve the node correspondence problem based on the signature similarity maximization across any two graphs. Correspondences are modeled by

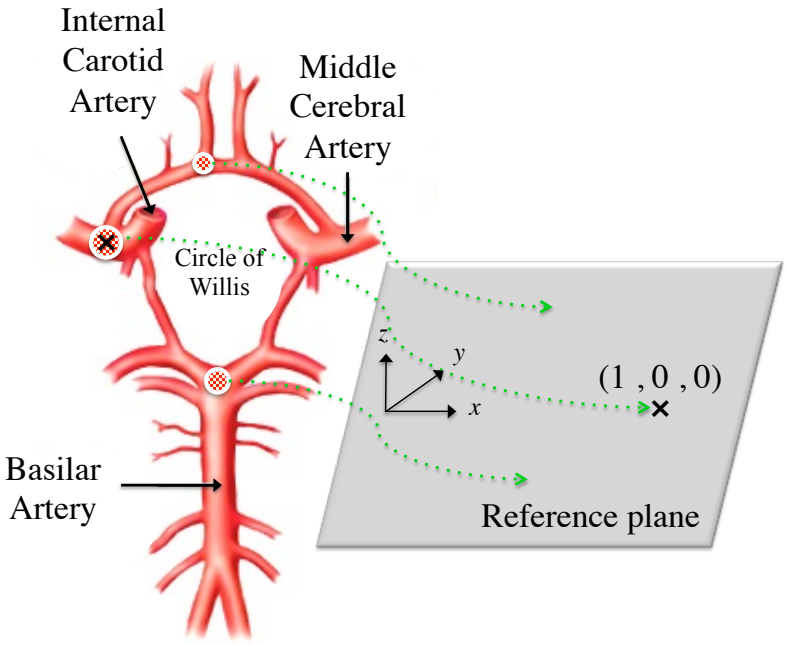


Figure 5.2: Three anatomical landmarks on the CoW used for alignment procedure are marked by white circles. The scale of graphs are normalized by mapping the node associated with the crossed junction to (1, 0, 0) in the Cartesian system. Graph poses are harmonized by rotations that map the other landmarks onto the $x-y$ plane.

binary indices $a_{ij} \in \{0,1\}, i = 1,\ldots,n_1, j = 1,\ldots,n_2$ where $a_{ij} = 1$ means that nodes $v_i \in V_1$ and $v_j \in V_2$ have the most similar signatures and are the best matches. The $a_{ij}$s form an assignment matrix $A \in \mathcal{A}^{n_1 \times n_2}$. By the sub-graph isomorphism problem definition, an assignment matrix can only take at most one non-zero element in each row or column, $\sum_{i=1}^{n_1} a_{ik} \leq 1, \forall k$ and $\sum_{j=1}^{n_2} a_{lj} \leq 1, \forall l$, to guarantee that every node of one graph is assigned to at most one node in the other graph [86].

Generally, connections of a node are labeled arbitrarily in its signature. Therefore, an optimal permutation of the three connections has to be estimated for achieving the most accurate node assignment. As shown in Figure 5.3 for instance, $\sigma_1(v_i)$ has to be multiplied by the given $B_{ij}$ such that $\sigma_1(v_i)B_{ij}$ will be minimally distant from $\sigma_2(v_j)$. Thus we need $4 \times 4$ permutation (orthogonal and doubly stochastic) matrices $B^{ij}, i = 1...,n_1, j = 1...,n_2$ for which always $B^{ij}(1,1) = 1$ (base nodes are compared with each other).

Given the above definitions and two globally aligned graphs $G_1$ and $G_2$, matching problem is defined as

$$A = \underset{A \in \mathcal{A}^{n_1 \times n_2}, B^{ij} \in \hat{\Pi}_4}{\arg\min} \sum_{i=1}^{n_1} \sum_{j=1}^{n_2} a_{ij} \|\sigma_2(v_j) - \sigma_1(v_i)B^{ij}\|_F - \lambda \|A\|_F \tag{5.3}$$

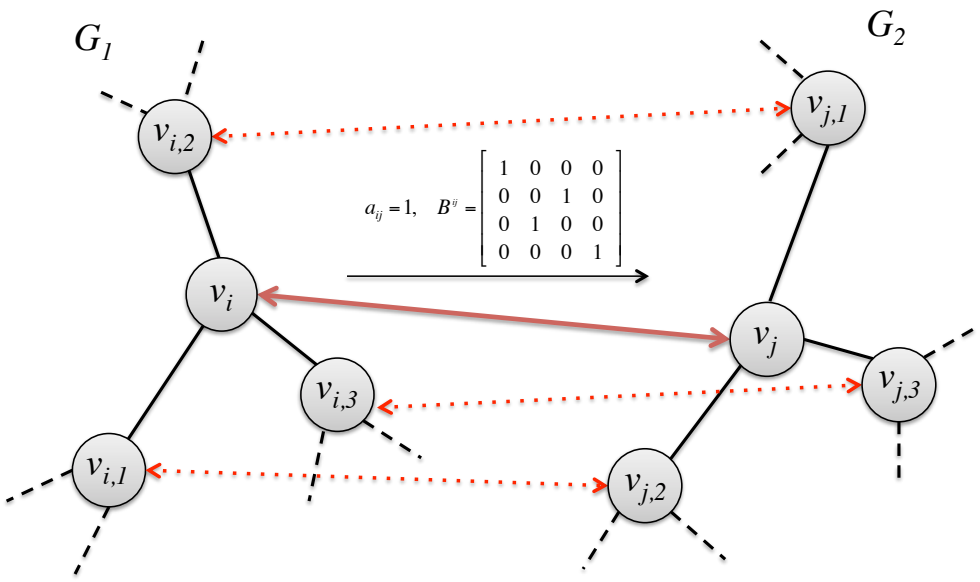


Figure 5.3: The shown $B^{ij}$ permutes $\{v_{i,1}, v_{i,2}, v_{i,3}\}$ so $\|\sigma_2(v_j) - B^{ij}\sigma_1(v_i)\|_F$ is optimally minimized.

where the regularization term penalizes correspondence of too distant nodes (distance tolerance) *i.e.* If the distance of two nodes surpasses $\lambda$, they will not be matched in spite of having the closest signatures. The $\lambda$ is manually set for this work considering the reasonable anatomical deviations.

## 5.4 Combinatorial optimization relaxation

In this section, we describe the essence of the algorithm that solves the combinatorial problem of (5.3). This problem calls for two interconnected linear assignment optimizations. The optimal assignment and permutation matrices are determined in an iterative manner where one is held fixed after convergence and then the other is found. At each iteration and through application of the graduated assignment technique [75] and [109], we relax the combinatorial matrices to be continuous. As described in Chapter 2, the graduated assignment algorithm is comprised of two fundamental elements: soft assign and deterministic annealing techniques [86]. Simply put, soft assign method relaxes binary matrices ($A$ and $B^{ij}$s here) to take continuous values in the $[0, 1]$ interval. This relaxation reduces the chance of trapping in local minima (a common challenge of combinatorial optimizations) by allowing partial/soft matches between points and smooth updates during the optimization process rather than jittering between 0 and 1. Figure 5.4 provides a visual description of

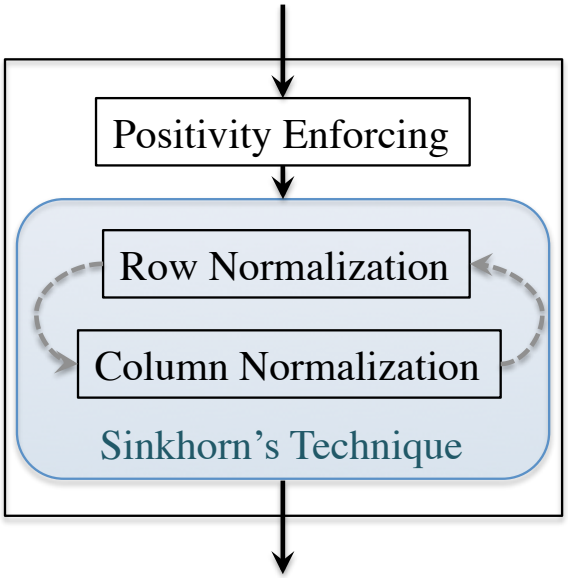


Figure 5.4: Soft assign method

the soft assign method. After enforcing positivity to the elements *e.x.* via exponentiation, the process continues subject to keeping matrices doubly stochastic (summation of elements in each row or column amounts to one). The "summation to one" constraint is guaranteed by iterative normalization of rows and columns [89]. Our problem of cranial vascular GGM registration allows for outliers (structural variety for inter-subject cases). Thus the assignment matrix may include rows or columns of all zero elements by definition. To satisfy the doubly stochasticity constraint for these scenarios, $A$ is modified by addition of a row and a column as explained in Chapter 2. A modified version of the two-way doubly stochastic constraint holds as

$$\sum_{i=1}^{n_1+1} a_{ik} = 1,\ k = 1, \ldots, n_2 \quad , \quad \sum_{j=1}^{n_2+1} a_{lj} = 1,\ l = 1, \ldots, n_1 \tag{5.4}$$

and is based on the Birkhoff theorem [110]: the set of doubly substochastic matrices is the convex hull of the set of permutation matrices of same size. In Figure 2.7, the convex hull of a sample of permutation matrices $P_i, i = 1 \ldots, 6$ is shown with a colorful hexagon area. Each point in this area is a convex combination of the $P_i$s and is a doubly stochastic matrix. Shades of colors correspond to different levels of matrix entropy, $-\sum_{i=1}^{n_1}\sum_{j=1}^{n_2} a_{ij}\log(a_{ij})$. Warmer colors in the center represent matrices of higher entropy with more randomly distributed (continuous) elements where binary matrices at the corners demonstrate the lowest

level of entropy. Therefore, enforcing a gradually reducing entropy level constraint, leads matrices to converge to any of the polytope's corners ($P_6$ here) *i.e.* permutation or binary doubly stochastic matrices in general. Combination of continuous relaxation and Birkhoff theorem transforms the combinatorial correspondence problem (5.3) into the following optimization formulations.

$$A = \underset{A \in \mathcal{E}^{n_1+1 \times n_2+1}}{\arg\min} \quad \sum_{i=1}^{n_1}\sum_{j=1}^{n_2}(a_{ij}\|\sigma_2(v_j) - \sigma_1(v_i)B^{ij}\|_F - \lambda a_{ij}^2) + \beta \sum_{i=1}^{n_1}\sum_{j=1}^{n_2} a_{ij}\log(a_{ij}) \tag{5.5}$$

Since $B^{ij}$s are permutation matrices of small size, they can be tractably found by running bipartite matching (with computational complexity of *e.x.* $\mathcal{O}(N^3)$ for Hungarian method) among all the signatures across two graphs. However, we can manage to reduce the computation time by use of the graduated assignment that is of $\mathcal{O}(N^2)$ complexity. Via this approach, the complexity can be even further reduced with selectively updating $B^{ij}$s only for the correspondences that are strengthening, $a_{ij}^I > a_{ij}^{I-1}$ where $I$ is the iteration count. The respective optimization form for such cases in the graduated assignment framework would be

$$\hat{B^{ij}} = \underset{\{B^{ij} \in \mathcal{E}^{4\times 4} | B_{11}^{ij}=1\}}{\arg\min} \quad \sum_{k=2}^{4}\sum_{l=2}^{4} B_{kl}^{ij}\|\phi(v_{j,k}) - \phi(v_{i,l})\|_F + \beta \sum_{k=2}^{4}\sum_{l=2}^{4} B_{kl}^{ij}\log(B_{kl}^{ij}). \tag{5.6}$$

Parameter $\beta$ that is the same for optimizations (5.5) and (5.6) controls the relaxation degree via tuning the entropy term's effect in optimizations (5.5) and (5.6). The smaller the $\beta$, the more bipolar the results will be. Thus, binary matrices are achieved by regularly reducing (annealing) $\beta$ [75] with annealing rate $\beta_r$. The optimal matrices obtained at each $\beta$ level, are used as initial values for the next stage that the $\beta$ is lowered. When $\beta$ reaches zero, matrix entries converge to either 0 or 1.

### 5.4.1 Graph registration algorithm

The overall matching algorithm is described step by step in this section where its pseudocode is provided in Algorithm 2. Based on the descriptions given in the previous part, this algorithm is essentially a dual update process embedded within an annealing scheme. Prior

to the start of process and at lines 1 and 2 of Algorithm 2, $a_{ij}$ and $B^{ij}$s are initialized as

$$B^{ij} = \begin{bmatrix} 1 & 0 & 0 & 0 \\ 0 & \frac{1}{3} & \frac{1}{3} & \frac{1}{3} \\ 0 & \frac{1}{3} & \frac{1}{3} & \frac{1}{3} \\ 0 & \frac{1}{3} & \frac{1}{3} & \frac{1}{3} \end{bmatrix} \; i = 1, \ldots, n_1, \; j = 1, \ldots, n_2 \quad \text{and} \quad a_{ij} = 0. \tag{5.7}$$

The main loop that is associated with annealing parameter adjustment incorporates the following operations.

Weight coefficients for the correspondence matrix entries are first calculated as

$$Q_{ij}^A = \|\sigma_2(v_j) - \sigma_1(v_i)B^{ij}\|_F - \lambda. \tag{5.8}$$

Then, positivity is enforced on $a_{ij}$s with exponentiation such that

$$a_{ij} = \exp(\beta a_{ij}^{I-1} Q_{ij}^A). \tag{5.9}$$

By means of the Sinkhorn method, entries are normalized iteratively in every row and column except for the slack variables ($a_{n_1+1j}$ and $a_{in_2+1}, \forall i, j$) until $A$ converges or the number of iterations, $I$, exceeds $I_{max}$:

$$\begin{aligned} a_{ij} &= \frac{a_{ij}}{\sum_{j=1}^{n_2+1} a_{ij}}, \quad i = 1, ..., n_1 \\ a_{ij} &= \frac{a_{ij}}{\sum_{i=1}^{n_1+1} a_{ij}}, \quad j = 1, ..., n_2. \end{aligned} \tag{5.10}$$

where the convergence criterion is

$$\frac{1}{n_1 \times n_2} \sum_{i=1}^{n_1} \sum_{j=1}^{n_2} |a_{ij}^I - a_{ij}^{I-1}| < \epsilon. \tag{5.11}$$

For every increasing correspondence index, $a_{ij}^I > a_{ij}^{I-1}$, we update its $B^{ij}$ in the same manner as explained above given weight coefficients of

$$Q_{kl}^B = \beta B_{kl}^{ij,I-1} \|\phi(v_{j,k}) - \phi(v_{i,l})\|_F. \tag{5.12}$$

Since $Q_{kl}^B$s are positive by definition of the Frobenius norm, there is no need for positivity enforcement here. We let $B_{kl}^{ij} = \beta Q_{kl}^B$. Rows and columns are normalized by recurse implementation of

$$\begin{aligned} B_{kl}^{ij} &= \frac{B_{kl}^{ij}}{\sum_{l=2}^{4} B_{kl}^{ij}}, \quad k = 2, ..., 4 \\ B_{kl}^{ij} &= \frac{B_{kl}^{ij}}{\sum_{k=2}^{4} B_{kl}^{ij}}, \quad l = 2, ..., 4 \end{aligned} \tag{5.13}$$

**Algorithm 4** Node matching algorithm

**Inputs:** $G_1$, $G_2$, $\beta_0$, $\beta_r < 1$, $\beta_f$, $I_{max}$, $\lambda$, and $\epsilon$
**Initialization:**
$a_{ij}^0 \leftarrow 0 \quad \forall\, i, j$
$B^{ij,0} \leftarrow B^{ij} \quad \forall\, i, j$
**Calculation:** signatures $\sigma_1$ and $\sigma_2$.
**while** $\beta \geq \beta_f$ **do**
  $I \leftarrow 1$
  $Q_{ij}^A \leftarrow \|\sigma_2(v_j) - \sigma_1(v_i)B^{ij}\|_F - \lambda$
  Positivity enforcement: $a_{ij} \leftarrow \exp(\beta a_{ij}^{I-1} Q_{ij}^A)$.
  **while** $A$ is not converged and $I < I_{max}$ **do**
    $a_{ij} = \frac{a_{ij}}{\sum_{j=1}^{n_2+1} a_{ij}}, \quad i = 1, ..., n_1$
    $a_{ij} = \frac{a_{ij}}{\sum_{i=1}^{n_1+1} a_{ij}}, \quad j = 1, ..., n_2$
    $a_{ij}^I \leftarrow a_{ij}$
    $I \leftarrow I + 1$
  **end**
  **for** $\{i = 1, \ldots, n_1,\ j = 1, \ldots, n_2 | a_{ij}^I > a_{ij}^{I-1}\}$ **do**
    $I \leftarrow 1$
    $Q_{kl}^B \leftarrow \beta B_{kl}^{ij,I-1} \|\phi(v_{j,k}) - \phi(v_{i,l})\|_F$.
    $B_{kl}^{ij} \leftarrow \beta Q_{kl}^B$.
    **while** $\frac{1}{9}\sum_{i=2}^{4}\sum_{j=2}^{4} |B^{ij,\,I} - B^{ij,\,I-1}| < \epsilon$ and $I < I_{max}$ **do**
      $B_{kl}^{ij} = \frac{B_{kl}^{ij}}{\sum_{l=2}^{4} B_{kl}^{ij}}, \quad i = 2, ..., 4$
      $B_{kl}^{ij} = \frac{B_{kl}^{ij}}{\sum_{k=2}^{4} B_{kl}^{ij}}, \quad l = 2, ..., 4$
      $B^{ij,I} \leftarrow B^{ij}$
      $I \leftarrow I + 1$
    **end**
  **end**
  $a_{ij}^0 \leftarrow a_{ij} \quad \forall\, i, j$
  $B^{ij,0} \leftarrow B^{ij} \quad \forall\, i, j$
  Anneal: $\beta \leftarrow \beta_r \beta$
**end**
**Binarization:** $A$ and $B^{ij} \quad i = 1, \ldots, n_1,\ j = 1, \ldots, n_2$.
**Output:** $A$ and $B^{ij} \quad i = 1, \ldots, n_1,\ j = 1, \ldots, n_2$

only for the lower right $3 \times 3$ sized part of the permutation matrices keeping the first element equal to one. Similar to $A$, iterations continue until reaching convergence or $I_{max}$. The convergence criterion is that

$$\frac{1}{9}\sum_{k=2}^{4}\sum_{l=2}^{4} |B_{kl}^{ij,\,I} - B_{kl}^{ij,\,I-1}| < \epsilon. \tag{5.14}$$

The annealing structure controls the updating processes. Starting from $\beta_0$, $\beta$ is gradually reduced with annealing rate $\beta_r$. The dual updates are repeated till convergence for each $\beta$ level. As $\beta$ decreases, the ratios in (5.10) and (5.13) approach one for variables with minimum weight (indicating the maximum correspondence) and zero for the rest. The process is repeated until $\beta$ reaches the final value $\beta_f$.

Matrices are then binarized through maximum element filtering of the solutions. In each row, the maximum valued element is turned into one and the rest of the elements are put to zero, $a_{ij} = 1$ if $a_{ij} \geq a_{ik}, k = 1, \ldots, n_2 + 1$.

Edges are matched subsequently using the following definition.

**Definition 1:** *Suppose attributed graphs* $G_1 = (V_1, E_1, \phi_1, \zeta_1)$ *and* $G_2 = (V_2, E_2, \phi_2, \zeta_2)$ *are corresponded with* $A$. *Let* $v_i, v_k \in V_1$ *and* $v_j, v_l \in V_2$. *Then,* $(v_i, v_k) \in E_1$ *and* $(v_j, v_l) \in E_2$ *are said to be matched if* $a_{ij} = a_{kl} = 1$.

## 5.5 Experiments

In this section, we evaluate the proposed method's performance using synthetic and clinical data to demonstrate its full matching power when challenged by different perturbation sources such as node displacement or outliers. Results are provided in terms of accuracy, robustness, and computational complexity measures.

The clinical data being in two modalities are collected by magnetic resonance angiography (MRA) and 3-dimensional rotational angiography (3DRA) of the cerebral vascular networks. Two examples are shown in Figures 5.5(a) and 5.5(b) respectively. The MRA images include vasculature across the entire brain whereas the 3DRA images show vasculature of either right or left hemisphere in a more exhaustive manner. In section 5.5.4, it will be shown that how the structural difference between vasculatures in these two modalities is exploited to test the method's performance more in depth. Synthetic graphs are derived from clinical data through application of non-linear operations described in section 5.5.1.

### 5.5.1 Pre-processing

Given segmented images of the cerebral blood vessels, their graph-based models are generated by means of [93]. Attributed graph models are then formed by following the procedure described in section 5.1.

Synthetic graphs are extracted from real network graphs that we call base graphs here, by implementing two sorts of perturbations (structural distortions) through a non-linear

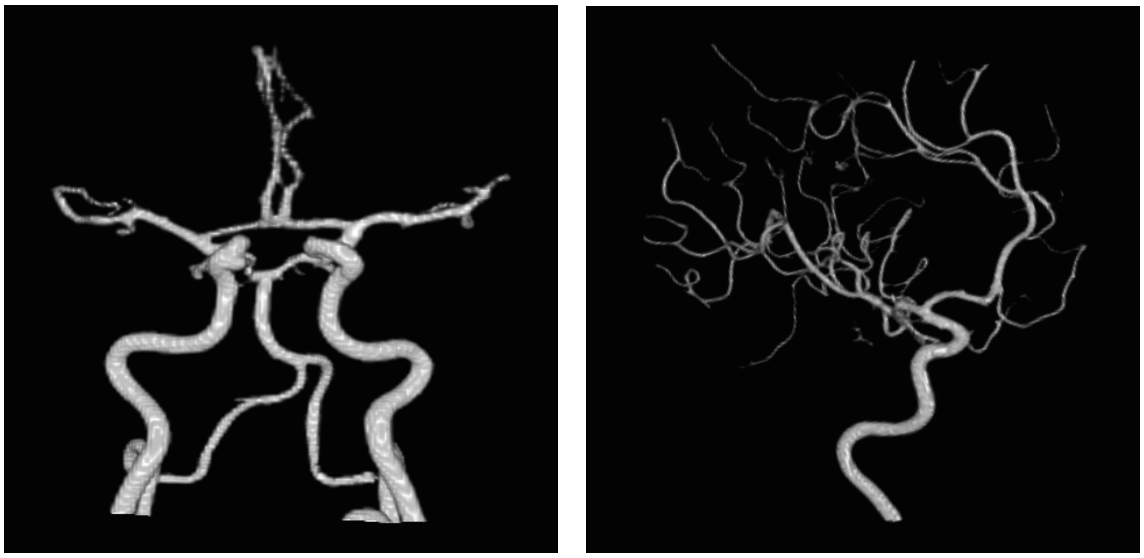

(a) (b)

Figure 5.5: (a) MRA and (b) 3DRA images of the cerebral vascular network.

transformation $\mathcal{T}$ of nodes defined as

$$w_j = \mathcal{T}(v_i) = \begin{cases} v_i + \eta & \text{with probability } (1-\alpha) \\ \varnothing & \text{otherwise} \end{cases} \tag{5.15}$$

where parameter $\alpha$ determines the percentage of removed nodes in the synthetic data ($n_{missed} = \alpha|V_i|$). Edges are also removed when each of their end nodes is missed in the synthetic graph. Displacements are produced by adding Gaussian noise $\eta \sim \mathcal{N}(0, \sigma_\eta^2)$ to every Cartesian coordinate of nodes. For every removed node, its linked edges are also removed from the synthetic graph. Throughout experiments, the base graph is considered as the ground truth and its synthetic variations are utilized to test the method against the problem size and location distortion factors controlled by $\alpha$ and $\sigma_\eta$.

### 5.5.2 Parameter tuning

Even though the overall performance of graduate assignment method is affected by the choice of $\beta$, it has been proved to converge and provide satisfactory results given well-tuned parameters [111]. In all the experiments, parameters related to this method, $\beta_0$, $\beta_r$, and $\beta_f$, are set as suggested by [86]. The $\beta_0$ is set to the largest square distance of all signature pairs. The annealing rate that balances between convergence rate and robustness has to be a value between 0.9 and 0.99. Here, we let $\beta_r = 0.95$. The $\beta_f$ is chosen to be equal to the average of the distances between connected nodes in signatures of the two graphs.

### 5.5.3 Validation metrics

Precision of the matching algorithm is measured in terms of sensitivity and specificity calculated for nodes and edges. Sensitivity or true positive rate (TPR) equals to the ratio of correctly detected matches to the total number of matched features (nodes or edges). Accordingly, specificity or true negative rate (TNR) is defined by the ratio of correctly detected outliers to the total number of unmatched features. Another precision measure is vertex similarity rate (VSR) that regards geometrical accuracy and is defined as

$$VSR = \frac{1}{N_{C_V}} \sum_{i=1}^{n_1} \sum_{j=1}^{n_2} \begin{cases} \|\phi_1(v_i) - \phi_2(v_j)\|^2 & \text{if } a_{i,j} = 1 \\ 0 & \text{otherwise} \end{cases} \tag{5.16}$$

where $N_{C_V}$ is the number of correctly matched vertices. This metric determines the extent of spatial distortion tolerance by the matching method. Likewise, edge similarity rate (ESR) provides a shape analogy measure for the correctly matched edges as

$$ESR = \frac{1}{N_{C_E}} \sum_{i,k=1}^{n_1} \sum_{j,l=1}^{n_2} \begin{cases} \|\zeta_1(v_i, v_k) - \zeta_2(v_j, v_l)\|^2 & \text{if } a_{i,j} = a_{k,l} = 1 \\ 0 & \text{otherwise} \end{cases}. \tag{5.17}$$

### 5.5.4 Performance evaluation

The key component in developing a graph matching technique especially for medical applications is robustness; its performance has to be minimally impacted by reasonable geometrical distortions and presence of outliers that prevalently occur in the data collected from different patients and even at different stages of a disease for an individual patient. Here, we show that how inclusiveness of the proposed signature feature regarding topological (connections) and geometrical information guarantees robustness of matchings in presence of the above-mentioned issues. This has been proved by the assessments that are made versus parameters causing structural variation via changing the problem size ($\alpha$), spatial distortion ($\sigma_\eta$), or optimization accuracy ($\lambda$). Figure 5.6 shows a base abstract graph and its three synthetic modifications in each of which one of the parameters has affected the structure. In the first synthetic graph shown in Figure 5.6(b), a fraction of the nodes are missed where $\alpha = 0.17, \sigma_\eta = 0$ and $\lambda = 10$. Figure 5.6(c) shows a graph with perturbations in the nodes location produced by having $\alpha = 0, \sigma_\eta = 10$, and $\lambda = 10$. The last synthetic graph is designed to test the effect of regularization parameter $\lambda$. For this reason, parameters are set as $\alpha = 0, \sigma_\eta = 5$, and $\lambda = 50$. The nodes are numerically labeled and edges are color-coded for visual appreciation of the matching results. In the synthetic graphs, nodes have double

labels. The label on the right side is the label of the node of the base that it is matched to where the left side label shows the ground truth. The right side label is replaced with a cross sign for outliers (non-matched nodes). The same concept holds for the edges but with colors. Every edge of the synthetic graphs are colored with the same hue as the edge they are matched to in the base graph. Non-matched edges are shown in black.

In order to assess the effect of graph size variation that comes with change of outlier numbers, a collection of synthetic data is produced from ten base graphs (5 from MRA and 5 from 3DRA data) by varying $\alpha$ from 0.1 to 0.5 with increments of 0.1 where $\sigma_\eta = 5$ and $\lambda = 100$. Averaged performance metrics for ten graphs are presented in Table 5.2.

Table 5.2: Performance measures versus problem size ($\alpha$).

| $\alpha$ | $TPR$ (node/edge) | $TNR$ (node/edge) | $VSR$ | $ESR$ |
|---|---|---|---|---|
| 0.1 | 0.93/0.84 | 0.83/0.88 | 5.92 | 13.98 |
| 0.2 | 0.89/0.87 | 0.87/0.86 | 7.47 | 12.24 |
| 0.3 | 0.92/0.88 | 0.90/0.91 | 7.88 | 10.93 |
| 0.4 | 0.94/0.90 | 0.91/0.95 | 8.39 | 5.87 |
| 0.5 | 0.95/0.92 | 0.92/0.97 | 9.01 | 2.75 |

The node related TPR shows an increase with rising of $\alpha$ except for a minimum at $\alpha = 0.2$. This behavior can be interpreted with the following argument. As the $n_{missed}$ increases (rising of $\alpha$) slightly, it is probable that one neighbor of the removed node will be matched to its corresponding node in the other graph resulting in falling of correct detections. However, with further node removal, the node density reduces and less meaningful structure remains to be matched. Thus, nodes can be matched with higher sensitivity (TPR increases). The edge related TPR also demonstrates an increasing pattern as more nodes are missed.

The specificity (TNR) increases homogeneously for node detection reflecting the increased power of method in correctly determining outliers as the problem size decreases. The specificity of edge matching increases in general except for a drop at $\alpha = 0.2$ that can be due to the same cause as is true for the node-based TPR. Therefore, reduction of edges as structural information results in performance improvement.

Evaluations regarding the node displacements level are carried out by tuning $\sigma_\eta$ with five levels uniformly spaced from 5 to 25 for the same base graphs as mentioned above. The reason for selection of these variance levels stems from the fact that the minimum distance between neighboring junctions in all data sets is greater than ten. For $\alpha = 0.1$

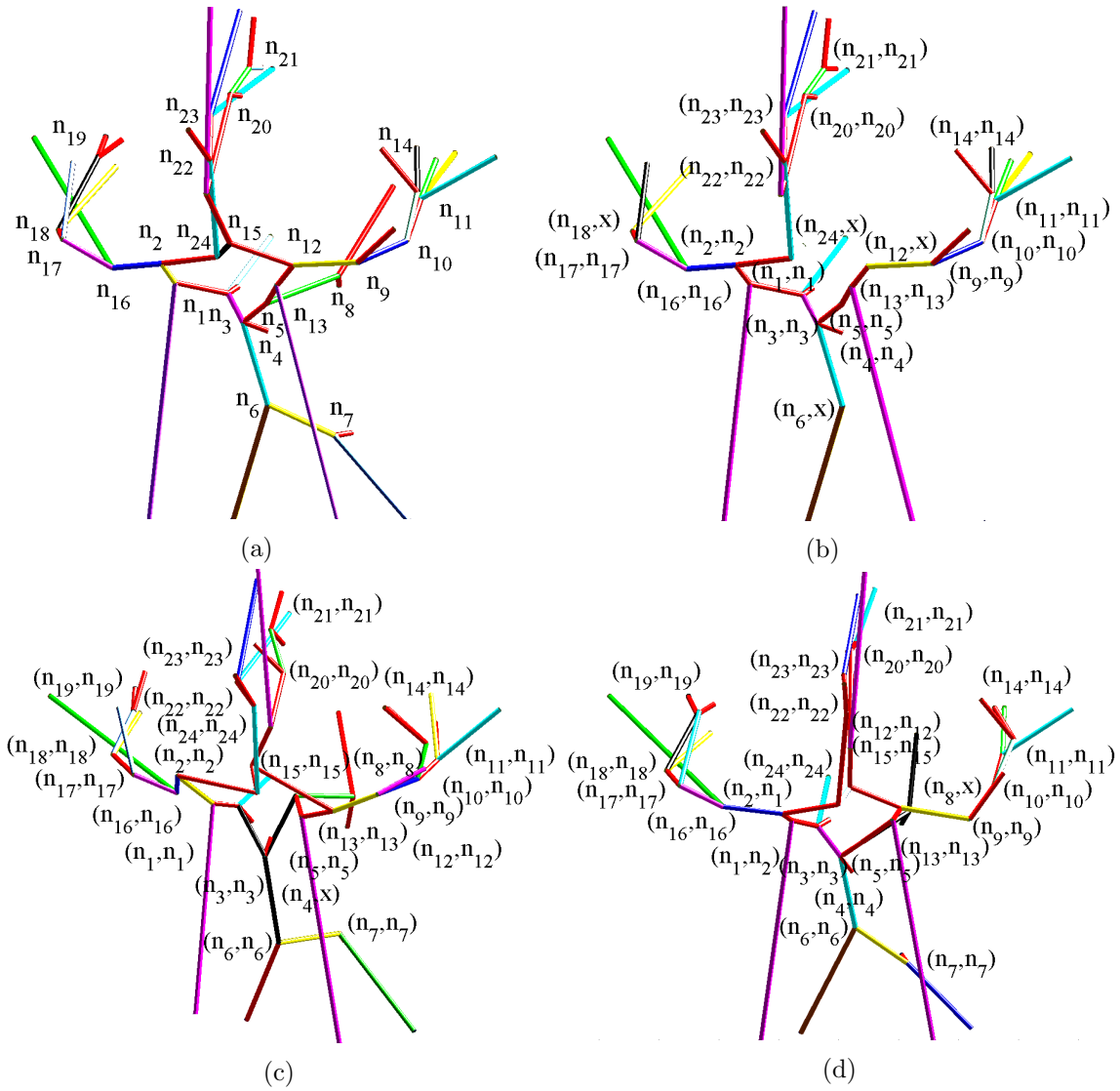


Figure 5.6: (a) A base MRA-driven abstract graph and its synthetic modification with (b) $\alpha = 0.17, \sigma_\eta = 0$, and $\lambda = 10$, (c) $\alpha = 0, \sigma_\eta = 10$, and $\lambda = 10$, and (d) $\alpha = 0, \sigma_\eta = 5$, and $\lambda = 50$. The synthetic nodes labels reflect the ground truth (left) and the label of the node that they are matched to (right) (this replaces with a cross sign for outliers). Matched edges are safely colored where un-matched edges are presented in black.

and $\lambda = 100$, averaged performance measures are given in Table 5.3. According to these results, the performance decreases with larger displacements in both of the sensitivity and specificity senses.

Next, we present the experimental results that show the effect of regularization parameter on the precision of algorithm. Synthetic graphs are built similar to the other two cases

Table 5.3: Performance measures versus nodes displacement level ($\sigma_\eta$).

| $\sigma_\eta$ | $TPR$ (node/edge) | $TNR$ (node/edge) | $VSR$ | $ESR$ |
|---|---|---|---|---|
| 5 | 0.93/0.92 | 0.83/0.88 | 5.92 | 13.98 |
| 10 | 0.87/0.85 | 0.79/0.83 | 7.26 | 18.84 |
| 15 | 0.86/0.79 | 0.71/0.75 | 9.04 | 21.09 |
| 20 | 0.73/0.68 | 0.68/0.69 | 14.86 | 26.05 |
| 25 | 0.65/0.60 | 0.64/0.57 | 15.11 | 29.10 |

described above having $\alpha = 0.1$ and $\sigma_\eta = 5$. Given the matched nodes and edges obtained from solving the optimization of (5.3) for $\lambda$ values ranging from 10 to 200, performance metrics are calculated and results are provided in Table 5.4. Results show that setting the $\lambda$ for the distance tolerance term ($\|A\|_F$) can be difficult. Large values of $\lambda$ greatly limit the range of matching non-rigidity. On the other hand, the matching becomes too flexible at small values of $\lambda$ increasing false matchings.

Table 5.4: Performance measures versus the regularization parameter ($\lambda$).

| $\lambda$ | $TPR$ (node/edge) | $TNR$ (node/edge) | $VSR$ | $ESR$ |
|---|---|---|---|---|
| 10 | 0.95/0.93 | 0.81/0.76 | 5.92 | 13.98 |
| 50 | 0.93/0.92 | 0.83/0.88 | 5.92 | 13.98 |
| 100 | 0.83/0.76 | 0.89/0.79 | 7.75 | 17.65 |
| 150 | 0.79/0.70 | 0.78/0.69 | 9.46 | 24.87 |
| 200 | 0.75/0.68 | 0.71/0.65 | 10.87 | 30.47 |

### 5.5.5 Inter-subject matching

Here, we deliver the results acquired from testing the algorithm handling inter-subject cases to prove its power against real perturbations. As follows, we use the matching results and the $VSR$ metric to probe the anatomical variations of vasculature according to different samples and the level of branches from the CoW. Since the MRA images only include less and more discriminating levels of vessel branches by nature and as shown in Figure 5.5, we have limited the investigations to this type of data.The results are provided for 36 pair-wise matchings of nine given graphs. The ground truth is determined via the real angiography images.

A sample of this type of matching is shown in Figure 5.7 for two GGMs extracted from

MRA images. Double headed arrows show the derived junction correspondences.

The statistical measures of the TPR and TNR for matching 36 pairs of graphs derived

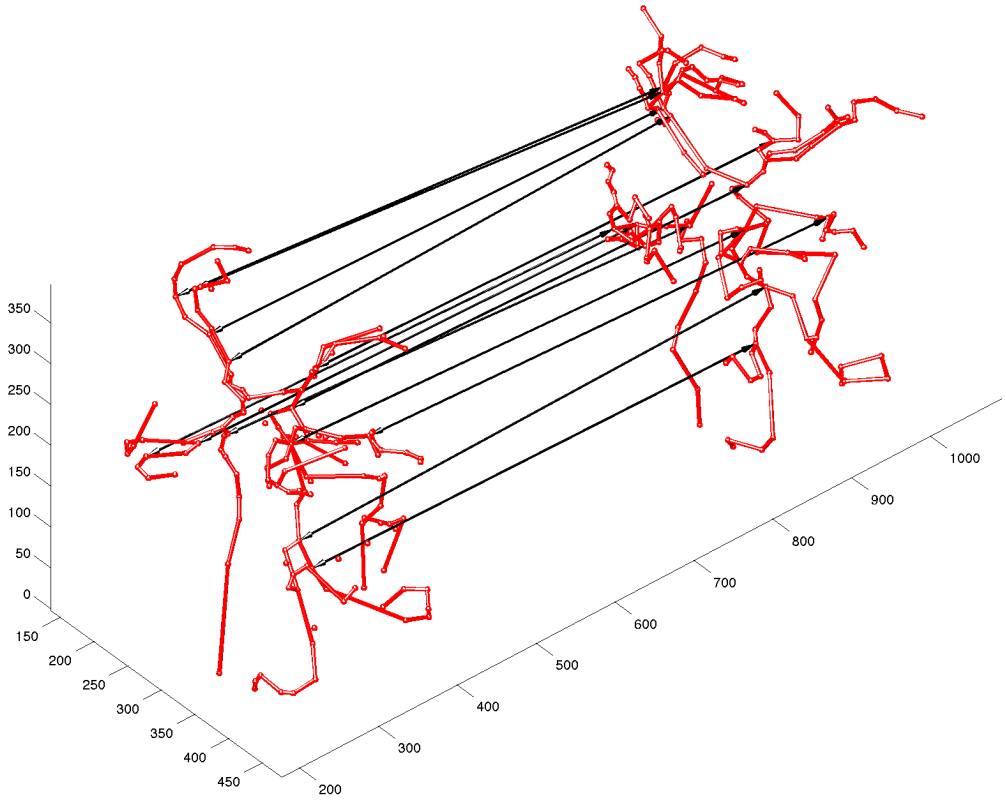


Figure 5.7: Junction correspondences (marked by double headed arrows) of graphs derived from two different data.

from MRA data are provided in Figures 5.8(a) and (b) for nodes and edges respectively. The sensitivity of node matching shows to be more affected by the structural variations where its average is close to the mean of sensitivity that is around 80%. The edge matching sensitivity is around 74% on average where the average of specificity falls around 71%. The lower TNR is due to the relatively higher number of non-matched edges as they are dependent on four nodes to be matched. Therefore, the number of matchings decreases with a higher rate than nodes.

Figure 5.9 presents the $VSR$ measure for correctly matched nodes of 36 pairs of registered graphs versus their levels form the CoW. The MRA images consist only five levels of nodes counting from the circle of Willis. In addition to the large structural variations between samples, the quality of segmentations also affects the number of matched nodes.

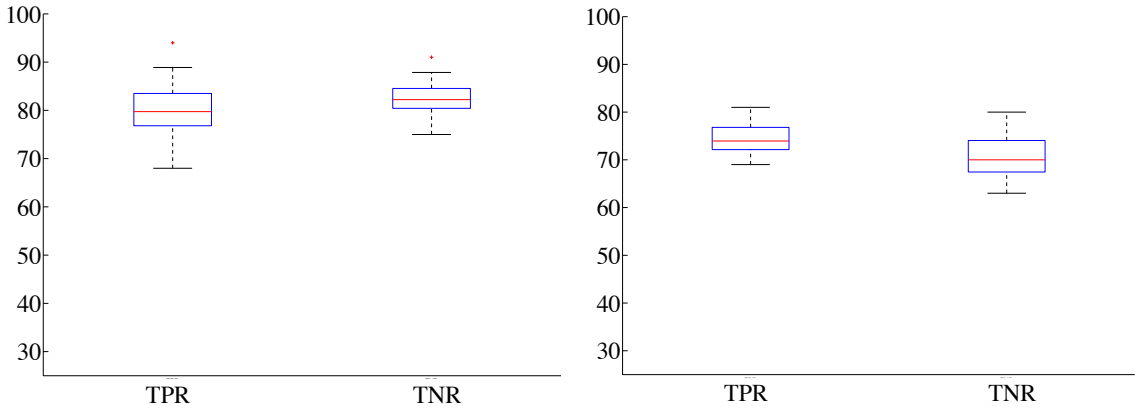


Figure 5.8: Statistical measures of TPR and TNR for matching (a) nodes and (b) edges of 36 pairs of graphs derived from nine MRA images.

Thus, the number of samples is not necessarily 36 for each level.

This plot proves the claim in Section 5.2 on the larger variations of node locations

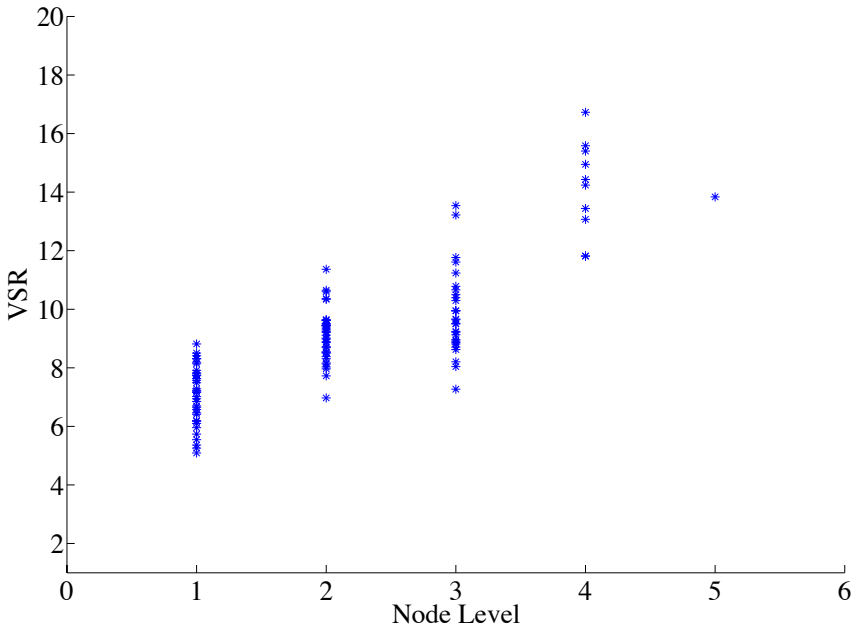


Figure 5.9: The anatomical change analysis as $VSR$ measure vs. the level of nodes from the CoW.

relative to their distance from CoW. However, they yet can be matched with high precision. We observe that the larger $VSR$ amounts emanates from the larger translational momenta that comes with larger radial distances rather than changes in the anatomical shapes or

topology of the networks.

### 5.5.6 Multi-modal matching

Due to invasiveness of imaging modalities such as 3DRA which calls for contrast injection, it is of great importance to develop methods capable of multimodal matching. To prove our algorithm's capacity in this respect, we consider its application to MRA and 3DRA images. Graphs obtained from MRA images that include vasculature across the entire brain are matched with the graphs derived from 3DRA images that represent only vasculature from either right or left hemispheres but with more structural details. Therefore, there is larger number of outliers compared to mono-modal matchings. The node and edge related accuracy measures (TPR and TNR) obtained from matching 25 graph pairs (5 from MRA and 5 from 3DRA data) are presented in the plots of Figure 5.10(a) and (b). The performance metrics for this type of matching display more variance. The TPR of node matchings is around 85% on average where this value is about 38% for TNR. The dramatic reduction of specificity stems from the high number of non-matched nodes in the 3DRA data pulling down the ratio. The edge matching performs with a slightly lower efficiency than the node matching. The TNR shows a rather low mean (about 24%) and variance similar to the node matching case.

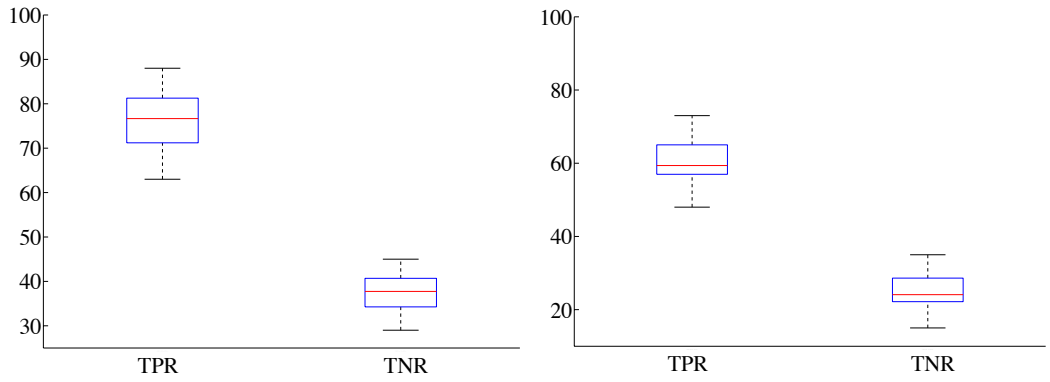


Figure 5.10: Statistical measures of TPR and TNR for matching (a) nodes and (b) edges of 25 graphs derived from five MRA and five 3DRA images.

### 5.5.7 Computatinal complexity

Conducive to determining the computational complexity, a clinical driven graph is set as reference and varying size test graphs are obtained by gradually removing the terminal nodes. The reference graph is then reduced in size similarly and the final result includes a range of problem sizes, $n_1 \times n_2$, from 1 to 324. The run time of matching these graphs is distributed from 0.29 to 21.72 seconds measured on a 1.7 GHz CPU and 4.00 GB RAM platform. Results shown in Figure 5.11 that are linearly normalized to the unit interval for visual clarity suggest that the execution time is linearly dependent on the problem size. Being tree graphs, the number of edges equals to $n_V - 1$, thus it does not rule the run time independently. Therefore, we haven't investigated its effect as a separate parameter.

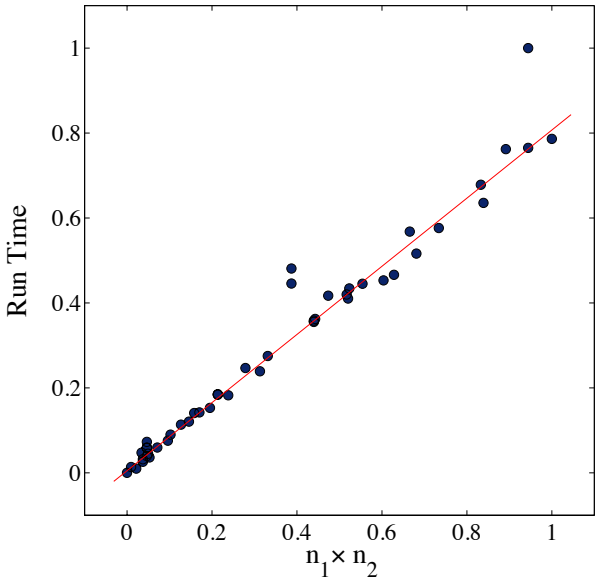


Figure 5.11: Run time of the registration algorithm versus problem size $n_1 \times n_2$. Values are linearly normalized to unit interval for both axes.

# Chapter 6

# Conclusion and Future Work

The core of this work is about developing methods that identify and register the piecewise linear approximation (or GGM) of the vascular networks centerlines based on specific geometrical features of these tubular structures. This goal has been achieved in three steps. First, a pre-processing method is designed that retrieve vasculature from raw data. Next, a GGM identification method is proposed that does not require a precise segmentation and advantageously works on a rough binary representation of the vasculature of arbitrary shape. Finally, the GGMs are efficiently registered through a novel method that factorizing the topology into the local connections.

## 6.1 Volumetric extraction of microvasculature

The first part of dissertation addresses the segmentation problem of 3-D vascular networks. A novel iterative algorithm is proposed that is based on a bi-scale filtering scheme. The proposed method is tested on the fluorescence microscopy images of the murine cranial microvasculature. These images manifest miscellaneous types of noise, varying SNRs, uneven contrast, and structural complexity that prove to be challenging for existing segmentation methods even when they process denoised and pre-processed data. Our method iteratively retrieves the vasculature and robustly builds the structural pattern of interest while rejecting the imaging artifacts. The search algorithm uses a greedy approach which selects the locally optimal voxels that are in compliance with the structure at each iteration. These voxels are the points for which the radial distance and standard intensity deviation are in the acceptable range from the given retrieved region. Evaluations on real fluorescence microscopy and synthetic data show that the presented method has high specificity and sensitivity while it outperforms state-of-the-art methods. Without loss of generality, this

method is applicable to images of two dimension and with less computational complexity.

The segmentation method can be generalized to images of other tubular shapes including neurons and retina's vasculature with some modifications such as scaling. Even though the algorithm has proved to perform superior to state-of-the-art denoising and segmentation methods, it will highly benefit from an analytical probabilistic justification. Also, it can be adapted for different imaging modalities with different probabilistic models of noise.

## 6.2 Geometrical graph-based model identification

We have developed an accurate process for graph-based skeletal model identification of 3-D vascular networks and demonstrated its capabilities in the processing of fluorescence microscopy data collected in a murine model. Novel algorithms for critical points (junctions and waypoints) detection and graph extraction have been developed that enable the semi-automatic delineation of 3-D interconnected tubular networks. Critical point detection required no prior information about the degree of junctions, direction of branches, or curvature of vessels. A binary integer programming approach was used to identify optimal edges connecting the critical points where optimality was defined in terms of the degree to which possible edges in the graph aligned with and overlapped vessel structure. Exploiting the structural specifications of loopy networks in addition to the local intensity statistics in the design of these algorithms has made them robust to the data imperfections like noise and inhomogeneous illumination that are very common specifically in fluorescence microscopy images. This claim has been empirically verified by the experimentation results presented in Chapter 4.

Development of the divide-and-conquer approach has reduced the computational complexity of the proposed algorithm. A large data set is decomposed into a collection of non-overlapping blocks, networks are identified in each, and then stitched together using a bipartite matching method to connect boundary points across neighboring block faces. With such a decomposition of the problem, all of the blocks could, given sufficient computing resources, be processed in parallel. In this case, the latency of the processing is dictated by the maximum time needed for a given block. For the data and multiple tessellations into blocks considered here, the maximum time over all blocks generated by the 12 four-block divisions of data discussed in Section 4.4.7 was 8542 s. For the forty-eight cases of 16-block partitioning case this number is 5696 s, while the maximum time to process any block from 64-block division was 161 s. Based on these numbers a parallel implementation of the method would likely be scalable. Even where we are limited to processing blocks

sequentially, the results are still encouraging. The median time to processing all four blocks one-after-the-other in the twelve cases was 15,149 s. These numbers drop to 1718 s in the 16-block case and 735 s for 64 decompositions. Again, the total run time has greatly been affected by the partitioning as we see it has been reduced by factor of 20.6 from four to 64 partitions.

However, designing accurate and computationally feasible techniques that improve the scalability without performing the divide-and-conquer approach is an open problem to investigate. Also, additional work on the divide and conquer approach can be conducted to examine the effect of block shapes in the performance *e.x.* the necessity of having uniform subdivisions. Giving spatial adaptivity to the divisions is specifically an important case to study.

The network model detected by this method gives an efficient and accurate foundation for future efforts in general vasculature segmentation. Another area of development is related to automizing the selection of spherical shell thickness, $\delta_\rho$, and Gaussian kernel standard deviation, $\sigma_G$, in accordance to the data specifications.

We have observed that performance of the CP detection process is sensitive to the quality of segmentation and shape of the vasculature. For instance, the GGM identification method faces challenges forming discriminating utility functions when processing structures with either longer and less curved or highly tortuous branches as precise CPs have not been found. Thus, it is crucial for having a broader application to modify the three steps of convex hull filtering, spherical shell filtering, and agglomerative clustering to produce robuster CPs to noise and structural variation factors.

Completing these studies and extending the method developed here to a broader range of tubular identification problems constitutes our primary areas of continued investigation.

## 6.3 Geometrical graph-based model registration

The human cranial artery networks show specific geometric properties in structure that motivated us to investigate the application of graph matching to the GGMs. Due to imaging and image processing artifacts and inter-subject variations, graphs manifest different node counts and edge distortions. In the literature, graph matching of this type of data are considered inexact matching or sub-graph isomorphism and are usually approached by solving an NP-hard quadratic assignment problem. In this work, we exploited the intuition that two nodes are correspondent if their neighbors correspond maximally to build a novel feature that embodies geometrical attributes of nodes (location of junctions) and edges (length

and curvature of vessels) in a topology encoded form. This feature termed signature, allows formulating the matching problem in a linear assignment problem rather than a QAP form through solving which nodes of the geometrically induced attributed graphs are matched efficiently. Using signatures, we relaxed the topology locally and reduced the computational complexity profoundly. Through relaxing the assignment matrix to be doubly stochastic and having continuous elements, a combinatorial problem is turned into a convex optimization. Nodes are first matched via Graduated Assignment (GA) technique, and then the edge correspondences are determined using a heuristic approach. The performance of this method is tested using clinical angiography images and synthetic data sets. Quantitative results in the form of sensitivity and specificity of matched nodes and edges, suggest that this method is highly reliable under the influence of different perturbing factors like node displacement and problem size. Quality of inter-subject and multimodal matching of clinical data have also been confirmed through provided results.

One area of future work for this part would be establishing methods that register intensity-based images of tubular structures using their GGMs. This provides two-fold advantages: A noticeably lower number of data points are needed for registration when graphs are the subject of study rather than full images, and the topological information is also considered in finding the correspondences (increasing the morphology change tolerance where structures appear with large variations) that is lacking with intensity or geometry-based techniques.

Another path to consider for further investigation is increasing the method's capacity by adding flexibility to the number of connections in the signature definition. If the proposed registration method allows arbitrary number of connections rather than restricting it to three, it will be more efficiently applicable to graphs obtained from vasculature of any shape and in a more general sense, all attributed graphs.

Studying statistics on tree-structured objects has recently become subject of growing number of studies [112, 113] as it would have a wide range of applications. However, the existing works on finding tree distances are algorithmic rather than geometric. This indeed yields difficulties in the problem of finding the mean of trees, and only a limited number of methods are designed for analysis of tree shapes. Thus, this field is remained as an open area of research. The GGMs and proposed registration technique could be used to build a shape analysis framework. Resulting from such a framework would be discrete vascular atlases that are quantitative gold standards for anatomical morphology in medical studies. A multi-graph matching based on the pair-wise registration results can potentially result in a mean graph, and *e.x.* PCA analysis of the matched attributes between healthy samples

yields normal modes of structural and attributal variations.

# Bibliography


[1] M. Jackowski, X. Papademetris, L.W. Dobrucki, A.J Sinusas, and L.H. Staib, "Characterizing vascular connectivity from microCT images," Medical Image Computing and Computer-Assisted Intervention (MICCAI), 701–708 (2005).

[2] D. Lesage, E.D. Angelini, I. Bloch, and G. Funka-Lea, "A review of 3D vessel lumen segmentation techniques: Models, features and extraction schemes," J. Medical image analysis, **13**(6), 819–845 (2009).

[3] J. Kim, W.J. Oh, N. Gaiano, Y. Yoshida, and C. Gu, "Semaphorin 3E-Plexin-D1 signaling regulates VEGF function in developmental angiogenesis via a feedback mechanism," Genes Dev **25**(13), 1399–1411 (2011).

[4] P. Blinder, P.S. Tsai, J.P. Kaufhold, P.M. Knutsen, H. Suhl, and D. Kleinfeld, "The cortical angiome: an interconnected vascular network with noncolumnar patterns of blood flow," Nat Neurosci **16**(7), 889–897 (2013).

[5] P.S. Tsai, J.P Kaufhold, P. Blinder, B. Friedman, P.J. Drew, H.J Karten, D.L. Patrick, and D. Kleinfeld, "Correlations of neuronal and microvascular densities in murine cortex revealed by direct counting and colocalization of nuclei and vessels," J. Neuroscience, **29**, 14553–14570 (2009).

[6] S.R. Aylward, J. Jomier, S. Weeks, and E. Bullitt, "Registration and analysis of vascular images," Int. J. Comput. Vision **55**(2-3), 123–138 (2003).

[7] E. Bullitt, S.R. Aylward, A. Liu, J. Stone, S.K. Mukherji, C. Coffey, G. Gerig, S.M., Pizer, "3D graph description of the intracerebral vasculature from segmented MRA and tests of accuracy by comparison with X-ray angiograms," J. Information Processing in Medical Imaging, 308–321 (1999).

[8] C. Kirbas and F. Quek, "A review of vessel extraction techniques and algorithms," ACM Computing Surveys (CSUR) **36**(2), 81–121 (2004).

[9] L. Younes, "Spaces and manifolds of shapes in computer vision: An overview," Image and Vision Computing, **30**(6), 389–397 (2012).

[10] T.B. Sebastian and B.B. Kimia, "Curves vs. skeletons in object recognition," Signal Processing, **85**(2), 247–263 (2005).

[11] X. Bai and L.J. Latecki, "Path similarity skeleton graph matching," Pattern Analysis and Machine Intelligence, IEEE Transactions on, **30**(7), 1282–1292 (2008).

[12] P. Sarder and A. Nehorai, "Deconvolution methods for 3-D fluorescence microscopy images," IEEE Signal Processing Magazine **23**(3), 32–45 ( 2006).

[13] J.S. Suri, K. Liu, L. Reden, and S. Laxminarayan, "A review on MR vascular image processing algorithms: acquisition and prefiltering: part I," IEEE Trans. Inform. Technol. Biomed, **6**, 324–337 (2002).

[14] R. Wang, C. Li, J. Wang, X. Wei, Y. Li, Y. Zhu, and S. Zhang, "Threshold segmentation algorithm for automatic extraction of cerebral vessels from brain magnetic resonance angiography images," J. neuroscience methods, **241**, 30–36 (2015).

[15] F. Kording, C. Weidensteiner, S. Zwick, N. Osterberg, A. Weyerbrock, O. Staszewski, D. Elverfeldt, and W. Reichardt, "Simultaneous assessment of vessel size index, relative blood volume, and vessel permeability in a mouse brain tumor model using a combined spin echo gradient echo echo-planar imaging sequence and viable tumor analysis," J. Magnetic Resonance Imaging, **40**(6), 1310–1318 (2014).

[16] J. Boulanger, C. Kervrann, P. Bouthemy, P. Elbau, J.B. Sibarita, and J. Salamero, "Patch-based nonlocal functional for denoising fluorescence microscopy image sequences," IEEE Transactions on Medical Imaging **29**(2), 442–454 (2010).

[17] F. Luisier, T. Blu, and M. Unser, "Image denoising in mixed Poisson-Gaussian noise," IEEE Transactions on Image Processing **20**(3), 696–708 (2011).

[18] P. M. Carlton, J. Boulanger, C. Kervrann, J.B. Sibarita, J. Salamero, S. Gordon-Messer, D. Bressang, J.E. Haberg, S. Haaseh, L. Shaoa, L. Winotoa, A. Matsudaa, P. Knera, S. Uzawai, M. Gustafssona, Z. Kamj, D.A. Agard, and J. W. Sedat, "Fast live simultaneous multiwavelength four-dimensional optical microscopy," Proceedings of the National Academy of Sciences, **107**(37), 16016–16022 (2010).

[19] J.G. White, W.B. Amos, and M. Fordham, "An evaluation of confocal versus conventional imaging of biological structures by fluorescence light microscopy," The Journal of cell biology, **105**(1), 41–48 M (1987).

[20] S.D. Olabarriaga and A.W. Smeulders, "Interaction in the segmentation of medical images: A survey," J. Medical image analysis **5**(2), 127–142 (2001).

[21] T.F. Chan and L.A. Vese, "Active contours without edges," IEEE Transactions on Image Processing **10**(2), 266–277 (2001).

[22] P. Yan and A.A. Kassim, "MRA image segmentation with capillary active contours," Med. Image Anal. **10**(3), 317–329 (2006).

[23] X. Qian, M.P. Brennan, D.P. Dione, W.L. Dobrucki, M.P. Jackowski, C.K., Breuer, A.J. Sinusas, and X. Papademetris, "A non-parametric vessel detection method for complex vascular structures," Medical image analysis **13**(1), 49–61(2009).

[24] V. Mahadevan, H. Narasimha-Iyer, B. Roysam, and H.L. Tanenbaum, "Robust model-based vasculature detection in noisy biomedical images," Information Technology in Biomedicine, IEEE Transactions on **8**(3), 360–375 (2004).

[25] S. Eiho, H. Sekiguchi, N. Sugimoto, T. Hanakawa, and S. Urayama, "Branch-based region growing method for blood vessel segmentation," In Proceedings of International Society for Photogrammetry and Remote Sensing Congress, 796–801 (2004).

[26] J. Lee, P. Beighley, E. Ritman, and N. Smith, "Automatic segmentation of 3D micro-CT coronary vascular images," Medical image analysis, **11**(6), 630–647 (2007).

[27] O. Friman, M. Hindennach, and H.O. Peitgen, "Template-based multiple hypotheses tracking of small vessels," Proc. IEEE Int. Symp. Biomed. Imaging, 1047–1050 (2008).

[28] M. Sofka and C. V. Stewart, "Retinal vessel centerline extraction using multiscale matched filters, confidence and edge measures," Medical Imaging, IEEE Transactions on, **25**(12), 1531–1546 (2006).

[29] K. Krissian, G. Malandain, N. Ayache, R. Vaillant, and Y. Trousset, "Model-based detection of tubular structures in 3D images," Computer vision and image understanding, **80**(2), 130–171 (2000).

[30] E. Meijering, "Cell segmentation: 50 years down the road [life sciences]," IEEE Signal Processing Magazine, **29**(5), 140–145 (2012).

[31] Y. Zhu, F. Li, T.J. Vadakkan, M. Zhang, J. Landua, W. Wei, J. Ma , M.E. Dickinson , J.M. Rosen , M.T. Lewis , M. Zhan, and S.T. Wong, "Three-dimensional vasculature reconstruction of tumour microenvironment via local clustering and classification," Interface focus, **3**(4), 20130015 (2013).

[32] H. Homann, "Implementation of a 3D thinning algorithm," J. Insight ( 2007).

[33] L. Wang, C. Li, Q. Sun, D. Xia, and C.Y Kao, "Active contours driven by local and global intensity fitting energy with application to brain MR image segmentation," Comput. Med. Imaging Graph, **33**, 520–531 (2009).

[34] M.A. Gulsun and H. Tek, "Robust vessel tree modeling," Med. Image Computing and Computer-Assisted Intervention (MICCAI), 602–611 (2008).

[35] V. Megalooikonomou, M. Barnathan, D. Kontos, P.R. Bakic, and A.D Maidment, "A representation and classification scheme for tree-like structures in medical images: analyzing the branching pattern of ductal trees in X-ray galactograms," IEEE Trans. Med. Imaging **28**, 487–493 (2009).

[36] S. Olabarriaga, M. Breeuwer, and W. Niessen, "Minimum cost path algorithm for coronary artery central axis tracking in CT images," Med. Image Comput. Comput.-Assisted Intervention (MICCAI), 687–694 (2003).

[37] C. Pisupati, L. Wolff, W. Mitzner, and E. Zerhouni, "A central axis algorithm for 3D bronchial tree structures," In: IEEE International Symposium on Computer Vision, 259–264 (1995).

[38] E. Türetken, G. Gonzlez, C. Blum, and P. Fua, "Automated reconstruction of dendritic and axonal trees by global optimization with geometric priors," J. Neuroinform, **9**, 279–302 (2011).

[39] J. Jomier, V. LeDigarcher, and S.R. Aylward, "Automatic vascular tree formation using the mahalanobis distance," Medical Image Computing and Computed-Assisted Intervention (MICCAI), 806–812 (2005).

[40] S.R. Aylward and E. Bullitt, "Initialization, noise, singularities, and scale in height ridge traversal for tubular object centerline extraction," IEEE Transactions on Medical Imaging **21**(2), 61–75 (2002).

[41] H. Li and A. Yezzi, "Vessels as 4-D curves: global minimal 4-D paths to extract 3-D tubular surfaces and centerlines," IEEE Transaction on Medical Imaging, **26**, 1213–1223 (2007).

[42] J. Rittscher, R. Machiraju, and S.T, Wong, "Microscopic Image Analysis for Life Science Applications," Artech House (2008).

[43] E. Türetken, F. Benmansour, B. Andres, H. Pfister, and P. Fua, "Reconstructing Loopy Curvilinear Structures Using Integer Programming," CVPR (2013).

[44] H. Bogunovic, J.M. Pozo, R. Crdenes, L. San Romn, A.F. Frangi, "Anatomical labeling of the circle of willis using maximum a posteriori probability estimation," IEEE Transaction on Medical Imaging, **32**(9), 1587–1599 (2013).

[45] K.L. Hoffman and T.K. Ralphs, "Integer and combinatorial optimization," In: Encyclopedia of Operations Research and Management Science. Springer, US, 771–783 (2013).

[46] J.H. Metzen, T. Krger, A. Schenk, S. Zidowitz, H.O. Peitgen, and X. Jiang, "Matching of anatomical tree structures for registration of medical images," Image and Vision Computing, **27**(7), 923–933 (2009).

[47] U. Mitrovic, Z. Spiclin, B. Likar, and F. Pernus, "3D-2D registration of cerebral angiograms: a method and evaluation on clinical images," Medical Imaging, IEEE Transactions on, **32**(8), 1550–1563 (2013).

[48] P. Foggia, G. Percannella, and M. Vento, "Graph matching and learning in pattern recognition in the last 10 years," International Journal of Pattern Recognition and Artificial Intelligence, **28**(01), (2014).

[49] M.F. Demirci, A. Shokoufandeh, Y. Keselman, L. Bretzner, and S. Dickinson, "Object recognition as many-to-many feature matching," International Journal of Computer Vision, **69**(2), 203–222 (2006).

[50] R. Singh, J. Xu, and B. Berger, "Pairwise global alignment of protein interaction networks by matching neighborhood topology," In Research in computational molecular biology, Springer Berlin Heidelberg, 16–31 (2007).

[51] G.W. Klau, "A new graph-based method for pairwise global network alignment," BMC bioinformatics, **10**(1), S59 (2009).

[52] D. Conte, P. Foggia, C. Sansone, M. Vento, "Thirty years of graph matching in pattern recognition," Int. J. Pattern Recognit. Artif. Intell. **18**, 265–298 (2004).

[53] R.E. Burkard, "Quadratic assignment problems," Springer, New York, 2741–2814 (2013).

[54] J. Yan, J. Wang, H. Zha, X. Yang, and S. Chu, "Consistency-driven Alternating Optimization for Multi-Graph Matching: a Unified Approach," (2015).

[55] S.Z. Selim and M.A. Ismail, "K-means-type algorithms: a generalized convergence theorem and characterization of local optimality," IEEE Transactions on Pattern Analysis and Machine Intelligence, **1**, 81–87 (1984).

[56] L. Bottou and Y. Bengio, "Convergence Properties of the K-Means Algorithms," In Advances in Neural Information Processing Systems (NIPS) Conference, Denver, Colorado, USA, 585–592 (1994).

[57] T. Kanungo, D.M. Mount, N.S. Netanyahu, C.D. Piatko, R. Silverman, and A.Y. Wu, "An efficient k-means clustering algorithm: Analysis and implementation," IEEE Transactions on Pattern Analysis and Machine Intelligence, **24**(7), 881–892 (2002).

[58] Q. Du, V. Faber, and M. Gunzburger, "Centroidal Voronoi tessellations: applications and algorithms," SIAM review, **41**(4), 637–676 (1999).

[59] C.A. Sugar and G.M. James, "Finding the number of clusters in a dataset," Journal of the American Statistical Association, **98**(463), (2003).

[60] D.J. Ketchen and C.L. Shook, The application of cluster analysis in strategic management research: an analysis and critique. Strategic management journal, **17**(6), 441–458 (1996).

[61] N. Otsu, "A threshold selection method from gray-level histograms," IEEE Transactions on Systems, Man, and Cybernetics, **9**(1), 62-66 (1979).

[62] A.J. Izenman, "Modern multivariate statistical techniques," New York: Springer, **1** (2008).

[63] W.H.E. Day, H. Edelsbrunner, "Efficient algorithms for agglomerative hierarchical clustering methods," J. Classification. **1**, 7–24 (1984).

[64] J.T. Linderoth and M.W. Savelsbergh, "A computational study of search strategies for mixed integer programming," INFORMS Journal on Computing, **11**(2), 173–187 (1999).

[65] K. Hoffman and M. Padberg, "LP-based combinatorial problem solving," Annals of Operations Research, **4**(1), 145–194 (1985).

[66] G.B. Dantzig and M.N. Thapa, "Linear programming 2: theory and extensions," Springer Science and Business Media (2006).

[67] H.W. Kuhn, "The Hungarian method for the assignment problem," Naval research logistics quarterly, **2**(1-2), 83–97 (1955).

[68] S. Umeyama, "An Eigendecomposition Approach to Weighted Graph Matching Problems," IEEE Trans. Pattern Analysis and Machine Intelligence, **10**(5), 695–703, (1988).

[69] T. Cour, P. Srinivasan, and J. Shi, "Balanced graph matching," Advances in Neural Information Processing Systems, **19**, 313 (2007).

[70] M. Leordeanu and M. Hebert, "A spectral technique for correspondence problems using pairwise constraints," IEEE International Conference on Computer Vision (ICCV), **2**, 1482–1489 (2005).

[71] H.F. Wang and E.R. Hancock, "Correspondence Matching Using Kernel Principal Components Analysis and Label Consistency Constraints," Pattern Recognition, **39**(6), 1012–1025, (2006).

[72] T. Caelli and S. Kosinov, "An Eigenspace Projection Clustering Method for Inexact Graph Matching," IEEE Trans. Pattern Analysis and Machine Intelligence, **26**(4), 515–519 (2004).

[73] M. Zaslavskiy, F. Bach, and J.P. Vert, "A path following algorithm for the graph matching problem," IEEE Transactions on Pattern Analysis and Machine Intelligence, **31**(12), 2227-2242 (2009).

[74] H. Almohamad and S. Duffuaa, "A Linear Programming Approach for the Weighted Graph Matching Problem," IEEE Trans. Pattern Analysis and Machine Intelligence, **15**(5), 522–525, May (1993).

[75] S. Gold and A. Rangarajan, "A graduated assignment algorithm for graph matching," Pattern Analysis and Machine Intelligence, IEEE Transactions on, **18**(4), 377–388 (1996).

[76] C. Schellewald and C. Schnor, "Probabilistic Subgraph Matching Based on Convex Relaxation," Lecture Notes in Computer Science, **3757**, 171–186, Springer, (2005).

[77] B.T. Messmer and H. Bunke, "A new algorithm for error-tolerant subgraph isomorphism detection," IEEE Transactions on Pattern Analysis and Machine Intelligence, **20**(5), 493–504 (1998).

[78] R. Myers, R.C. Wison, and E.R. Hancock, "Bayesian graph edit distance," IEEE Transactions on Pattern Analysis and Machine Intelligence, **22**(6), 628–635 (2000).

[79] A. Robles-Kelly and E.R. Hancock, "Graph edit distance from spectral seriation," IEEE Transactions on Pattern Analysis and Machine Intelligence, **27**(3), 365–378 (2005).

[80] K. Siddiqi, A. Shokoufandeh, S.J. Dickinson, and S.W. Zucker, "Shock graphs and shape matching," International Journal of Computer Vision, **35**(1), 13–32, (1999).

[81] H. Qiu and E.R. Hancock, "Graph simplification and matching using commute times," Pattern Recognition, **40**(10), 2874–2889 (2007).

[82] C. Schellewald and C. Schnrr, "Probabilistic subgraph matching based on convex relaxation," In Energy minimization methods in computer vision and pattern recognition, Springer Berlin Heidelberg, 171–186 (2005).

[83] P.H.S. Torr, "Solving markov random fields using semi definite programming," In Artificial Intelligence and Statistics, (2003).

[84] A. Rangarajan, J. Coughlan, and A.L. Yuille, "A bayesian network framework for relational shape matching," In Computer Vision, 2003. Proceedings. Ninth IEEE International Conference on, 671–678 (2003).

[85] D. Cremers, T. Kohlberger, and C. Schnor, "Evaluation of Convex Optimization Techniques for the Weighted Graph-Matching Problem in Computer Vision," Proc. 23rd DAGM-Symp. Pattern Recognition, **2191** (2001).

[86] H. Chui and A. Rangarajan, "A new point matching algorithm for non-rigid registration," Computer Vision and Image Understanding, **89**(2), 114–141 (2003).

[87] A. Rangarajan, H. Chui, and F.L Bookstein, "The softassign procrustes matching algorithm," In Information Processing in Medical Imaging, Springer Berlin Heidelberg, 29–42 (1997).

[88] A.L. Yuille, "Generalized deformable models, statistical physics, and matching problems," Neural Computation, **2**(1), 1–24 (1990).

[89] R. Sinkhorn, "A relationship between arbitrary positive matrices and doubly stochastic matrices," The annals of mathematical statistics, 876–879 (1964).

[90] T.T.V. Cao, "Nonhomogeneity Detection in CFAR Reference Windows Using the Mean-to-Mean Ratio Test (No. DSTO-TR-2608). Defence Science and Technology Organization, Edinburgh (Australia) (2012).

[91] P. Patidar, M. Gupta, S. Srivastava, and A.K. Nagawat, "Image de-noising by various filters for different noise," International Journal of Computer Applications, 0975–8887 (2010).

[92] E. Arias-Castro and D.L. Donoho, "Does median filtering truly preserve edges better than linear filtering?," The Annals of Statistics, 1172–1206 (2009).

[93] S. Almasi, X. Xu, A. Ben-Zvi, B. Lacoste, C. Gu, and E.L. Miller, "A novel method for identifying a graph-based representation of 3-D microvascular networks from fluorescence microscopy image stacks," Medical image analysis, **20**(1), 208–223 (2015).

[94] A. Bindilatti and N. Mascarenhas, "A Nonlocal Poisson Denoising Algorithm Based on Stochastic Distances," IEEE Signal Processing Letters **20**(11), 1010–1013 (2013).

[95] P. Coupé, M. Munz, J.V. Manjon, E. Ruthazer, and D.L. Collins, "A CANDLE for a deeper in-vivo insight," J. Medical Image Analysis, **16**(4), 849–864 (2012).

[96] K.N. Chaudhury and M. Singer, "Non-Local Euclidean Medians," IEEE Signal Processing Letters **19**(11), 745–748 (2012).

[97] S. Aja-Fernández, G. vegas-Sanchez-Ferrero, M. Martn-Fernández, and C. Alberola-López, "Automatic Noise Estimation in Images Using Local Statistics. Additive and Multiplicative Cases," J. Image and Vision Computing **27**(6), 756–770 (2009).

[98] S. Almasi, E.L. Miller, "Microvasculature network identification in 3-D fluorescent microscopy images," In: IEEE International Symposium on Biomedical Imaging (ISBI), San Fransisco, 444–447 (2013).

[99] A.F. Frangi, W.J. Niessen, K.L. Vincken, M.A. Viergever, "Multiscale vessel enhancement filtering," Med. Image Comput. Comput.-Assisted Interventation (MICCAI), 130–137 (1998).

[100] W.T. Freeman, E.H. Adelson, "The design and use of steerable filters," IEEE Transaction Pattern Analysis and Machine Intelligence, **13**, 891–906 (1991).

[101] G.L. Nemhauser and L.A Wolsey, "Integer and Combinatorial Optimization," **18**, Wiley, New York (1988).

[102] D. Sage, ¡http://bigwww.epfl.ch/sage/soft/localnormalization/¿ (2014).

[103] D. Mayerich, C. Bjornsson, J. Taylor, and B. Roysam, "NetMets: software for quantifying and visualizing errors in biological network segmentation," J. BMC Bioinform, **13**, 1–19 (2012).

[104] J. Collins, C. Kurcz, C. Lisle, Y. Liu, E. Zudaire, "Assessment of vascular network segmentation," Int. J. Image Process. **4**, 584–599 (2011).

[105] G. Fudenberg, L. Paninski, "Bayesian image recovery for dendritic structures under low signal-to-noise conditions," IEEE Transaction Image Process. **18**, 471–482 (2009).

[106] J.E. Bresenham, "Algorithm for computer control of a digital plotter," J. IBM Systems, **4**(1), 25–30 (1965).

[107] J.P. Salmon, I. Debled-Rennesson, and L. Wendling, "A new method to detect arcs and segments from curvature profiles," In ICPR (3), 387–390 (2006).

[108] C. Goodall, "Procrustes methods in the statistical analysis of shape," Journal of the Royal Statistical Society. Series B (Methodological), 285–339 (1991).

[109] S. Gold, A. Rangarajan, C.P. Lu, S. Pappu, and E. Mjolsness, "New algorithms for 2d and 3d point matching: pose estimation and correspondence," Pattern Recognition, **31**(8), 1019–1031 (1998).

[110] R.A. Horn and C.R Johnson, "Matrix analysis," Cambridge university press (2012).

[111] C. Schellewald, S. Roth, and C. Schnrr, "Evaluation of a convex relaxation to a quadratic assignment matching approach for relational object views," Image and Vision Computing, **25**(8), 1301–1314 (2007).

[112] H. Wang and J.S. Marron, "Object oriented data analysis: Sets of trees," The Annals of Statistics, **35**(5), 1849–1873 (2007).

[113] B. Aydin, G. Pataki, H. Wang, E. Bullitt, and J.S. Marron, "A principal component analysis for trees," The Annals of Applied Statistics, 1597–1615 (2009).